7-1-2022

A Novel Power-Efficient Wireless Multi-channel Recording System for the Telemonitoring of Electroencephalography (EEG)

Mahmoud Sharafi
mshar052@fiu.edu

FLORIDA INTERNATIONAL UNIVERSITY

Miami, Florida

A NOVEL POWER-EFFICIENT WIRELESS MULTI-CHANNEL RECORDING SYSTEM FOR THE TELEMONITORING OF ELECTROENCEPHALOGRAPHY (EEG)

A dissertation submitted in partial fulfillment of

the requirements for the degree of

DOCTOR OF PHILOSOPHY

in

ELECTRICAL AND COMPUTER ENGINEERING

by

Mahmoud Sharafi Masouleh

2022

To: Dean John L.Volakis
College of Engineering and Computer

This dissertation, written by Mahmoud Sharafi Masouleh, and entitled A Novel Power-Efficient Wireless Multi-Channel Recording System for the Telemonitoring of Electroencephalography (EEG), has been approved concerning style and intellectual content and is referred to you for judgment.

We have read this dissertation and recommend that it be approved.

Ilker Yaylali

_____

Mercedes Cabrerizo

_____

Berrin Tansel

_____

Nezih Pala

_____

Malek Adjouadi, Major Professor

Date of Defense: July 1, 2022

The dissertation of Mahmoud Sharafi Masouleh is approved.

_____

Dean John L. Volakis
College of Engineering and Computer

_____

Andrés G. Gil
Vice President for Research and Economic Development
and Dean of the University Graduate School

Florida International University, 2022

DEDICATION

This dissertation is entirely dedicated to my wife Maryam Sajedi and my parents Zahra Reihanian and Dr. Akbar Sharafi. The achievement of this lifelong goal would not have been possible without the unending support, love, and motivation from these beloved ones.

ACKNOWLEDGMENTS

It would not have been possible to complete this dissertation and research without the support and dedication of Prof. Malek Adjouadi. I am deeply grateful to him for his guidance, enthusiastic encouragement, advice, and financial support throughout my Ph.D. program. I enjoyed working with Prof. Adjouadi for the duration of my doctoral work and had growing opportunities within and outside of the university as my research progressed. I would also like to thank the rest of my thesis committee: Dr. Mercedes Cabrerizo, Dr. Nezih pala, Dr. Berrin Tansel, and Dr. Ilker Yaylali for their insightful comments and encouragement.

Pursuing a Ph.D. was not without difficulties, but perseverance ultimately contributed to achieving a highly distinguished lifelong accomplishment. This would not have been possible without the help and support of others who believed in me from the beginning. To begin, I would like to acknowledge the technical support I received from my colleagues at the Center for Advanced Technology and Education, which led to a unique and innovative research collaboration during my graduate studies. The next thing I would like to acknowledge is my sincere gratitude to my friends' caring support, whose presence, regardless of their distance, brought a sense of warmth and light to my heart during those difficult times. Finally, I would like to express my most profound appreciation for the kind, unwavering support I received from my wife, parents, and my dear friend Amin Kargar throughout this journey.

This research is supported by the National Science Foundation under grants: CNS-1920182, CNS-1551221, CNS-1338922, CNS- 2018611, and by the National

Institutes of Health through the 1P30AG066506-01 with the 1Florida Alzheimers Disease Research Center (ADRC). Our thanks also go to the Ware Foundation.

ABSTRACT OF THE DISSERTATION

A NOVEL POWER-EFFICIENT WIRELESS MULTI-CHANNEL RECORDING SYSTEM FOR THE TELEMONITORING OF ELECTROENCEPHALOGRAPHY

by

Mahmoud Sharafi Masouleh

Florida International University, 2022

Miami, Florida

Professor Malek Adjouadi, Major Professor

This research introduces the development of a novel EEG recording system that is modular, batteryless, and wireless (untethered) with the supporting theoretical foundation in wireless communications and related design elements and circuitry. Its modular construct overcomes the EEG scaling problem and makes it easier for reconfiguring the hardware design in terms of the number and placement of electrodes and type of standard EEG system contemplated for use. In this development, portability, light weight, and applicability to other clinical applications that rely on EEG data are sought. Due to printer tolerance, the 3D printed cap consists of 61 electrode placements. This recording capacity can however extend from 21 (as in the international 10-20 systems) up to 61 EEG channels at sample rates ranging from 250 to 1000 Hz and the transfer of the raw EEG signal using a standard allocated frequency as a data carrier. The main objectives of this dissertation are to (1) eliminate the need for heavy mounted batteries, (2) overcome the requirement for bulky power systems, and (3) avoid the use of data cables to untether the EEG system from the subject for a more practical and less restrictive setting.

Unpredictability and temporal variations of the EEG input make developing a battery-free and cable-free EEG reading device challenging. Professional high-quality and high-resolution analog front ends are required to capture non-stationary EEG signals at microvolt levels. The primary components of the proposed setup are the wireless power transmission unit, which consists of a power amplifier, highly efficient resonant-inductive link, rectification, regulation, and power management units, as well as the analog front end, which consists of an analog to digital converter, pre-amplification unit, filtering unit, host microprocessor, and the wireless communication unit. These must all be compatible with the rest of the system and must use the least amount of power possible while minimizing the presence of noise and the attenuation of the recorded signal

A highly efficient resonant-inductive coupling link is developed to decrease power transmission dissipation. Magnetized materials were utilized to steer electromagnetic flux and decrease route and medium loss while transmitting the required energy with low dissipation. Signal pre-amplification is handled by the front-end active electrodes. Standard bio-amplifier design approaches are combined to accomplish this purpose, and a thorough investigation of the optimum ADC, microcontroller, and transceiver units has been carried out. We can minimize overall system weight and power consumption by employing battery-less and cable-free EEG readout system designs, consequently giving patients more comfort and freedom of movement. Similarly, the solutions are designed to match the performance of medical-grade equipment. The captured electrical impulses using the proposed setup can be stored for various uses, including classification, prediction, 3D source localization, and for monitoring and diagnosing different brain disorders.

TABLE OF CONTENTS

CHAPTER PAGE

Chapter I. Introduction and Research Background…….....1
1.1 Introduction…….1
1.2 Research Purpose……2
1.3 Research Problem……2
1.4 Significance of Study……3
1.5 Theoretical Perspective and Literature Review……..4

Chapter II EEG Cap Head-surface-based positioning solutions based on 10/20 and 10/10 systems……..5
2.1 Electroencephalogram Signal Measurement……..5
2.2 Placement of the Electrode to Capture EEG Signals……6
2.2.1 10/20, 10/10, and 10/5 System……7
2.3 EEG Cap and Electrode Holders……9
2.4. EEG Cap 3-D Printing……15

Chapter III: Highly Efficient Power Generation, Transmission Conversion Chain……..19
3.1 Introduction……19
3.2 Wireless Power Transmission for Wearable EEG Readout System……..22
3.2.1 Power Generation, Transmission & Conversion Chain 25
3.2.2 The EEG Front-End Block 27
3.2.3 Data Transmission 28
3.3 Description and Details of Proposed System……...29
3.3.1 The Constraints of the Proposed Portable EEG Recording Setup.....30
3.4 Far-Field Vs. Mid-range Near Field Powering……...34
3.4.1 Design, Analysis, of the Array of Axial Rectangular Slots on a Cylindrical Waveguide 38
3.4.1.1 Far-field power harvesting 38
3.4.1.2 First and Second Design Equations 39
3.4.1.3 The Error Function 41
3.4.1.4 Slot Design Equation Error Function 42
3.4.1.5 A Relation for the Radiation Pattern of Axial Slot Array 43
3.4.1.6 Synthesis of Slot Array……...45

3.4.1.7 Fabrication, Measurement, and Comparison……...47

Chapter IV Near-Field Wireless Power Transmission 52
4.1 Inductive or Resonant Inductive……..52
4.2 Wireless Powering Standards and Protocols……53
4.2.1 An efficient Wireless Power Transfer Link's Requirements 53
4.2.2 Technical Concerns Regarding the Power Delivered to Load in the Design Procedure 55
4.2.3 Single or Multi-Loop Resonator……56
4.2.4 Resonator Specification.....58
4.2.5 4-loop resonator power transmission link 58
4.2.6 Resonator Configurations.....59
4.2.6.1 The Octagonal Spiral Inductor's configuration coefficient and analytical calculations.....60
4.2.6.2 Finalized Design of Resonator 62
4.3 The Optimum Conformal Wireless Power Transmission line……..62
4.3.1 Calculation Methods Proposed Conformal Wireless Power Transmission Link 64
4.3.2 Link's PTE Enhancement Using Magnetized Strips 65
4.3.3 An Analysis of the Alignment and Misalignment 68
4.3.4.1 Lateral and Angular Misalignment.....68
4.4 Wirelessly Powered EEG Readout Systems via Intelligent Powering Setup……..71
4.4.1 Intelligent Positioning System Frame 72
4.4.2 Positioning System Algorithm 74
4.4.3 Design and Analysis of Testbed.....79
4.5 Electronics and drivers of proposed Wireless power transmission link…….81
4.6 Power Amplifier…….84
4.6.1 Coupling Coefficient Impact on Wireless Power Transmission ……86
4.6.2 Powering Front-end and Back-end Circuits and Electronics……...87
4.6.3 Powering Front-end Units 89
4.6.4 Powering Algorithms……91
4.6.5 Front-end Power Management Description.....92
4.6.6 Technical Specifications of Power Conversion Chain 95

Chapter V Fabrication, Testing, and Experimental Results 98
5.1. Conformal Resonator's Geometries and Parameters 98
5.2 Frequency Shift Compensation-Capacitive Effect…….101
5.3 Coupling Distance Effect on Link's Power Transfer Efficiency……104

5.4 Planar 20-way Octagonal Power Combiner……..106
5.5 Power Transmitter Resonator Array (Back-end Tx Testbed).....109
3.11.6 Power Receiver Resonator Array (Front-end Rx Testbed) 110

Chapter VI: EEG Read Out System's Front-End Electronics/Electrode and bio amplifier ……..112
6.1 Introduction and Prior Works……...112
6.1.1 EEG Capturing and Monitoring Systems…….113
6.1.2 Metrics in EEG recording amplification Unit……114
6.2 Instrumentation Amplifier Circuit……118
6.3. Single-channel versus multi-channel EEG recording system……..119
6.4. Active Electrode…….120
6.4.1 Active Electrode Architectures.....123
6.4.2. Noise Cancellation Challenges for AE Circuit Design 123
6.5. Technical Metrics for Active Electrode Design……124
6.5.1 Electrode Offset.....124
6.5.2 Common Mode Rejection Ratio.....124
6.5.3 Input Impedance.....124
6.5.4 Power Dissipation.....125
6.5.5 Number of Wires.....125
6.6 Design of an Active Electrode Preamplifier for Single-Channel EEG readout system …….....126
6.6.1 Electronic Circuit Design Analysis Type.....126
6.6.1.1 Transistor Sizes 126
6.6.1.2 Transient Analysis.....127
6.6.1.3 Common-Mode Input Range.....127
6.6.1.4 Maximum Input and Output Swing.....127
6.6.1.5 Input Impedance.....127
6.6.1.6 CMRR 127
6.6.1.7 Power Consumption 128
6.7 Design Process and System Components……..128
6.7.1 Parametric Analysis and Optimization of MOSFET and Simulation Results…...130

Chapter VII: Filter, Analog-to-Digital Converter (ADC)& Microcontroller 134

7.1 Filters……134
7.1.1 The Most Common Way to Choose a Filter for Electroencephalography 134
7.1.2 Type of Filters 135
7.2 Analog-to-Digital Converter (ADC)……...137
7.2.1 Successive Approximation Register Analogue-to-Digital Converter…….137
7.2.2 SAR ADC's Efficiency in terms of energy 138
7.2.3 SAR ADC Coding Complexity 138
7.2.4 SAR ADC Resolution and sampling rate 139
7.3 Microcontroller Unit……..139
7.3.1 Different types of Microcontroller 140
7.3.2 MCU Comparison 141
7.4 Transmitter……143
7.4.1 Bidirectional Communication link for power management unit……...143
7.5 Modular Design……146
7.5.1 Topology of the Framework……...149
7.5.2 Schematic modular design and PCB Layout……149

Chapter VIII: Conclusion..... 152
8.1 Design Contributions……154
8.2 Retrospective……..157

List of References 159

VITA…… 186

LIST OF TABLES

TABLE PAGE

Table 3.1. Characteristics of structure optimized parameters and desired pattern antenna,.....53

Table 3.2. Optimized parameters of antenna 55
Table 3.3. The design parameters of the link.....83
Table 5.1. Measured Capacitor impact on wireless power transmission Efficiency 102

Table 5.2. Simulation and Measured Data of Coupling Distance……104

Table 6.1. CFIA components operating points, sizes, and values (refer to 1 in figure 8.4).....125

Table 6.2. The voltage amplifier components' operating points, sizes, and values (refer to 2 in figure 8.4) 125

Table 6.3. Operating points, sizes, and values for the OTA components (refer to 3 in figure 6.8)…….....126

Table 6.4. Gm-C filter trans conductor component operating points and sizes (see 4 in figure 8.4). 126

Table 7.1. MCUs types & properties 135

LIST OF FIGURE

FIGURE PAGE

Figure 2.1. Electrode implantation location for designing portable EEG cap …….24

Figure 2.2. 3D view of designed EEG cap based on technical requirements 27

Figure 2.3 3D Printed EEG Cap 29

Figure 3.1 The Schematic Block Diagram 35

FIGURE 3.2 SCHEMATIC OF BACK-END POWERING UNITS ……..36

Figure 3.3. the front-end power transmission-conversion chain units 37

Figure 3.4. Schematic diagram of Front-End of EEG recording system 37

Figure 3.5. Two scenarios for downlinking a and uplink communication i EEG recording system 38

Figure 3.6. scale model of suggested wireless and battery-free EEG recording cap system 39

Figure 3.7. The suggested wirelessly powered Tx multi-resonator setup 39

Figure .3.8. An array of narrow rectangular slots along the axis of the cylindrical waveguide 48

Figure. 3.9. The equivalent circuit of axial slot array 49

Figure 3.10. Two-column narrow rectangular slot array on a cylindrical waveguide 52

Figure 3.11. E-plane pattern cut comparison between MLS and HFSS at 9GHz in XZ-plane for $\varphi = 0$ 53

Figure 3.12. Simulated results of VSWR 54

Figure 3.13. Fabrication of the 22-slot antenna (two rows of 11 elements).. 56

Figure 3.14. Measured and simulated return loss (S_{11}) versus frequency 56

Figure 3.15. Measured and simulated radiation patterns for an axial slot at operating frequency f = 9 GHz 56

Figure 4.1. Coupling distance d12 and mutual inductance M_{23} 61

Figure 4.2. the layout of a square spiral inductor 65

Figure 4.3. the layout of an octagonal spiral inductor 65

Figure 4.4. Circuit model of powering link by reflected load theory 66

Figure 4.5. Octagonal spiral inductor designed for being installed on EEG cap 68

Figure 4.6. Proposed testbed for recording EEG signals 68

Figure 4.7. Circuit model of suggested octagonal shape Tx-Rx resonators 69

Figure 4.8. CAD model of magnetized loop placed on PCB substrate backside between the L1 and L2 71

Figure 4.9. PTE drop when the coupling distance increases between 8 to15mm 72

Figure 4.10. frequency drop compensation by adding magnetize strips in 10cm coupling distant 72

Figure 4.11. a. perfect alignment, b.angular misalignment, c. lateral misalignment, and d. both angular and lateral misalignment 1.....74

Figure 4.12. Simulated angular Misalignment Versus Link's power transfer Efficiency 74

Figure 4.13. Two and multi-resonator configuration angular misalignment versus power transfer efficiency 75

Figure 4.14. a lattice design framework for Tx array 77

Figure 4.15. Intelligent positioning and feeding system 77

Figure 4.16. the designated permanent magnet positioned in the center of the Rx resonator 79

Figure 4.17. The Feedback System for Remotely Powered Untethered EEG Cap 80

Figure 4.18. the Power transmission efficiency of the resonant-inductive Power transmission Lateral misalignment 81

Figure 4.19. The Effect of the outermost diameter of resonators on power transfer efficiency 83

Figure 4.20. (a) an array of Tx power transmitter resonators (b) a variety of RxP ower receiver resonators 84

Figure 4.21. the recommended powering setup for a wireless and battery-free EEG reading device set 85

Figure 4.22. Simulation result of power transfer efficiency of powering back-end and WPT link 86

Figure 4.23. Circuit model of Tx-Rx powering link 87

Figure 4.24. resonant inductive link and E-class external link driver 88

Figure 4.25. the Simulated Power Efficiency vs. Coupling coefficient results for a Class-E power amplifier optimized with k =0.01 89

Figure 4.26. Tx resonator driver electronics 92

Figure 4.27. Driver Efficiency Vs. load 1.....92

Figure 5.1. The Layout, Excitation Port, and Resonance Capacitor Bank of the Proposed Octagonal Spiral Resonator……..98

Figure 5.2. CAD model and experimental setup for measuring the power transfer efficiency in a 4-loops resonance- inductive link operating at 6.78 MHz……99

Figure 5.3. Comparison of the proposed powering link's measured and simulated power transfer efficiency in 60 mm coupling distance……...100

Figure 5.4. Capacitive effect of the power transmission link (HFSS simulation results)…….……101

Figure 5.5. The Figure of Merit comparison for simulation results and measured data 102

Figure 5.6. A testbed to evaluate the coupling distance effect on power transfer efficiency……...……103

Figure 5.7. link's power transfer efficiency versus Tx-Rx coupling distance……..103

Figure 5.8. Coupling distance variation vs. Simulation PTE results and measured PTE data…….…….....105

Figure 5.9 a) CAD View and b) The fabricated circular power combiner 20*1……..……106

Figure 5.10. Simulated and measured return loss of the output port…….....108

Figure 5.11 CAD model and experimental setup for powering resonator array…….....108

Figure 5.12 CAD model and Fabricated setup (Front-end Rx array mounted on EEG head cap)…….……109

Figure 6.1. Block diagram of EEG measurement and recording subsystems 113

Figure 6.2. Electrode Tissue Interface circuit model 115

Figure 6.3. Conventional EEG readout system block diagram 117

Figure 6.4. The three Op-Amp IA configurations (Image courtesy of Texas Instruments) 119

Figure 6.5. A typical Drivel -Right Leg for EEG readout system [292] 119

Figure 6.6. (A) a single-channel conventional EEG system and (B) a multi-channel EEG system 117

Figure 6.7. Active Electrode AE based EEG readout system 118

Figure 6.8. Optimized proposed pre- amplification unit CMOS designed based on CFIA 125

Figure 6.9. Signal Amplification…….128

Figure 7.1. block design successive approximation registers……..132

Figure 7.2. Schematic design of suggested EEG recording front end system……144

FIGURE 7.3. PCB OF SUGGESTED EEG RECORDING SYSTEM'S FRONT END 152

LIST OF ACRONYMS & ABBREVIATIONS

A	
ABCI	Ambulatory Brain-Computer Interface
ADC	Analog to Digital Converter
AFE	Analog-Front-End
ANC	Adaptive Noise Cancelling
ASIC	Application-Specific Integrated Circuit
ADC	Analog-to-Digital Converter
AE	Active Electrode
AZ	Autozeroing
B	
BCI	Brain Computer Interface
BW	Bandwidth
BCI	Brain-Computer Interface
BIT	Bipolar Junction Transistor
C	
C_{bs}	Bulk to Source Capacitance
C_d	Depletion Capacitance
CG	Gate to Bulk Capacitance
CGA	Common Gate Amplifiers
C_{gs}	Gate to Source Capacitance
CLK	Clock
CMFB	Common Mode Feedback
CMFF	Common Mode Feedforward
CMRR	Common Mode Rejection Ratio
CM	Common Mode
CNS	Central Nervous System
CS	Source to Bulk Capacitance
CSA	Current Source Amplifiers
CT	Continuous-Time
CFI	Current Feedback Instrumentation Amplifier
CHS	Chopper Stabilization
CMFB	Common-Mode Feedback
CMFF	Common-Mode Feedforward
CMRR	Common-Mode Rejection Ratio
CNS	Central Nervous System
CT	Computed Tomography

D	
DAC	Digital to Analog Converter
DNL	Differential Non-Linearity
DR	Dynamic Ratio
DT	Discrete Time
DAE	Digital Active Electrode
DRC	Design Rule Check
DRL	Driven-Right-Leg
DSL	DC Servo Loop
E	
EEG	Electroencephalogram
EMG	Electromyogram
ENOB	Effective Number of Bits
ERD	Event-Retarded Synchronization
ECG	Electrocardiography
EDA	Electronic Design Automation
EEG	Electroencephalography
EMC	Electromyography
ETI	Electrode-Tissue Impedance
F	
FC	Folded Cascaded
FIFO	First In First Out
FoM	Figure of Merit
FIR	Finite Impulse Response
FOD	Foreign Object Detection
FPGA	Field-Programmable Gate Array
FT	Frequency response
G	
GBW	Gain Band-Width
g_m	transconductance
g_{mb}	bulk transconductance
H	
H_e	Noise Transfer function
H_x	Signal Transfer function
HDL	Hardware Description Language
I	
ICMR	Input Common Mode Range
I_D	Drain current

I_{DO}	Characteristic current
IFSECN	International Federation Committee Society of Electroencephalography
INL	Integral Non-Linearity
ISI	Inter-symbol Interference
IA	Instrumentation Amplifier
ICA	Independent Component Analysis
IEEE	Institute of Electrical and Electronics Engineers
IEC	International Electrotechnical Commission
IRN	Input-Referred Noise
K	
K	Coupling coefficient
L	
L	Length of a CMOS transistor
LVS	Layout versus Schematic
M	
MC	Monte Carlo
MEG	Magnetoencephalography
MSB	Most Significant Bit
MRI	Magnetic Resonance Imaging
MOSFET	Metal Oxide Semiconductor Field-Effect Transistor
MRI	Magnetic Resonance Imaging
N	
NI	National Instruments
NMR	Nuclear Magnetic Resonance
NRZ	Non-Return to Zero
NEF	Noise Efficiency Factor
NMOS	N-channel MOSFET
O	
OL	Overload Level
OSR	Oversampling Rate
OTA	Operational Transconductance Amplifier
Op-Amp	Operational Amplifier
OTA	Operational Transconductance Amplifier
P	
PM	Phase Margin
PSD	Power Spectral Density
PDK	Process Design Kit
PDL	Power Delivered to Load
PET	Positron Emission Tomography

PMOS	P-channel MOSFET
PGTCC	Power Generation ,Transmission and Conversion Chain
PTE	Power Transfer Efficiency
PWM	Pulse-Width-Modulation
Q	
q	Magnitude of the electrical charge on the electron
R	
R	Resistance
Rbi	Effective series bulk resistance
Rgi	Effective series gate-metal resistance
R-C	Resistor-Capacitor
RCCM	Regulated Cascade Current Mirror
RMS	Root Mean Square
RRL	Ripple Reduction Loop
S	
S	Geometrical shape factor
SAR	Successive Approximation Register
SC	Switched Capacitor
SCP	Slow Cortical Potentials
SNR	Signal-to-Noise Ratio
SINAD	Signal, Noise and Distortion
SNDR	Signal to Noise-plus-Distortion Ratio
SNR	Signal to Noise Ratio
SW	Switch
U	
ULV	Ultra-Low Voltage
UT	Thermal voltage
V	
VBS	Bulk to Source Voltage
VDS	Drain to Source Voltage
VEP	Visual Evoked Potentials
V_G	Gate to Bulk Voltage
V_{GS}	Gate to Source Voltage
VS	Source to Bulk Voltage
VT	Threshold voltage
VTO	Threshold voltage for zero substrate bias
W	
W	Width of a CMOS transistor

Chapter I Introduction and Research Background

1.1 Introduction

Electrical activity of the human brain as recorded through electroencephalography (EEG) recording has been a research area of significant interest for many scientists and researchers for several decades since the inception of electrode recordings in 1890. Richard Caton was the first to have reported his findings on brain electrical signals [1] and introduced the existence of such electrical brain rhythms to the world. In the 1920s, Hans Berger discovered the presence of certain rhythms in brain signals and was the first to use a recording method we now know as Electroencephalograms [2]. Since then, Electroencephalography (EEG) signals as a recording modality for research and diagnosis have become ubiquitous in medical schools and hospitals [3]. EEG recordings have subsequently been utilized to detect central nervous system abnormalities such as encephalopathies, epilepsy, and structural lesions [4] and examine other dysfunctions associated with various neurological and neurodegenerative illnesses.

Electroencephalography has many advantages, such as high temporal resolution and the ability for mobile and long-term measurements compared to positron emission tomography (PET), magnetic resonance imaging (MRI), and computerized tomography (CT) [5]. Besides the mentioned advantages, the recorded EEG signals can be used for brain-computer interface (BCI) to control all kinds of devices to better everyday life, including entertainment such as video games and medical implantation procedures like the prostheses described in [6–8].

1.2 Research Purpose

Despite the many advantages of EEG systems, the low spatial resolution compared to other neuroimaging techniques is the downside of such a recording technique. High-density EEG systems with 126-256 channels have emerged to address this problem, but they still include excessive setup time, cumbersome wirings, or battery-powered related issues. Typical EEG recording systems are pretty bulky where the channels are connected with cables to a local processing system, which prevents monitoring during ambulation. So the use of typical EEG recording systems usually requires a relatively lengthy amount of time to set up (around 45-60 minutes) [9]. On the other hand, single-channel EEG systems offer quick setup time, increased user comfort, and, most importantly, the ability for a specific measurement during ambulation, such as monitoring sleep, gauging auditory evoked potential, or even assessing the type of induced emotion through specific stimulation. However, such setups suffer from low spatial resolution and are limited in scope for the more meaningful representations of brain activity and 3-D source localization that can be attained with multi-channel EEG recordings.

1.3 Research Problem

The proposed design elements for a wireless and batteryless recording system are developed to to create a power-efficient, wireless multi-channel cable and battery-free recording system for telemonitoring electroencephalography (EEG) data. Although the practical focus is on EEG recording, such a system is shown to be adaptable for recording other signals emaniating from sensors or any other recording device. This type of design as contemplated leads to a more comfortable and less obtrusive and restrictive headset that

could solve pertinent design issues while making the system more practical and appealing to both patients and clinicians. However, the high impedance at the electrode-tissue interface seen with dry electrodes increases noise and interference from the environment. Interesting studies have shown different ways of overcoming some of these practical issues [10-14]. It should be mentioned that one of the main drawbacks of dry electrodes is motion artifacts seen in the recorded signals. To address the motion artifacts issue, active electrodes circuit (AEs) have been developed and simulated. These are likely candidates for providing reliable EEG to be used for further processing. This will also remove extensive wiring for transmitting data and heavy batteries as power supply.

1.4 Significance of Study

The significance of this research endeavor is in consolidating our understanding of the engineering and computing principles behind designing a portable hardware setup with the ability to wirelessly power an EEG recording system in an untethered and freely moving target. The intellectual merit of the study is in the integrated software-hardware design to serve as a wearable EEG system for long-term monitoring and diagnosis of brain activity as reflected through EEG. This research endeavor builds the system and related circuit design elements to create a novel wireless multi-channel EEG signal recording setup to meet these essential design requirements. This system thus contends with the complex portability issues and mitigates the ubiquitous presence of noise in recording reliable and repeatable EEG signals that are transmitted wirelessly.

1.5 Theoretical Perspective and Literature Review

The initial steps of this research are devoted to improving current wireless EEG recording systems for multi-channel EEG signal acquisition, including the EEG cap and resonator holders. Then we focus on designing a power-efficient battery-free wireless multi-channel recording system for wireleslly recording and transmitting EEG signals or any other signal captured through some other sensor or recording device. This matter entails a thorough review and analysis of current technologies related to highly efficient wireless powering and highly reliable wireless communication besides active electrode module design and the other required front-end electronics. The primary focus of this dissertation will be on the wireless power transmission, removing the powering cables, and designing a battery-free EEG recording signal setup.

To achieve a highly efficient EEG recording front end electronics, the primary design considerations will be power consumption, power efficiency, input impedance, noise, electrode offset, common-mode rejection ratio (CMRR), higher-order modulation technique, antenna design, and proper analog to a digital method for the EEG recording application. This will, in turn, guarantee reliable interpretation of the EEG, which can be used for monitoring the condition of the brain or as means for human-computer interaction or for the control input to an actuation mechanism (e.g., the communication system for people with locked-in syndrome or control system for prostheses or wheelchairs) . By providing high-quality signals in single or multi-channel EEG recordings, this technology could offer a viable alternative to the unfavorable standard EEG systems in diagnosing various disorders. Moreover, a dependable system could contribute to the advancement of telemedicine by eliminating the need for local professional assistance or a visit to a clinic.

As considered in this dissertation, the improvement of such systems could also benefit other electrophysiological measurement platforms such as EMGs or ECGs by providing good quality in signal acquisition.

The literature review mainly focuses on the different kinds of existing EEG recording system architectures and circuit design techniques. The circuit design techniques explored will range from conventional wire-based EEG recording systems to state-of-the-art techniques used for recording EEG signals to transmit recorded signals wirelessly with higher-order modulation and sampling techniques. The performance criteria of such sub-systems will likewise be researched for additional knowledge related to the system performance quality. The literature review article on domain applications of EEG is rich and extensive, as indicated by the selection of references provided here on Alzheimer's disease and epilepsy as two important study topics, among many others.

Before the design and theoretical accomplishments are revealed in the chapters that follow, It is emphasized here that the designs that were fabricated and tested in this dissertation included the 3D head cap, the electrode holders, the TX (RX) transmitter and receiver resonators, the resonator holders, an array of Rx resonator holder, and power combiner. The rest of the control circuitry and supporting electronic designs were also designed and simulated via standard existing software.

Chapter II EEG Cap Head-surface-based positioning solutions based on 10/20 and 10/10 systems

2.1 Electroencephalogram Signal Measurement

EEG signals are projections of brain activity that have been attenuated by the leptomeninges, cerebrospinal fluid, dura matter, bone, galea, and scalp. Cartographic

discharges have 0.5–1.5 mV amplitudes, with spikes reaching several millivolts when measured by subdural electrodes. The amplitudes on the scalp, on the other hand, are typically in the range of 0.5–200 μV. Because EEG pulses provide data about individuals' neuronal activities and neurophysiological features, it is feasible to analyze many functioning of the human brain using modern signal analysis techniques. Besides, Digital Signal Processing (DSP) techniques and advanced Brain-Computer. Furthermore, Digital Signal Processing (DSP) techniques and enhanced Brain-Computer Interface (BCI) mechanisms allow us to control numerous technologies that assist people. To achieve the stated aim, it is necessary first to understand the EEG cap's head-surface-based positioning solutions based on 10/20 and 10/10.

2.2 Placement of the Electrode to Capture EEG Signals

The 10-20 system is a widely used method of detecting EEG signals. The international 10–20 system is a method for specifying and applying the position of scalp electrodes in an EEG recording test. This method was developed to ensure that the results of a subject's study (clinical or research) could be compiled, duplicated, and appropriately analyzed and compared using the scientific method. The method is based on the link between the positioning of an electrode and the underlying area of the brain, specifically the cerebral cortex. The International Federation Societies for Electroencephalography and Clinical Neurophysiology (IFSECN) has approved the 10-20 system [17]. The 10-20 system depends on the percentage ratio (in terms of percentage) between electrode placement and underneath the region of the cerebral cortex, where 10% and 20% relate to the realistic intervals between neighboring electrodes of the whole skull's front-back or right-left

distance. Each of these spots has a classification that comprises a letter and a number to determine the lobe and hemisphere placement. The letters F represent the frontal lobe, T for the temporal lobe, C for the central lobe, P for the parietal lobe, and O for the occipital lobe. The numbers indicate which side a given electrode is placed on, an even number indicates the right side of the head, and an odd number indicates the left. In the 10-20 system, earlobe reference electrodes with expressions A_1 and A_2 are employed. Modern methods, such as the "10-5" system, use up to 256 electrodes, even though the original 10-20 system only had 21 electrodes [18].

2.2.1 10/20, 10/10, and 10/5 System

For more than 50 years, the universal 10-20 method has been the defacto norm for electrode placement to record brain signals. The relative distances between cranial landmarks over the head surface characterize head surface positions in this approach. The 10-20 system, also known as the international 10-20 system, describes and applies the placement of scalp electrodes in an EEG reading and recording. This approach was created to ensure that a subject's study outcomes could be collected, replicated, adequately assessed, and compared using the scientific method. The process is based on an electrode's placement and the brain's underlying region, especially the cerebral cortex.

During sleep and waking cycles, the brain generates various objectively known and identifiable electrical patterns, which electrodes may detect on the skin. Multiple extrinsic variables, such as age, prescription medicines, bodily illnesses, and drug dependency, may influence these patterns. Various branches and modifications of the 10-20 system are often used without precise definitions. Comparing different futures is a problem, and there is no

straightforward standard approach yet. So we must cope with derivatives' diversity. The demand for expanding the 10-20 approach to more significant density electrode configurations grew with multi-channel EEG hardware solutions. As a result, the 10-10 system was suggested, expanding the previous 10-20 system with a greater channel density of 81. Its specific version has also been adopted as a benchmark by the American Clinical Neurophysiology Society (ACNS) and the International Federation of Clinical Neurophysiology after some disagreements about electrode location naming. On the other hand, high-end consumers want even greater density electrode configurations. Marketed accessible 128-channel EEG devices and 256 channel EEG systems are becoming commonplace.

Oostenveld and Praamstra [19] logically expanded the 10-10 system to the 10-5 system, allowing for over 300 electrode sites (320 explicitly stated). Meanwhile, the 10-20 system's principal application shifted from guiding the placement of EEG electrodes to giving direct positional guidance for emerging transcranial neuroimaging methods, near-infrared spectroscopy, and transcranial magnetic stimulation. The 10-20 approach ensures that probe settings are constant across the participant’s scalp. In addition, the 10-20 approach is utilized to mediate probabilistic registration in the same way traditional cranial landmarks are employed. As a result, the 10-20 approach is becoming more widely used as a conventional relative head-surface-based positioning strategy for transcranial magnetic stimulation (TMS) brain mapping techniques. Indeed, it is also true that the initial 10-20 system was not designed to be a flexible system capable of handling such unusual scenarios. The 10-20 based systems have mainly been recognized as approaches to spatial resolution for EEG research. More densely positioned electrodes have been proved helpful in

enhancing spatial resolution when the three-dimensional signal source estimate is used. However, its use as a head-surface-based positioning system has received considerable attention.

2.3 EEG Cap and Electrode Holders

The numbers "10" and "20" indicate that the actual distances between neighboring electrodes are 10% and 20% of the skull's entire front-back or right-left space. A measurement is made across the top of the head, from the nasion to the inion. Most other commonly used measures ('landmarking methods') begin at one ear and conclude at the other, usually over the top of the head. The tragus, auricle, and mastoid are three anatomical sites of the ear [20-27]. The letters allocated to each electrode implantation position to identify which lobe or part of the brain it is reading from are pre-frontal (Fp), frontal (F), temporal (T), parietal (P), occipital (O), and central (C). Because of their positioning and depending on the individual, the "C" electrodes can display EEG activity more characteristic of frontal, temporal, and some parietal-occipital action and are always used in polysomnography sleep studies to determine sleep phases. There are (Z) spots as well; the Z (zero) electrode is positioned on the midline sagittal plane of the skull (Fp_z, F_z, C_z, O_z) and is used primarily for reference and measuring purposes. Because they are positioned across the corpus callosum, these electrodes will not necessarily reflect or enhance lateral hemispheric cortex activity, and they will not sufficiently represent either hemisphere.

In polysomnography sleep studies and diagnostic/clinical EEG montages aimed to represent/diagnose epileptiform seizure activity or suspected clinical brain death, "Z"

electrodes are frequently used as "grounds" or "references." The number of EEG electrodes required and their meticulous, measured implantation grow with each clinical necessity and modality. Even-numbered electrodes are located on the right side of the head, whereas odd-numbered electrodes are located on the left.

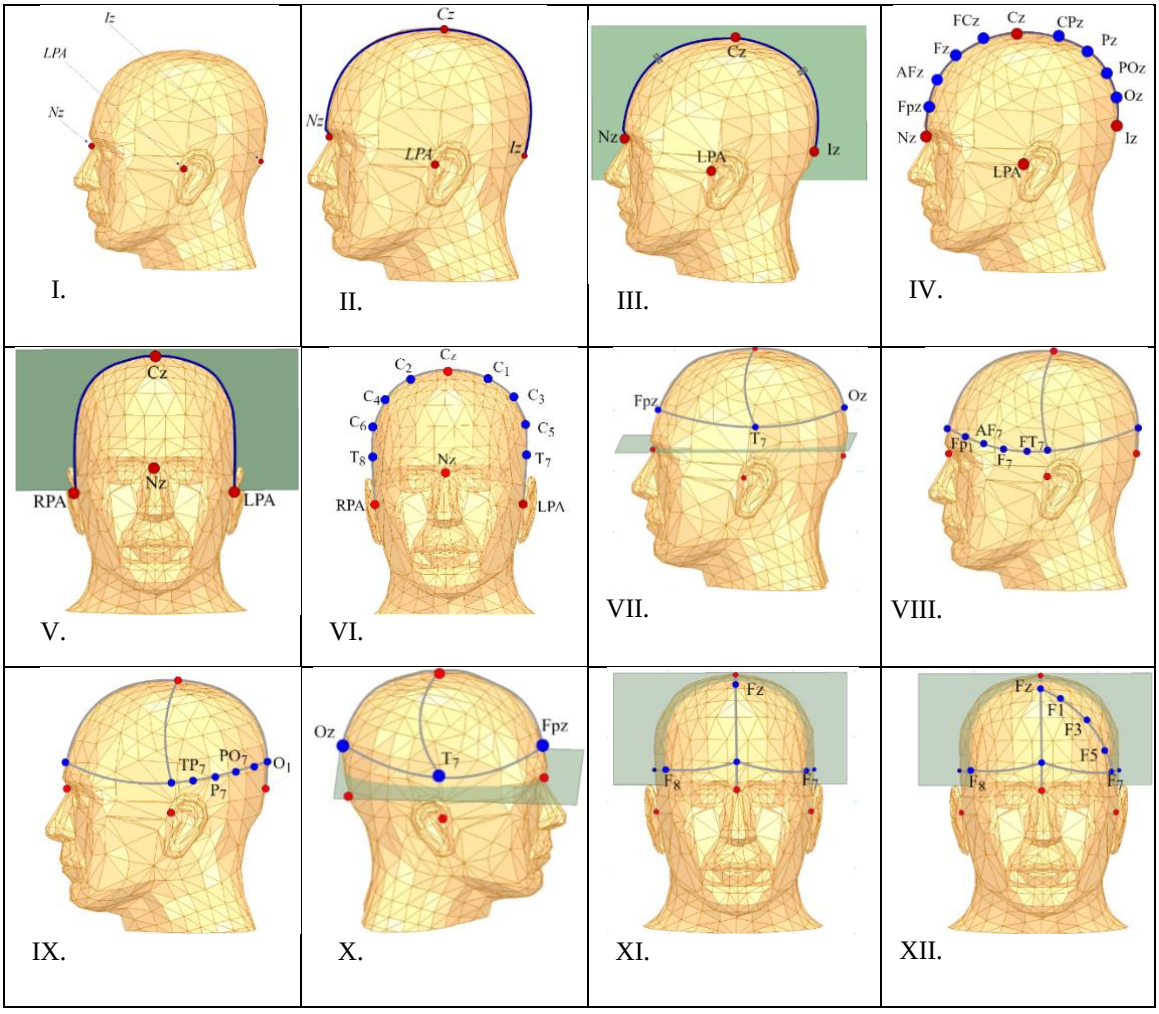

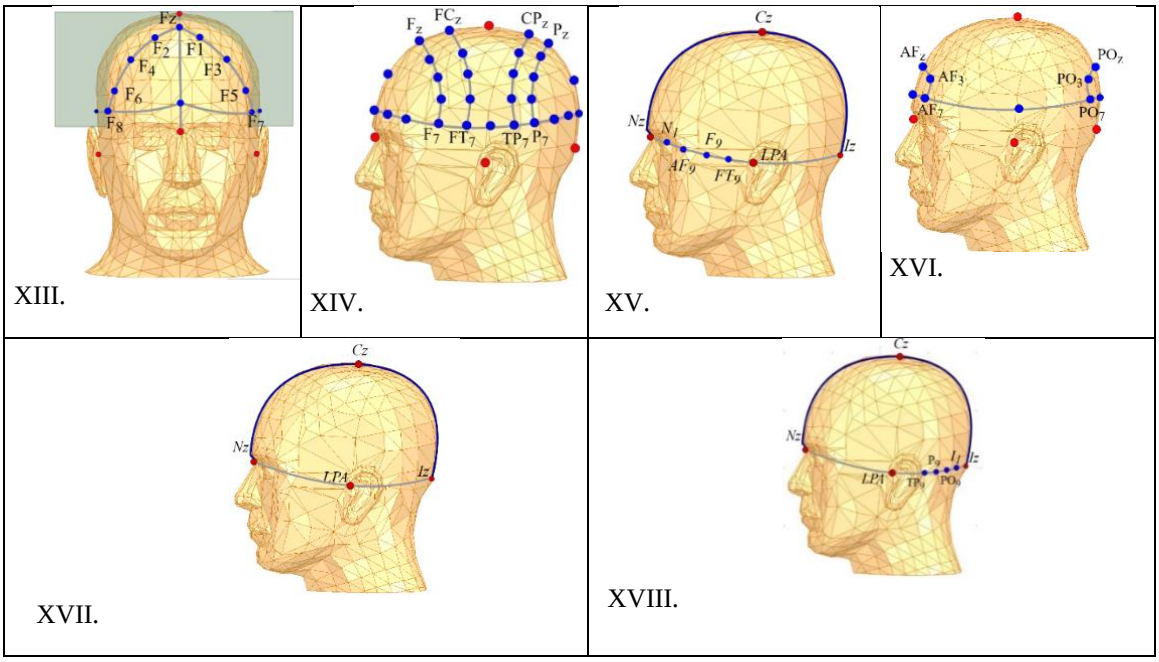

FIGURE 2.1. Electrode implantation location for designing portable EEG cap

To make a typical EEG cap, we need to understand the basics of the electrode locations. As a result, we begin by identifying four crucial reference points on the scalp anatomy. As seen in Figure 2.1.I, the nasion (N_z) is a dent at the upper root of the nose bridge; the inion (I_z) is an external occipital protuberance; the left preauricular point (LPA) is an anterior root of the center of the peak region of the tragus, and the right preauricular point (RPA) is determined in the same manner as the left. In the UI 10/10 system, LPA and RPA are the same as T_9 and T_{10}. The reference curves on a scalp must then be established. For clarity, as shown in Figure 2.1.II, a "reference curve" is defined as a path of crossover seen between the head surface and a plane given by three provided locations. We consider N_z and I_z to create the sagittal center reference curve around the head surface, with C_z acting as a temporary midpoint.As shown in Figure 2.1.III, the sagittal central reference curve is altered so that C_z splits both the sagittal and coronal main reference curves evenly spaced along with LPA, C_z, and RPA to create the coronal central reference curve across

LPA, C_z, and RPA. The UI 10-10 method divides the sagittal center reference curve in ten percent increments from N_z to I_z, yielding Fp_z, AF_z, Fz, FC_z, C_z, Cp_z, P_z, PO_z, and O_z.

Moreover, considering Figure 2.1.XV, the coronal center reference curve is separated into T_7, C_5, C_3, C_1, C_z, C_2, C_4, C_6, and T_8 by dividing it by 10% increments from LPA to RPA. As shown in Figure 2.5, The UI 10/10 method divides the sagittal center reference curve in ten percent increments from Nz to Iz, yielding Fp_z, AF_z, F_z, FC_z, C_z, Cp_z, Pz, PO_z, and Oz and considering Figures 2.2.V and 2.2.VI, the coronal center reference curve is separated into T_7, C5, C_3, C_1, C_z, C_2, C_4, C_6, and T_8 by dividing it by 10% increments from LPA to RPA).

Next, as shown in Figure 2.1.V and Figure 2.1.VI along Fpz, T_7, and O_z, a left 10% axial reference curve is created. To establish Fp_1, AF_7, F_7, and FT_7, we split the left anterior quarter of the turn by 1/5'th increment from Fpz to T_7. Then, across Fp_z, T_7, and Oz, a left 10% axial reference curve is created (Figure 2.1.VII).To establish Fp_1, AF_7, F_7, and FT_7, the left anterior quarter of the curve is split by 1/5'th increments from Fpz to T_7 (Figure 2.1.VIII). In Figure 2.1.IX , from T_7 to Oz, the space is divided by one-fifth increments to get TP_7, P_7, PO_7, and O_1 for the left posterior quarter. The same procedure is valid for the right side of the brain (Figure. 2.1.X). Following that, six coronal reference curves are created. To have a comprehensive view of what we expect to have as an EEG electrode holder based on 10-20 or 10-10 present, we start with four coronal reference curves in the center, using the frontal (F) coronal reference curve as an instance because anterior–frontal (AF) and posterior–occipital (PO) reference curves reflect different guidelines. F_7, F_z, and F_8 establish the F coronal reference curve (Fig. 2.2.XI). As shown in Figure 2.1.XII, F_5, F_3, and F_1 are generated by dividing the F_7–Fz segment of the curve by one-fourth intervals

from F_7 to Fz. We do the same for the F_8–Fz section (Figure 2.1.XIII). As shown in Figure 2.1.XIV, The front-central/temporal (FC/FT), temporal-/ Centro-parietal (TP/CP), and parietal (P) coronal reference curves are divided into quarters on each hemisphere.

As seen in Figure 2.1.XV, the anterior–frontal (AF) coronal reference curve, is then calculated utilizing AF_7, AF_z, and AF_8. Because quarterly subdivision causes overcrowding, the AF_7–AF_z section of the curve is now just intersected into half to produce AF_3, and the AF_z–AF_8 section is just split in half to create AF_4. Likewise, we establish PO_3 and PO_4 using the parietooccipital (PO) coronal reference curve and considering Figure 2.1.XVI, along with Nz, LPA (T_9), and Iz, we established a left zero percent axial reference curve. As shown in Figure 2.1 XVII, From LPA (T_9) to Nz, we divide by one-fifth increments to get FT_9, F_9, AF_9, and N_1 for the left anterior quarter. We split by one-fifth intervals from LPA (T_9) through I_z to get TP_9, P_9, PO_9, and I_1 for the left posterior quarter (Figure 2.1.XVIII). Similarly, N_2, AF_{10}, F_{10}, FT_{10}, TP_{10}, P_{10}, PO_{10}, and I_2 are set for the right hemisphere. A_1 and A_2 electrodes are put on the left and right ear lobes for EEG research. However, they are not required for other transcranial techniques. To retain intermodal generality, A_1 and A_2 are not being addressed in this thesis. Through the mentioned positioning system, 81 locations of the UI 10/10 methods can be specified. All the jobs defined in ACNS's 10-10 system are included in these 81 positions.

In the rest of the study, we employ this system to design a solid EEG cap for mounting electrodes, resonators, and electronics in this chapter. Except for the following modifications, the UI 10-10 system is backward compatible with Jasper's 10-20 system. There are some minor terminology changes: In the 10-20 system, T_3, T_4, T_5, and T_6 are

renamed T_7, T_8, P_7, and P_8 in the 10/10 system, respectively. Pg_1 and Pg_2 are positioned on the pharynges in the 10-20 scheme. We left them out of the analysis since they are challenging to describe quantitatively. Cb_1 and Cb_2 are meant to reside on the head above the cerebellum and are included in Jasper's initial 10/20 scheme from 1958 [28]. We left them out of the UI 10-20 scheme to retain backward compatibility. In the UI 10/20 scheme, 19 places are specified, eliminating A_1, A_2, Pg_1, Pg_2, Cb_1, and Cb_2.

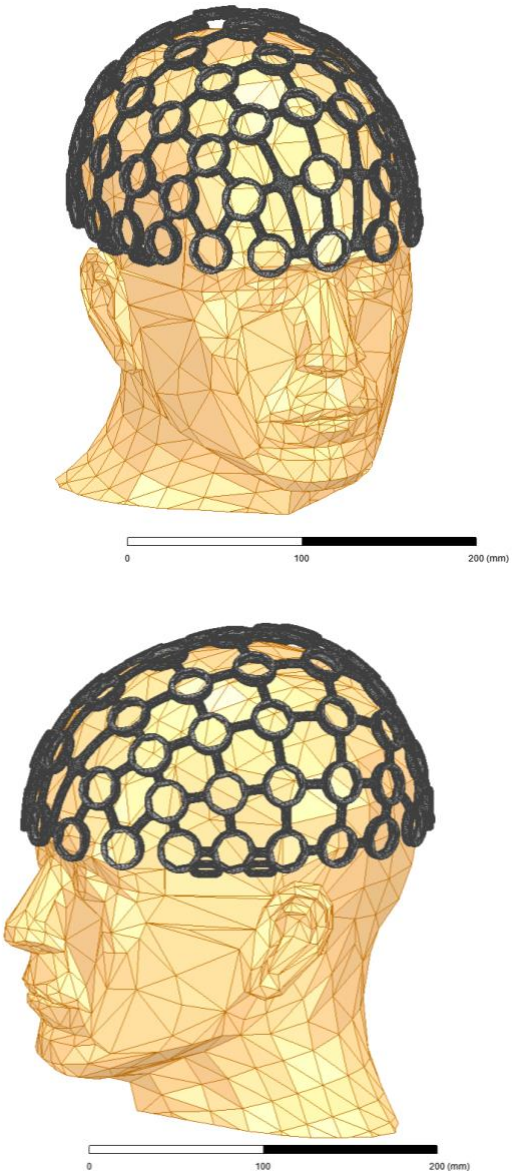

Figure 2.2. A 3-D view of the designed EEG cap based on technical requirements

2.4. EEG Cap 3-D Printing

Because measuring voltage potential from several spots on the skin is such a complicated operation, the use of EEG in practical applications outside of the hospital or laboratory is minimal. Different headset models are being created in various structures to help with this process. The number of channels, sampling rate, electrode connection type,

and headset preparation time is all aspects cited as difficulties with recently developed headsets. There are distinguishing characteristics such as conformability, and the cost is also involved in this procedure.

A unique EEG cap is required to realize a fully untethered EEG recording system and improve electrode implantation configurations. OpenBCI, Compumedics Neuroscan, TMSi, and MyndBand are well-known headset manufacturers. Quick-Cap is a Compumedics Neuroscan device that comes in the shape of an elastic cloth cap.

For the mentioned purpose using 3-D printers can be beneficial. As shown in Figure 2.2, a CAD model of a 3-D view of the EEG head cap with a hexagonal form electrode holder, including holes and interconnections, is designed and constructed. This structure uses an elastic printing element to address the design requirement challenges mentioned earlier. As a result, this construction represents a new version of the 3-D printed EEG cap, which builds on prior work [26]. The design and fabrication of our EEG cap, on which power resonators and other devices can be mounted on the head, is described in this section.

The structural strength is determined by mechanical and electrical testing. The early designs are based on open-source BCI's base 3-D printing file, and we changed the structure to suit our needs [30]. PLA filament material with a diameter of 2 mm was used to print the headset. 0.3 mm layer height, 3 mm shell thickness, 15% fill rate, aided printing, and regular speed printing parameters were employed to print the headset. Since it is not feasible to print the entire system in a single printing session due to the size limitation, the headsets are divided into four pieces: left and front head, left and right rear headpieces, and they were printed separately. Finally, we can join all four components reliably by

developing the closed latching mechanism. In addition, in this way, the headset needs less support material and takes less time to print when it is printed in four sections.

When comparing the printing of complementary parts to a single component, a twin extruder uses the same amount of printing material as a single extruder. Still, the printing time is cut in half. The headset, electrode holder, bolt, nut, and spring made up the entire structure. All of these subsystems should be created considering the other aims in mind. For example, the bolt should be designated to hold the resonators. The same size nuts are used to hold the bolt and the Rx resonator on the Tx array testbed. The proposed structure uses dry electrodes and can be manufactured with any three-dimensional printer. Similar headsets but with a few electrodes are also available in three sizes: small (42-50cm), medium (48-58cm), and significant (60-70cm) [26]. Even while the original 10-20 system only had 21 electrodes, modern methods, such as the "10-10" or "10–5 " system, can provide more channels using up to 256 electrodes. Figure 2.3 Shows the printed EEG cap designed based on a 10/10 universal system.

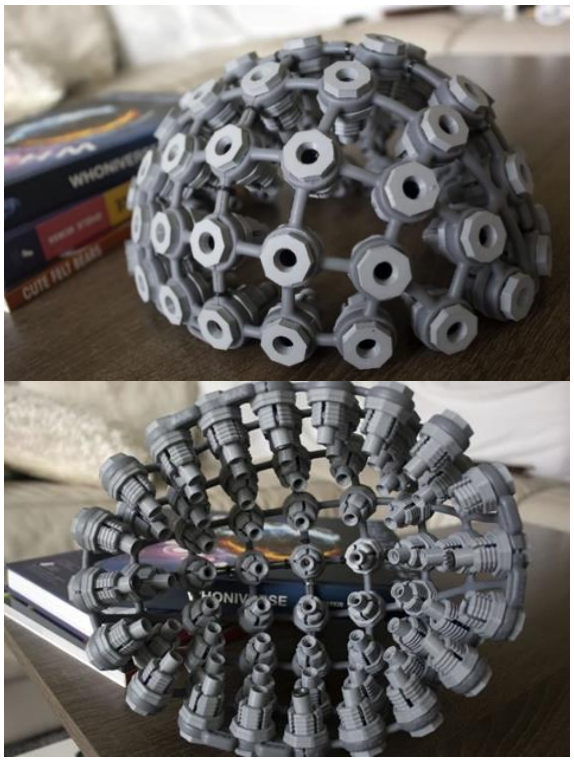

Figure 2.3. 3-D printed EEG cap

Chapter III: Highly Efficient Power Generation, Transmission Conversion Chain

3.1 Introduction

This chapter introduces state-of-the-art practical considerations for designing a highly efficient power generation, transmission, and conversion chain system, PGTCC, to power up the front-end electronics of an EEG signal acquisition system in a portable wireless battery-free EEG cap. To achieve this purpose, a highly efficient and compact resonance-inductive link, multi-resonator wireless power transfer, magnetized materials to boost power transmission efficiency, closed-loop power transmission, and a highly efficient power conversion chain have all been proposed. The proposed design can significantly improve the total efficiency and supply a stable power level for the front-end units, including the EEG signal filtering, noise cancelation, amplification, processing units, and transceivers.

The proposed techniques help us make a fully untethered system without being entirely dependent on the battery as the primary power source for the EEG readout cap. The powering system is equipped with a highly efficient and compact power transmitter system mosaicked by an array of (3×5 or 3×10 or 8×11) Tx resonators in a specific pattern operating at the lowest ISM band of 6.78 MHz (in system-level design). The front-end's power receiver block (Rx) includes multi-resonators mounted around an EEG cap that a subject can wear. Furthermore, taking into account the subject's head, which can assume a variety of positions, a well-designed positioning, and an intelligent power feeding system are designed to balance the efficiency drop caused by misalignment and to involve the most associated resonators with the powering scenario, with the possibility of switching off the extraneous resonators that are not engaged with transmitting and receiving (Tx-Rx) power.

In recent years, remote powering has piqued the interest of certain complex domains of research and innovations. This modality can be used for neuromuscular stimulation and neural recording in biomedical wearable and implantable systems. Utilizing wires and cables for power and data transmission limits the mobility of subjects being tested and makes them feel unpleasant [31-38]. Lightweight wearable devices must be able to communicate and get powered wirelessly for long-term and long-standing operations. The first solution that comes to mind for the limited mobility issue is using batteries as a source of energy to power up the front-end electronics. However, batteries have a short lifespan and might leak heavy metals while being used for biomedical purposes, which could be severely detrimental and cause severe head or brain damage. However, these portable wearable and implantable devices require a reliable energy source to perform their intended tasks. So, considering above mentioned powering issues, it is a significant operational difficulty to power up biomedical wearable systems without batteries or cables. Various power-up alternatives have already been reported, such as using wiring techniques. But, all of these approaches are concerned with restricted mobility, individual comfort, device longevity, and potential human safety risks. In addition, some of these approaches are prone to add noise effects to the captured EEG signal. As a result, procuring enough energy to power up the front-end units remains a challenge. In the case of implantable EEG recording systems, transcutaneous wires or powering cables for power delivery are not recommended since they might expose the patient to health hazards and restrict the patient's movement.

Wireless power transmission (WPT) has proven feasible for maintaining power without replacing batteries. Removing the battery from a portable EEG recording system has another advantage: delivering adequate and stable power levels while keeping safety measures. This approach allows adding additional electrodes on the EEG cap to have better spatial resolution with less crosstalk. Hence, wireless power transfer devices are increasingly being utilized for this

purpose. Inductive and resonant-inductive remote power approaches have become critical for wearable and implantable medical devices.

Two of the most prevalent wireless power transfer (WPT) technologies help us cut the last cord (power wires). More specifically, for the dissertation's intended application, a design of a battery-free and cable-free EEG readout system, WPT has proven to be a feasible method for preserving power while avoiding unnecessary effort for battery change and wet electrode installation and relocation.

The first option is to employ an inductive remote powering link [39].On the other hand, the second option, the resonant inductive or magnetic resonant coupling, requires that the Tx-Rx link be designed to operate at a specific frequency. By including an external capacitor on both sides of resonators, we will have more degree of freedom to adjust the resonance frequency.

The WPT through an inductive coupling principle is straightforward: A Tx coil powered by an oscillating electromagnetic field produces a current in a secondary Rx coil nearby. Under optimal circumstances, the method effectively allows for microlevel (μ) power transmission to tens of kilowatts (KW). The issue emerges when hardware developers discover they must choose between two seemingly opposing modalities for a specific application to power the embedded or implantable or wearable devices wirelessly. Both inductive and resonant- inductive systems have benefits and drawbacks, which will be discussed in the following sections. Due to poor electromagnetic coupling, inductively transferring power has low efficiency. Furthermore, the distance and relative orientation of the powering transmitter coil (Tx), as well as number of element in an array of resonator mounted on the EEG cap as the receiver coil (Rx), and the propagation medium substantially influences the level of received power in practice [40].

Because the research for this thesis is motivated by the need to eliminate data wires, power cables, and batteries (as power sources) from portable and wearable EEG readout systems, the above objective, as well as providing the necessary power for front-end electronics in a highly

efficient manner, are the primary goal of this chapter. The most challenging problem we encounter is optimizing and increasing the parameters of the resonant-inductive power connection for high power transfer efficiency. Another challenge is precisely integrating the power conversion chain (PCC) electronics and components on the EEG cap at the front end to consume less power while still fitting within the volume permitted for the chosen recording system. Moreover, we need to assess power dissipation in the power transmission and conversion chain while supplying energy to different front-end units. So to fulfill this dissertation, we strive to concentrate on developing system and circuit-level solutions for high-performance wireless power transmission and conversion chain circuitries. This procedure begins with the design of corresponding wireless power transferring links, a power conversion chain including voltage rectification and regulation subsystems, power management units consisting of power on rest modules, and the other required electronics.

These low-cost wireless and battery-free EEG recording caps can be used as ambulatory therapeutic assistive equipment or as a fast-diagnostic tool for brain injuries in an accident or battlefield [41]. These are just some of the possibilities that could be produced with this unique design. It should be noted that the number of channels involved in the EEG reading and recording procedure specifies the power consumption limits, which range from 10 mW to 150 mW, depending on the application type. What will be proposed in the following sections can dramatically improve the efficiency of the power transfer link to power on the power-hungry front-end units such as an EEG signal amplifier, filtering, noise cancelation unit, ADC, processing units, and transceivers.

3.2 Wireless Power Transmission for Wearable EEG Readout System

Wearable and implantable gadgets require energy sources to perform their intended tasks. As stated in the introduction of this chapter, it is a significant operational difficulty to power up

biomedical wearable systems without batteries or cables [42]. Batteries are very limited in energy density and device life. They have potential dangers to human safety, individual comfort, integration, and the required space, and also they add more noise to the captured EEG signal. As a result, procuring enough energy to power up the front-end units remains a challenge. In the case of implantable EEG recording systems, transcutaneous wires or powering cables for power delivery are not recommended since they might expose the patient to germs and viruses and restrict the patient's movability [43]. WPT has shown to be a viable method for preserving power without battery replacement. Taking the battery out of a portable EEG recording device has an additional benefit. It allows more energy to be transmitted to the front-end's electronics while maintaining the body's threshold and safety precautions. The proposed EEG cap is a unique setup because of getting the required level of energy wirelessly. More electrodes can be involved in the EEG recording procedure, and we will have a higher spatial resolution.

According to a thorough literature review, wireless power and data transfer technologies will be able to keep an inductively powered EEG readout device operating permanently if needed [44] but with low power transfer efficiency. As a result, inductive remote powering might power EEG recording devices for people tested in enriched environments. However, there is a significant disadvantage to this power transfer method. Because the energy transmitted from the Tx coil is distributed nearly uniformly on all sides, the flux decreases rapidly as the range is extended because of the inverse square law [45]. The Rx coil should be placed as close to the Tx as possible to capture the most substantial magnetic flux.

Furthermore, the total energy level captured by the Rx coil is proportionate to its cross-section, which has been exposed to the magnetic field originating from the Tx side. An Rx coil with equal size to the Tx one, oriented parallel, and horizontal spacing of only a few centimeters, provides the best cross-section. However, alignment is still a significant issue that degrades efficiency drastically. The inductive coupling has low power efficiency due to weak

electromagnetic coupling. Furthermore, many published works had no consistency between the application and design size and standard allocated operation frequency.

MIT researchers examined a technique to enhance the efficiency of wirelessly powered devices in 2007. They are impressed that as the coils in inductive wireless powering are moved apart in terms of distance, the magnetic field flow rapidly diminishes. The flux gets feeble outside a few millimeters (mm), and power transmission is virtually impossible. To liberate power transmission from the inverse square law that dominates inductive approaches, MIT researchers came up with "non-radiating" wireless powering technology [46]. This approach is a new means of delivering power to a target application that may power devices and sensors without wires while also increasing power transfer efficiency.

The theory and the physics of resonant-inductive coupling are complicated, and it is out of the scope of this thesis; however, it is well covered in literature [47-52]. The essential idea is that energy is transmitted from the Tx resonator/resonators in the predefined channel to the next Rx resonator/resonators rather than spreading omnidirectionally from the initial resonator. In practice, in this way of remote powering, energy decreases with distance but not at the same inductive coupling method rate. Using this method, the primary source of attenuation is the resonators' qualification factor Q, not the nature of the transmission modality. So, we can enhance the Q factor to get a higher power transmission efficiency through power link optimization. Furthermore, suppose the Rx resonator has enough extensive cross-section exposed to Tx to receive the required power level. In that case, the resonant inductive link won’t rely on its resonators' alignment like other WPT methods.

When creating a link to transmit the power to wearable or implanted devices, the operation frequency of the WPT is an essential factor that must be considered as the initial design step. The frequency range between 1MHz to 13.56MHz has been recommended for wearable and implantable purposes [53]; however, acquiring the essential electronics and ICs in this range of frequencies

based on what is available on the market would be very challenging for hardware developers. Otherwise, we'd have to engage in complex ASIC designing processes to design different subsystems like power amplifiers, rectification units, voltage regulators, transceivers, ADCs, microcontrollers, etc., regarding the system's specific design requirements.

The simplified schematic block diagram of the proposed wireless and battery-free EEG recording system includes power back-end units, resonant-inductive link, power conversion chain units, power management unit EEG analog front-end, and the other subunits shown in Figure 3.1.

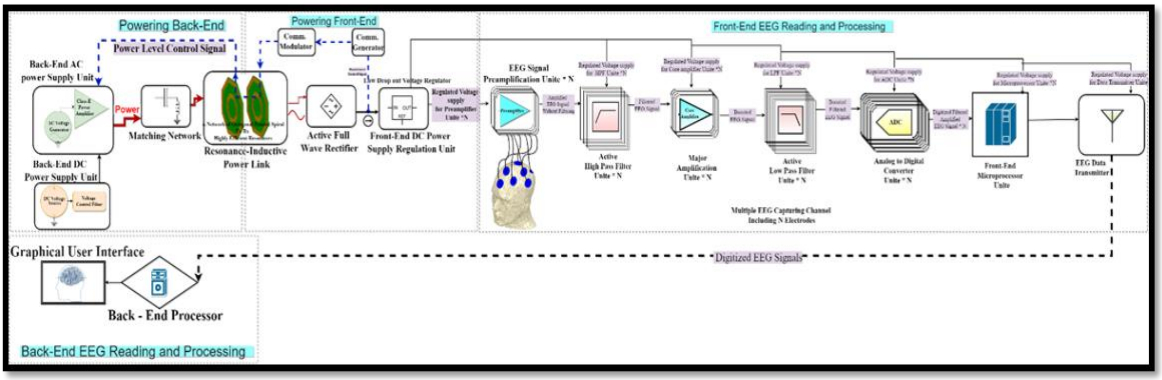

Figure 3.1. The schematic block diagram of the proposed wireless and battery-free EEG recording system

The system is divided into four primary blocks, as shown in Figure 3.1: the back and front-ends powering units and the front and back-ends EEG reading and processing units. The major subsystems addressed in the following sections are contained in these primary components.

3.2.1 Power Generation, Transmission & Conversion Chain

As shown in Figure 3.2, an input control voltage can adjust the operational characteristics of a DC voltage source followed by a voltage control filter. The AC, power supply unit generates the power and then gets boosted by a Class-E power amplifier linked to a matching network between a source and a Tx resonator. The matching network circuitry is often designed to transfer nearly all generated power from the power source to the Tx resonator while having an input

impedance equal to the complex conjugate of the source's output impedance. These components work together to drive the Tx resonator.

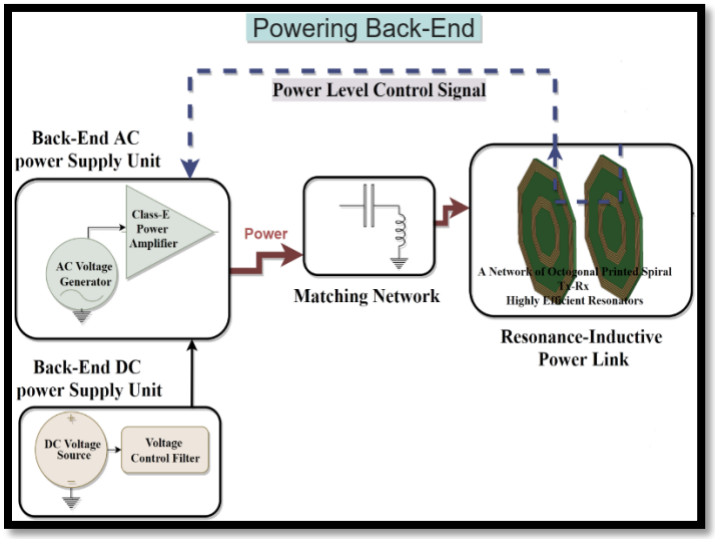

Figure 3.2. Schematic of back-end powering units

The power conversion chain units in the powering front-end, on the other hand, receive the transmitted power from the Tx to Rx resonator to provide a stable and reliable voltage level for the front-end's succeeding components, which include voltage-sensitive ICs, as shown in Figure 3.3. The front-end's power generation, transmission, and conversion chain (PGTCC) consist of a power receiver network that comprises an array of Rx resonators placed in a specific order around the proposed EEG cap plus a full-wave active rectifier that supplies the DC voltage. The AC-DC unit is followed by several low drops out voltage regulators that provide the stable DC voltage levels for different EEG font end’s electronics. A power management unit includes a command generator, and command modulators control the front-end's power level. These are.

The power level control signal contains information about the required power level, which must be transmitted from powering back-end to the powering front-end. Since this system allows more channels to be added to the EEG recording method (if higher spatial resolution is required), the desired power level signal is delivered through the same powering link to the back-end unit. In addition, foreign object detection (FOD) signal or excessive current usage will be reported

immediately through the powering link to the back-end to decrease the transmitted power level or turn off the entire front-end system.

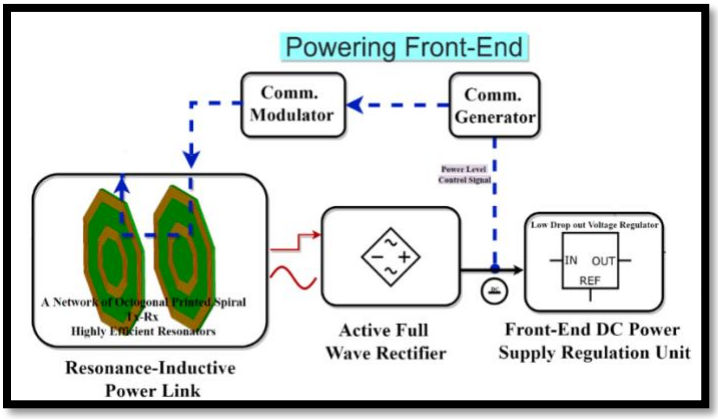

Figure 3.3. The front-end power transmission-conversion chain units

3.2.2 The EEG Front-End Block

The power transmission-conversion chain must create multiple consistent and smooth voltage levels that feed the power-hungry components in the EEG recording front-end unit. As shown in Figure 3.4, the preamplifier unit, active high pass filter unit, core amplifier unit, active low pass filter unit, analog to digital converter (ADC) unit, digital processing unit, and transmitter are all subsystems of the EEG front-end block. While EEG front-end blocks are exclusively designed to capture, amplify, and digitize EEG signals and prepare them for additional processing in the EEG reading back-end, the proposed PGTCC system is anticipated to be compatible with any wearable application with a power output of up to 5W. The power management and data transmission modules, which interchange data between the EEG front-end and the powering front and back-ends, are critical components of the suggested system.

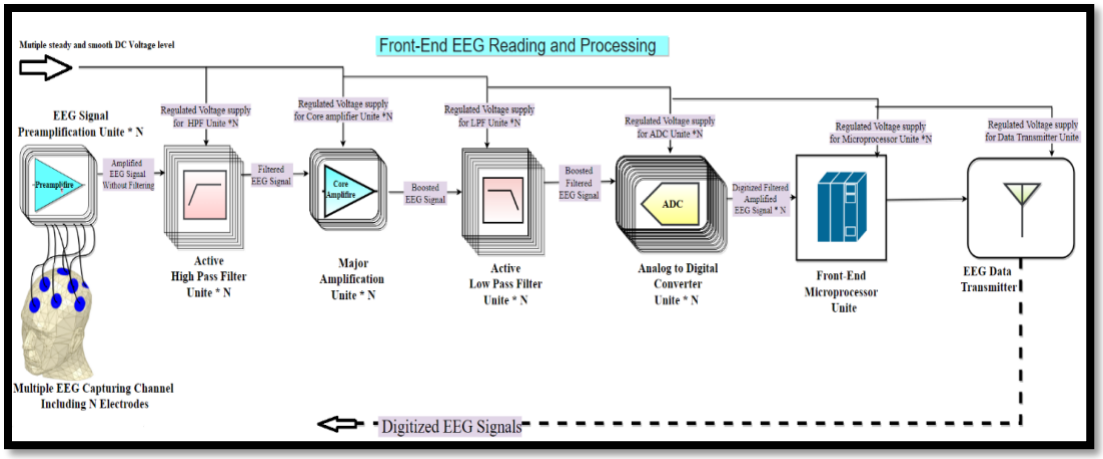

Figure 3.4. The Schematic diagram of Front-End of EEG recording system

3.2.3 Data Transmission

As shown in Figure 3.5, we assume two data communication channels for the suggested system. The first one is a full-duplex communication link through the same power link. This link conveys information about the powering link and the available power level on the front-end electronics. The key reason for contemplating such a link is to improve safety while enhancing power transmission and conversion efficiency at the same time.

Second, the EEG data link, a half-duplex communication channel, sends the digitized amplified and noise-free EEG signal to the EEG read-out system's back-end for further processing. Because of the significant electromagnetic-field absorption in the surrounding skull, skin, and tissues, which increases exponentially with carrier frequency [54], our EEG recording system's half-duplex high-bandwidth telemetry must also be established at the lowest carrier frequencies in the megahertz band.

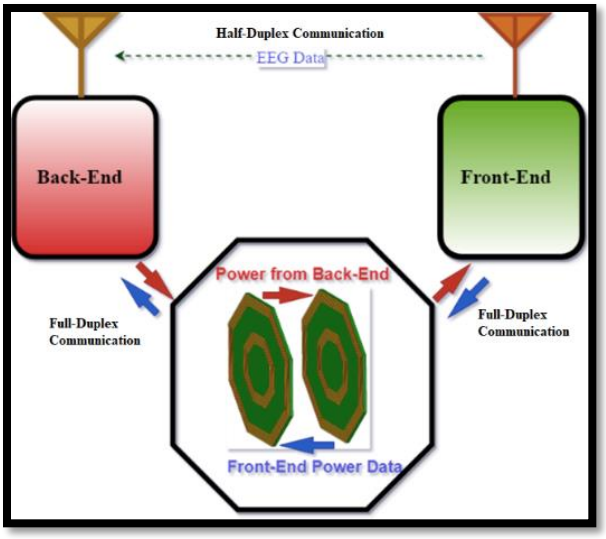

Figure 3.5. Two scenarios for downlinking a and uplink communication in the proposed EEG recording system

3.3 Description and Details of Proposed System

Due to the restricted space and permissible weight of head-worn wearable devices, the suggested methodology is more complicated to achieve than existing wearable systems for human subject use. However, the potential advantages of this proposed setup, on the other hand, make it worthwhile for further research. Figure 3.6 depicts a scale model of suggested wireless and battery-free EEG recording cap powering system for a freely moving subject, such as the human head. The proposed approach can be used for clinical and psychological research and novel therapies and entertainment systems.

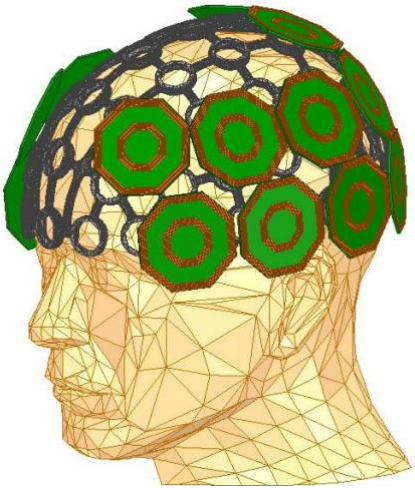

Figure 3.6. Scale model of suggested wireless and battery-free EEG recording cap system

A well-designed power transmission-conversion mechanism constantly supplies power to the battery-less wearable EEG readout system. On the other hand, the suggested EEG cap is designed so that the person being tested is not disturbed during the EEG recording operation.

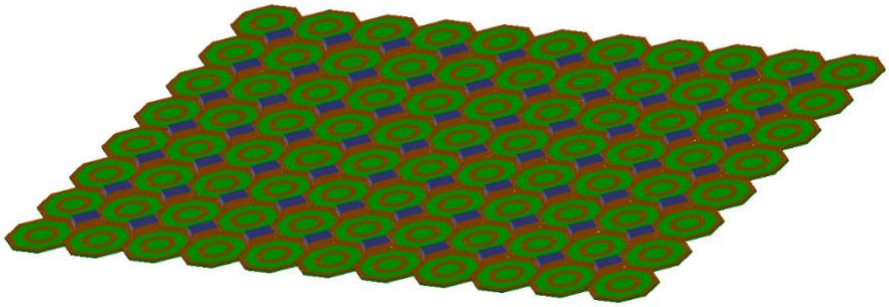

Figure 3.7. The suggested wirelessly powered Tx multi-resonator setup

Figure 3.7 shows the Tx multi-resonator arrangement. In the following chapters, we'll go through the detail of the layout, technical specification of resonators, and the number of resonators necessary for the intended application.

3.3.1 The Constraints of the Proposed Portable EEG Recording Setup

Many factors must be tuned to accomplish an effective wireless power transfer link. Furthermore, numerous elements interact with one another, making optimization procedures difficult and time-consuming. As a primary step, we are designing a highly efficient and compact

multi- resonator Tx- Rx link embedded in a pillow and mounted all around the EEG cap that a single individual can wear.

In this thesis, the powering resonator array embedded in a standard size pillow is called powering pillow. The Tx array is mosaicked by a group of Tx resonators in a specific pattern on the Tx side. A positioning system must be developed to involve the exact right resonators in the powering operation and switch off the extra resonators not involved with powering regarding the head position. In addition, this type of WPT system eliminates resonator misalignment and keeps efficiency close to the same level in the case of lateral and angular misalignment.

According to the latest research, the present marketed wearable EEG cap systems for being used by humans have several issues for being used by end-users and many obstacles in design and implementation for hardware developers. As stated in [55], having an efficient power source for the entire system is one of the most difficult challenges. Real-time EEG recording systems, in particular, which require many samples per minute, demand a relatively high power level. Almost all of the approaches reported so far are based on giving energy to wearable EEG caps via cable [56]. However, using a cable head cap, subjects being examined have limited movement due to the number of the attached wires. Another option is to employ batteries in the proposed portable wearable cap [57]. Because battery cells have a limited lifespan and must be replaced by other limited-life-span batteries when fully discharged, the number and the processing time of required operations may rise.

Furthermore, suppose the application necessitates a high level of power, such as when more electrodes are needed to be involved in an EEG recording operation to get a higher spatial resolution. The battery's lifespan will be restricted to a few minutes [58]. It may be feasible to employ a large battery that can respond to demands, but it increases the overall weight and size of the wearable device. The battery weight even dominates the system's total weight. The best option is to provide energy wirelessly to the wearable EEG cap system without using a battery and cable.

The suggested battery-free wearable gadget fits over a person's head and functions indefinitely. As mentioned before, the power transfer efficiency through the inductive coupling is relatively low in many experiments, so the required efficiency for the EEG recording system is not obtainable through that method. To achieve the best power transfer efficiency (PTE) and an acceptable power level that can be delivered to load PDL, we developed a multi-Tx-Rx resonant inductive link for our setup. Note that because the size and shape of the wearable system are constrained, the Tx resonator is similarly affected by the size of the wearing cap. Moreover, the Rx resonator's size affects the coupling coefficients *k* between the resonators. The link's coupling coefficient and the resonator's quality factor Q determine power transmission efficiency. Even though the resonators are designed to have a high-quality factor Q, on the other hand, the coupling coefficient K limits the power transfer efficiency to some extent [59].

Furthermore, owing to the intended set-up's test-bed and considering an individual's head position, there must be at least a 6 to 8 cm space between the Tx and Rx resonators. It should be noted that the distance between the Tx and Rx resonators, as well as any misalignment between them, has a negative impact on power transfer efficiency, so the powering system blocks, which include a power amplifier, command generator, and command modulator, should be designed in such a way that any PTE drops are addressed immediately. As seen in Figure 3.6, the proposed EEG cap has several Rx resonators to avoid power transfer efficiency due to lateral and angular misalignments. A set of Tx resonators has been mosaicked precisely on the powering pillow in the back-end. The problem of wireless power transmission becomes significantly more difficult when higher power transmission efficiency is necessary to limit the transmitted power level, and this matter might affect the health of the individual being tested. The resonator size and mutual inductance coupling must be optimized to acquire excellent power transfer efficiency from the wireless power transmission link. Finally, powering links data transmission is a significant design

issue in this study. A constant power supply is required to respond to the system's energy needs as multiple power-consuming components such as amplifiers and transmitters require it.

To reduce total energy usage, consider a low-power consumption solution, such as utilizing a limited number of EEG electrodes or highly low-power consumption ASICs for the EEG recording procedure. This method may compensate for low power transfer efficiency, but it reduces the resolution of collected EEG signals. So it wouldn't be beneficial for capturing EEG data of high quality. As mentioned in section 3.2.3, one possible solution for lowering power consumption is establishing two separate data links. One of these two links controls the power level, which can be accomplished via the same power link, and the other via a short-range communication data link that does not require a power amplifier for the EEG data transmitter unit. So by this way, because of the short distance between the EEG cap and the EEG signal recording and monitoring back-end unit, this strategy reduces the system's overall power consumption.

We might face another technical challenge in the power link design procedure; for example, the induced voltage is relative to the wireless powering frequency. So the resonator's self-resonant frequency should be less than the wireless power transmission frequency. Therefore, the resonator structure and geometrical specification dominate the WPT operation link (outside diameter, number of turns, track width, etc.). The resonators' geometrical configuration, shape, and size are crucial for fully covering the length and width of the standard size pillow on which the person being tested lays his head and receive enough power for the worn EEG cap.

The suggested wearable EEG system's energy consumption alters the architecture of the WPT powering link. The magnetic field strength diminishes as the distance increases (with the ratio of the inverse cube), which directly impacts the remote powering efficiency or the received power level. Although low-power-consumption electronics are necessary on the front-end side to minimize the energy required to power the front-end unit, we should not sacrifice captured signals quality to integrate the internal design of low-power consumption modules. The rectifier and

voltage regulator, active filters, and even the data transmitter could be highly efficient in limiting energy loss and power consumption and maximizing Tx's incoming transmitted energy. Designing or selecting other essential modules that directly impact the quality of signals based on their power consumption measures, such as ADC or microprocessor, should not be taken as the primary consideration for the design.

The proposed EEG signal recording system's total power usage, including the 16-channel EEG recording device, sensor interfaces, and communication, is projected to be under 50mW. Due to the testbed specifications, which include Rx resonators placed on an EEG cap, a pillow, and a planar Tx resonator mosaicked in a specific pattern, wireless power transmission must be accomplished over more than a 6 cm distance.

Furthermore, an intelligent wireless powering link must follow the individual's head movement and distribute the power effectively and efficiently in a testbed. A power control block and a switching devices adaption mechanism keep the suggested power quality at a predefined value. Finally, a highly efficient, mid-range data transmitter is proposed for uplink data transmission. The mentioned challenges are considered while designing an appropriate and optimal wireless powering link.

3.4 Far-Field Vs. Mid-range Near Field Powering

Electromagnetic waves, ultrasound, and magnetic field transmission can all transfer electricity. However, the decision is based on several factors, including the required energy level as link budget, the distance between the powering back-end Tx resonator and the front-end Rx resonator, and the power transmission conditions. Generally, there are two primary ways for an electrical device to get power from a distance. The first method is to obtain energy from available sources in the environment. The other solution is to install a power source dedicated to supplying power to the gadget [60]. The energy harvest techniques may create power levels from artificial

and natural sources [61]. The piezoelectric and thermoelectric effects can be exploited to produce electrical energy from movement. Electricity generated by the environment, such as solar, wind, or waterpower, seems a viable option [62]. Ambient heat as an energy source for remote sensors located within a structure might be advantageous. Using current radio-frequency (RF) transmissions, such as those present in TV and radio transmissions, mobile phone communications, and wi-fi, would be the most feasible technique for energy harvesting [63]. However, the biggest issue with ordinary far-field energy harvesting is the deficient level of captured power (often only a few $\mu W/cm^2$ [64]). A larger receiving antenna gives more power; however, this technology is incompatible with miniature remote sensors. As a result, given the present technology, this alternative is not feasible [65]. This section compares different modalities to select the best option with higher efficiency so that the EEG readout system can run with the lowest amounts of power available.

Since power harvesting is unfeasible, another alternative is to install an energy source that is mainly designed to deliver energy to the gadget [66]. Non-radiative technology is used in near-field transfer to transmit power over small distances utilizing inductive or capacitive, or resonant inductive coupling methods [67]. One alternative for far-field transmission is to employ available technology via electromagnetic radiation to achieve the required controlled power that is supposed to be delivered to the load [68]. This technique can now transfer electricity over distances of up to 50m, and the issue is that the transmitter must be in a direct line of sight with all receivers. This is ineffective if the receivers are dispersed over a multi-room facility with features that block or severely attenuate electromagnetic radiation. With the arrival of 5G technology, which uses beamforming to target broadcast signals to specific receiving devices, this problem is somewhat alleviated. This novel technology can give a more reliable and quicker transmission power and improve far-field power transmission efficiency for transmitters. However, given current

technological breakthroughs, the power demand of applying beamforming technology in the transmitting circuitry of a remote sensor array appears to be unfeasible for the years ahead [69-71].

A more reliable and straightforward alternative is to extract power from a transmitting electromagnetic field using slot array antennas to generate a field of sufficient power. So the remote devices can obtain enough power to exercise their function. Other antennas, such as microstrips, cannot transmit high levels of power owing to their structure, so they are not useful for this purpose. [72-73]. Power transmission technologies with greater power efficiency per unit surface area might be handy to wirelessly power up the electronic devices. However, the energy required to drive the current technology electronics cannot get satisfied by far-field radiation power harvesting methods

The technological limitations and the FCC clearance and certification requirements will create considerable barriers for the designer wishing to include remote power capabilities. However, it is likely to be changed shortly. Far-field power transmission systems operating in MHz and GHz frequencies in the ISM band [74-77] can be the following power harvesting sources. The ISM-designed base system allows power transmissions that are an order of magnitude greater than Wi-Fi or other commonly used radio transmitters, dealing with these low field densities. The disadvantage is that an ISM-based system will require a custom transmission system rather than the current Wi-Fi network [80-92].

The received power is affected by the distance between the source and receiving devices, and received power has a square-root relationship with coupling distance. As a result, there'll be a considerable power dissipation while working across broad spaces. With careful design of the receiving antenna, receiver electronics, rectifier, and tuning for maximum efficiency, it is feasible to send sufficient energy to a low-power consumption device [93]. Realistically, the technology exists to transmit a few milliwatts to a sensing device for a few minutes via pulsed power transfers across 10 meters. To open up far-field power transmission to a broader range of applications, the

issue is to transmit much higher quantities of energy levels to enable quick charging and high energy power transfers [94].

An energy source's field strength (H or E) diminishes with a propagation path length in far-field radiation. The magnetic field intensity (H) is highly dependent on a range of transmission and decreases with $1/d^3$ in the near field, corresponding to a 60 dB decrease each decade of transmission range. In the far-field zone, however, the electrical field intensity (E) is inversely dependent on the distance between Tx and Rx (1/d), resulting in only a 20 dB drop every decade [95]. As a result, electromagnetic waves are used to successfully transport power across further distances, but the energy level is kept extremely low due to many safety issues.

Furthermore, by employing the GHz range of frequency in the far-field, the power reception antenna may be scaled down to mm ranges, making it appropriate for many applications [96]. As part of the dissertation, we aimed to provide the necessary power for the EEG cap through the power harvesting method. We fabricated three different types of slot array antenna to evaluate the far-field radiation and energy harvesting. Still, unfortunately, none of these methods can be helpful due to energy levels and safety measures. Anyway, in this section, we try just the outline of what we had been done so far. The received power for far-field radiation can be calculated as follow

$$P_r = P_t G_t G_r \left(\frac{\lambda}{4\pi d}\right)^2 \tag{3.1}$$

The received power level, the transmitted power level, the transmitter antenna gain, the receiver antenna gain, the wavelength of the electromagnetic wave, and the distance between the two antennas are all represented by P_r, P_t, G_t, G_r, and d, respectively.

For a 12 cm distance at 2.42GHz, P_t G_t (PEIRP) of roughly 1W is required [95]. Furthermore, due to SAR restrictions set by regulation [96-99], the maximum value of PEIRP is limited. When the permeability of open space is zero, the received and transmitted power levels are P_r and P_t, respectively.

3.4.1 Design, Analysis, and Optimization of the Array of Axial Rectangular Slots on a Cylindrical Waveguide

3.4.1.1 Far-field power harvesting

The literature extensively analyzes different antenna topologies with different shapes and designs. They all show distinctive and systematic design procedures that characterize their proposed antennas [106-108]. In the scenarios, optimization techniques are applied to enhance the antenna's parameters and study the effect of different dimensions and materials on parameters [99]. Deployment, manufacturing techniques, and production procedures have been widely investigated at microwave frequencies for the other application domains, ranging from medical wearable applications to radars [100-103]. Many different antenna types are used in radio systems with specialized properties for specific applications [104-105]. Based on the target application, antenna parameters, including desired frequency, gain, bandwidth, impedance, and polarization, and the antenna's shape and configuration should be calculated and designed [106]. Despite confronting the constraints and many limitations in antenna design, novel methods have been proposed to improve the antenna parameters and optimize antenna size [107]. However, the slot array antennas have attracted significant attention due to their inherent valued characteristics of high radiation efficiency, high gain, wide bandwidth, and low losses. Consequently, they may be preferable to reflector and patch antennas [108].

The design of slot arrays goes back to 1948 when Stevenson [109] carried out the preliminary analysis on resonant slot arrays for the first time. This analysis was initially proposed by Oliner in the study on non-resonant slots [110]. However, Elliot was the one who presented the design equations for slot arrays on a rectangular waveguide [111]. In the study by Oraizi et al. [112], a design algorithm for an edge slot array is proposed with non-uniform spacing on a rectangular waveguide. Slotted arrays on a cylindrical waveguide were initially studied by Wait et al. [113]. In [114], Shin et al. studied the radiation from multiple circumferentially opened

rectangular slots displaced along the longitudinal direction. M. Sharafi Masouleh et al. in [115] extended Shin's work by proposing a similar method but for circumferential slots placed on a cylindrical waveguide. In this work, the design equations are proposed for rectangular slots elongated along the cylinder's axis, forming a linear array with the intent to broaden bandwidth and hence the realm of practicality. With their high gain, efficiency, mechanical strength, and absence of spurious radiation from their feeding system, slot array antennas have been deployed effectively in multiple radar and communication systems applications. They have many other practical implications [116-119]. However, the slot array antenna, axially placed on a cylindrical waveguide, is not well-covered in the literature despite all these research endeavors.

This section proposes a method to design narrow axially rectangular slots on a conducting cylinder. Compared to the circumferentially disposed slot arrays [120], the advantage of this design is its wider bandwidth [121]. The method follows the approach introduced by Elliot [121], which devised a recursive procedure for creating longitudinal slot arrays by considering the external mutual coupling. Three main variables for the array design and pattern synthesis are considered: slots L's length, center-to-center distance "d," and their disposed angle φ_0. The least-squares method is applied to synthesize the radiation pattern with specified sidelobe level and the array input impedance matching. The minimization of the error function is performed using a genetic algorithm (GA) and the conjugate gradient (CG) method. Through this work and for the first time, an analytical approach is proposed for both purposes, i.e., the design equations and the synthesis of an array composed of rectangular slots arranged along the central axis of a cylindrical waveguide. The results are verified using the HFSS commercial software, and the measurements are obtained via the proposed prototype built for this purpose.

3.4.1.2 First and Second Design Equations

An array of narrow rectangular waveguide slots on a cylindrical waveguide is shown in Figure.3.8. Each slot is of length L, while the center-to-center distance between two consecutive

slots is d. Two design equations are derived for the array based on the physical characteristics L, d, and arch length (φ_0). From these two equations, both the slots' mutual and self-impedance/admittance information defines the array's characteristics. For the pattern synthesis problem, an error function is also developed. The developed error function comprises impedance matching, array pattern synthesis, and slot design equations. Its minimization is achieved by the combination of the GA and CG methods. Due to the orientation of the slots, the circular waveguide is assumed to operate in its dominant mode TE11. Every slot is excited by a tangential electric field on its aperture as follows:

$$E_{\varphi} = E_{\tan} = \frac{V_n^s}{w_n}\cos\left(\frac{\pi z}{L_n}\right), \qquad \frac{L_n}{2} < z < \frac{L_n}{2} \tag{3.2}$$

With

$$E_s = E_{\varphi}\bar{u}_{\varphi} \quad , \quad E_Z = 0 \tag{3.3}$$

Where W_n and are the width and length of the n'th slot, respectively, with V_s being the maximum voltage distributed across the n'th slot.

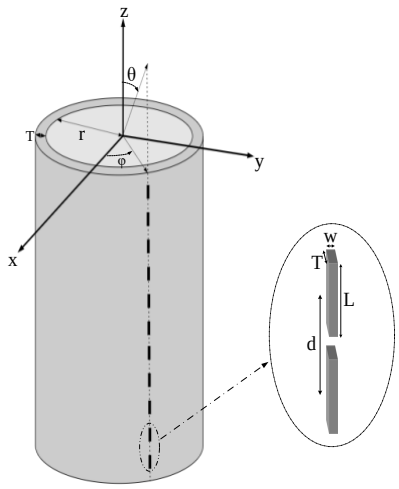

Figure 3.8. An array of narrow rectangular slots along the axis of the cylindrical waveguide

Following the procedure that is presented in appendix A, the two design equations are defined as follows:

First Design equation:

$$\frac{z_n^a}{z_0} = Kf_n\frac{v_n^s}{I_n} \tag{3.4}$$

Second Design equation:

$$\frac{Z_n^a}{Z_0} = \frac{\eta^2}{2} Z_0 |K|^2 \frac{f_n^2}{Z_n^{d,a}} \tag{3.5}$$

Where:

$$F_n = \frac{L_n \cos\left(\frac{\beta_{11} L_n}{2}\right) \cos(\varphi_{0n})}{(\pi^2 - (\beta_{11} L_n)^2)} \tag{3.6}$$

and

$$K = -j \sqrt{\frac{4\pi h^2 J_1{}^2(ha)}{\omega \mu \beta_{11} Z_0 \left[\int_0^a \left(\frac{J_1^2(h\rho)}{h^2 \rho} + \rho J_1'^2(h\rho)\right) d\rho\right]}} \tag{3.7}$$

In these equations, I_n , V_n^s and Z_n^a are the mode current, the slot's voltage, and the active impedance of the n'th slot, respectively. As $Z_n^{d,a}$ is the active loaded dipole impedance, defined as follows:

$$Z_n^{d,a} = Z_{nn} + Z_n^b \tag{3.8}$$

Where Z_{nn} is the axial slot impedance, and Z_n^b is the mutual impedance between the two axial slots. The complete derivations of Z_{nn} and Z_n^b are presented in Appendix B. It should be noted that based on the two design equations, the length of the slots and their azimuthal locations can be determined. These equations work in the microwave range of frequency, but we need to consider the upper bands' skin effect and waveguide power loss. The next step is to define the error function. This will be done based on an equivalent circuit model for the proposed array.

3.4.1.3 The Error Function

The error function comprises the three terms of impedance matching, slot design equations, and pattern synthesis. A single error function is constructed for each term, and all the error functions are summed up to produce the final error function.

For active impedance matching, the least-squares method minimizes both the real and imaginary parts.

$$\varepsilon_{\text{Matching}} = W_1 \left|\text{Re}\left(\frac{Y_n}{G_0}\right) - 1\right|^2 + W_2 \left|\text{Im}\left(\frac{Y_n}{G_0}\right)\right|^2 \tag{3.9}$$

Where W_1 and W_2 are weigh functions of the error function.

For linear array longitudinal slots in a cylindrical waveguide, the equivalent circuit model with a matched load in its end is shown in Figure 3.6.

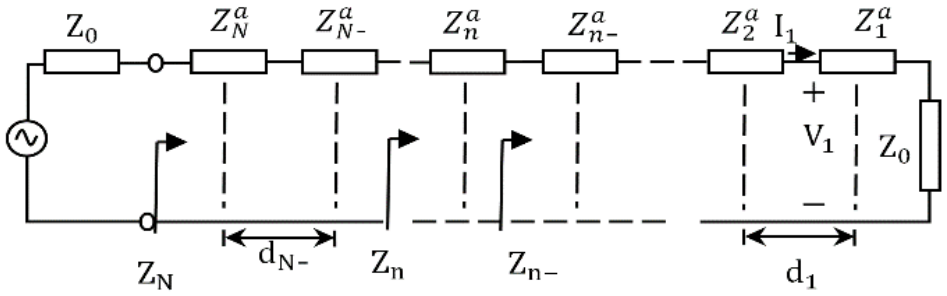

Figure. 3.9. The equivalent circuit of axial slot array

In Figure 6.3, the equivalent circuit of the linear traveling wave axial slot array is modeled by a transmission line with a series impedance. As seen, I_i is the constant parameter across the slots, so the slot's voltage distribution which is proportional to the cosine form of voltage, just depends on the length of the slot.

3.4.1.4 Slot Design Equation Error Function

According to the design procedure described in [135], the normalized admittance of the n'th slot is :

$$\frac{Z_n}{Z_0} = \frac{K_1 f_n^2}{Z_n^a} + \frac{\left(Z_{n-1}/Z_0\right)\cos\beta_{11}d_{n-1} + j\sin\beta_{11}d_{n-1}}{\cos\beta_{11}d_{n-1} + j\left(Z_{n-1}/Z_0\right)\sin\beta_{11}d_{n-1}} \tag{3.10}$$

Since the current of two successive elements can be written as :

$$I_n = I_{n-1}\cos\beta_{11}d_{n-1} + jI_{n-1}Y_0\sin\beta_{11}d_{n-1} = I_{n-1}\left[\cos\beta_{11}d_{n-1} + j\left(\frac{Z_{n-1}}{Z_0}\right)\sin\beta_{11}d_{n-1}\right] \tag{3.11}$$

Considering equations (10.3) and (11.3), the following relationship can be established:

$$\cos(\beta_{11}d_{n-1}) + j\frac{Z_{n-1}}{Z}\sin(\beta_{11}d_{n-1}) = \frac{V_n^s}{V_{n-1}^s}\cdot\frac{f_n}{f_{n-1}}\cdot\frac{Z_{n-1}^a/Z_0}{Z_n^a/Z_0} \tag{3.12}$$

Furthermore, the error function can be written as:

$$\varepsilon_{DesignEqs.} = w_3\left|\sum_{n=2}^{N}\cos\beta d_{n-1} + j\frac{Z_{n-1}}{Z_0}\sin\beta d_{n-1} - \frac{V_n^s}{V_{n-1}^s}\cdot\frac{f(\varphi_n,L_n)}{f(\varphi_{n-1},L_{n-1})}\cdot\frac{Z_{n-1}^a/Z_0}{Z_{n-1}^a/Z_0}\right|^2 \tag{3.13}$$

3.4.1.5 A Relation for the Radiation Pattern of Axial Slot Array

The radiation pattern of an array of axial slots on a cylinder as defined in [105] is replicated here in conformance with the proposed design approach:

$$E_\theta(r\to\infty) = j\omega\mu\frac{e^{-jkr}}{\pi r}\sin(\theta)\sum_{m=-\infty}^{\infty}e^{jm\phi}j^{m+1}f_m(\omega) \tag{3.14}$$

$$E_\phi(r\to\infty) = -jk\frac{e^{-jkr}}{\pi r}\sin(\theta)\sum_{m=-\infty}^{\infty}e^{jm\phi}j^{m+1}g_m(\omega) \tag{3.15}$$

The Fourier transforms $f_m(\omega)$ and $g_m(\omega)$ can be obtained by using equations (2.3) and (3.3) and also invoking the appropriate boundary conditions:

$$f_m(\omega) = 0 \tag{3.16}$$

$$g_m(\omega) = \frac{\bar{E}_\varphi(m,w)}{\sqrt{(k^2-w^2)}H_m^{(2)'}\left(R\sqrt{k^2-w^2}\right)} \tag{3.17}$$

$$\bar{E}_\varphi(m,w) = \sum_{p=1}^{P}\sum_{n=1}^{N}\frac{V_{pn}L_{pn}\cos\left(\frac{wL_{pn}}{2}\right)}{a\left(\pi^2-(wL_{pn})^2\right)}e^{-j(m\varphi_{pn}+wz_{pn})} \tag{3.18}$$

Where P denotes the number of columns of the axial slot. The far-field components consist of E_θ and $\bar{E}_\varphi$. Therefore, the E-plane pattern is considered only with the E_θ field component.

For the appearance of some null points in the pattern, we considered the asymmetrical modified Taylor pattern as in [125]:

$$h_k = \frac{\sin(\pi u)}{\pi u} \frac{\prod_{n=-(\hat{n}_L-1)}^{\hat{n}_R-1} (1-u/\hat{u}_n)}{\prod_{n=-(\hat{n}_L-1)}^{\hat{n}_R-1} (1-u/n)} \tag{3.19}$$

Where h_k is the asymmetrical modified Taylor pattern, and R and L denote the right and left components of the Taylor pattern, respectively. The unit normal factors for both the right and left parts are as defined below:

$$\hat{u}_n = \hat{n}_R \left[\frac{A_R^2 + \left(n - \frac{1}{2}\right)^2}{A_R^2 + \left(\hat{n} - \frac{1}{2}\right)^2} \right]^{1/2} \quad n = 1,2, \ldots \ , \hat{n}_R - 1 \tag{3.20}$$

and

$$\hat{u}_n = -\hat{n}_L \left[\frac{A_L^2 + \left(n + \frac{1}{2}\right)^2}{A_L^2 + \left(\hat{n} - \frac{1}{2}\right)^2} \right]^{1/2} \quad n = -(\hat{n}_L - 1), \ldots \ , -2, -1 \tag{3.21}$$

Where$R = \ 10^{(SLL/20)}$, $A = \frac{1}{n}\cosh^{-1}(R)$, and with $A_L$and A_R define the left and right side lobe level (SLL), respectively. For A_L and A_R, we use the left SLL and right SLL, respectively. The pattern's main lobe elevation angle depends only on the spacing of the slots, and this condition happens only when higher-order grating lobes appear in the pattern. Otherwise, the change of the elevation angle is about 1 to 3 degrees. Having defined the radiation pattern function using the method of least squares, the error function can be defined as:

$$\varepsilon_{Synthesis} = \sum_{k=1}^{K} w_k \left(|F(\theta_k) - h_k|\right)^2 \tag{3.22}$$

Where

$$F = 20\log\left(\left|\frac{E_\theta}{E_\theta Max}\right|\right) \tag{3.23}$$

It is worth mentioning that the error function depends on the spacing between the slots and the slots' dimensions. The error function in total is the combination of the errors determined through equations (3.9), (3. 13), and (3.22) as follows:

$$\varepsilon_{\text{Error Function}} = \varepsilon_{\text{Matching}} + \varepsilon_{\text{DesignEquations.}} + \varepsilon_{\text{Synthesis}} \quad (3.\ 24)$$

The following sections show how the most desired pattern can be obtained through optimization.

3.4.1.6 Synthesis of Slot Array

To determine the error function, both the space between adjacent slots and the length of the slots are assumed to be identical. These assumptions will result in the simplicity of the calculation process to minimize computational time. On the other hand, the equality of length of slots makes the amplitude of voltage distributions in the slots even and equal. A cylindrical array with twenty-two axial slots consisting of two rows of 11 elements is designed, as shown in Figure 10.3. The length of the slot and the spacing between slots were optimized. The error function is minimized by combining a genetic algorithm (GA) with the conjugate gradient (CG) method. The parameters are as given in Table 1.3. The spacing between adjacent slots is equal to 19.88 mm, and the width and length of the slots are equal to 3 mm and 10.95mm, respectively. Hence, optimizing these parameters aims to yield better impedance matching and the desired pattern shape.

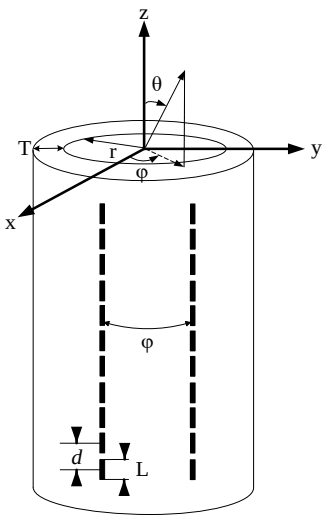

Figure 3.10. Two-column narrow rectangular slot array on a cylindrical waveguide

Table 3.1 optimized parameters of the antenna

Antenna parameters	N: Number of slots	Two by eleven
	W: Slot width	3.00 mm
	T: Thickness of wall of the waveguide	2.80 mm
	R: Radius of waveguide cylinder	11.26 mm
	Operation frequency	9.00 GHz

For comparative purposes, the pattern of the slot array as obtained by the method of least squares (MLS) and HFSS software simulation (at 9 GHz in XZ-plane for φ= 0) is shown in Figure 3.11. As shown in Figure 11.3, more specifically about the main beam, the MLS design pattern matches the HFSS simulation pattern, and the sidelobe levels are almost between the specified design constraints. The inability to reach the specified sidelobe levels is mainly due to internal mutual coupling, which is a factor that was not counted in the design. The assumption of sinusoidal field distribution in the slot is another possible source of error. The VSWR of the array simulated by HFSS at the input terminal of the cylindrical waveguide is shown in Figure 3.12, reflecting that the high bandwidth of the designed antenna is about 200 MHz.

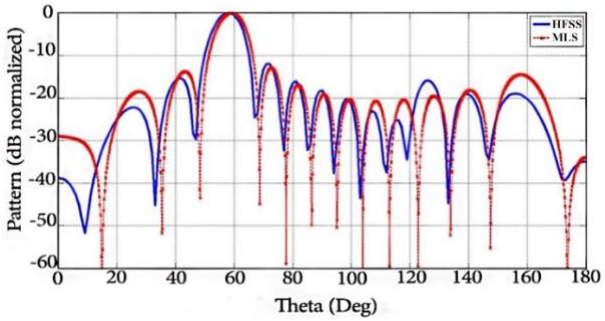

Figure 3.11. E-plane pattern cut comparison between MLS and HFSS at 9GHz in XZ-plane for φ= 0

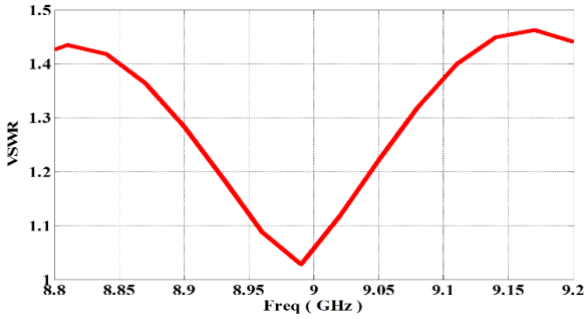

Figure 3.12. Simulated results of VSWR

3.4.1.7 Fabrication, Measurement, and Comparison

As shown in Figure 3.13, a typical axial slot array antenna consisting of two rows of 11 slots on a cylindrical waveguide is fabricated for the test, and measurement results are provided to clarify the accuracy of the acquired design equations. The fabricated antenna consists of a coaxially fed monopole, a slotted cylinder, and an SMA termination. The antenna has two ports, and a 50-Ohm male pin SMA as a terminator coax connector plug (TCCP) is used to absorb the reflected waves on one side. In contrast, the other port serves as the excitatory terminal of the antenna. The coaxially fed monopole, which has a protruding inner conductor of 6.9882 mm length, excites the TE_{11} mode into the slotted circular cylinder. The SMA termination used in the measurements demonstrates SWR below 1.25 at 9 GHz. Figure 3.14 illustrates the fabricated slot array antenna's simulated and measured return losses. The measured return loss is less than -17 dB from 8.9 GHz to 9.1 GHz.

The difference between the simulation and measurement results, as seen in Figure 14.3, can be attributed to milling machine fabrication process tolerance. Our theoretical model could not mimic the reflection, possibly introduced by the coaxially fed monopole and the SMA termination. The antenna radiation pattern is measured and compared to the simulation pattern at 9 GHz, as shown in Figure 15.3. The results obtained for the prototyped antenna have good compliance with the design goal, that SLL is lower than -15dB in the H-Plane. As the graphs in Figures 3.11, 3.14, and 3.15 reveal, there are strong agreements in the measured and simulated outcomes' overall behavior, which verify the proposed method's accuracy. The proposed antenna structure, designed based on acquired equations, can be used as a phased array antenna to scan a range of space. This feature comes out of the antenna’s high bandwidth, which by changing the frequency from one to another in a specific field, the angle of the main lobe gets altered consequently, and it can sweep a range of space to find targets. It is worth mentioning that since the amplitude of the voltage distribution is even across the waveguide, it is possible to change the beam angle but just by frequency changing. Moreover, more slots can be placed around the waveguide for designing wideband omnidirectional slotted-waveguide antenna arrays. However, it should be noticed that because ripples amplitude is proportional to the number of slots distributed around the circumference of the waveguide, increasing the number of slots just for the sake of having an omnidirectional pattern increases the level of ripple in the omnidirectional radiation pattern (azimuthal plane).

Table 3.2 Characteristics of structure optimized parameters and desired pattern antenna

Antenna parameters	N: Number of slots	Two by eleven
	W: Slot width	3.00 mm
	T: Thickness of wall of the waveguide	2.80 mm
	R: Radius of waveguide cylinder	11.26 mm

	Operation frequency	9.00 GHz
Optimized parameters	L: Slot length	10.95 mm
	d: Space of slots	19.88 mm
	$\varphi_{1\&2}$: Slot offset	-13.55^0 & 27.43^0
Characteristics of the desired pattern	Modified Taylor pattern to have SLL_L= -15 dB SLL_R= -12 dB	

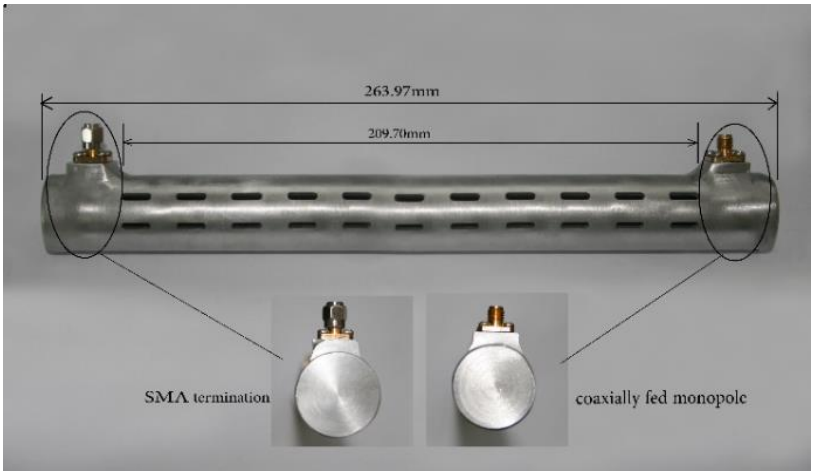

Figure 3.13. Fabrication of the 22-slot antenna (two rows of 11 elements). All slots are identical, and the distance between two adjacent slots is d=19.88 mm.

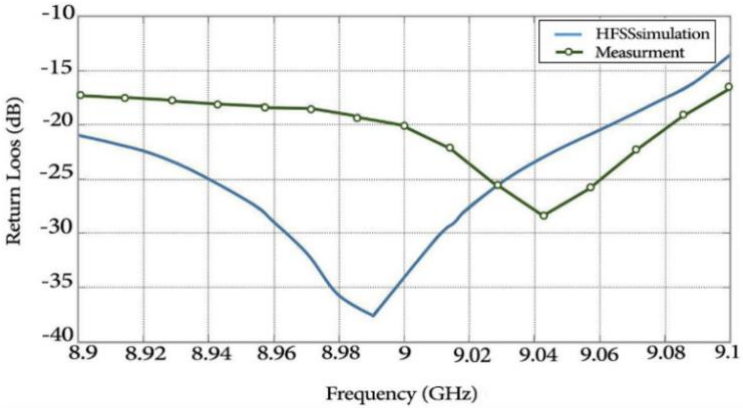

Figure 3.14. Measured and simulated return loss (S11) versus frequency

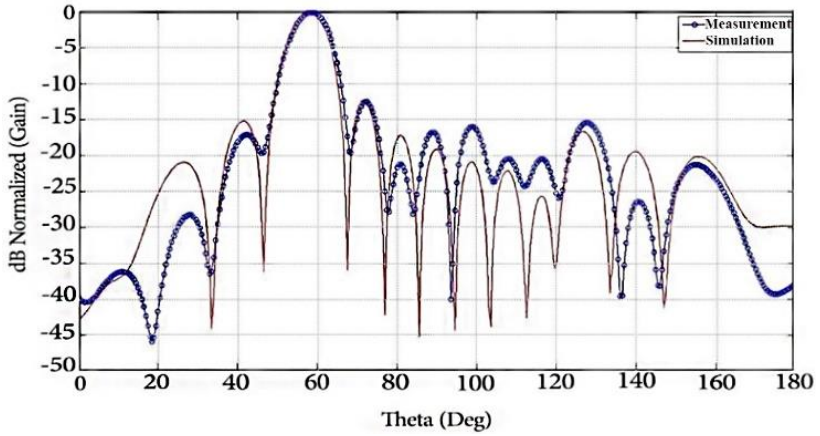

Figure 3.15. Measured and simulated radiation patterns for an axial slot at operating frequency f = 9 GHz

The proposed section expanded on the least-squares method to synthesize axial slot array on a cylindrical waveguide for the dominant mode TE_{11} and analyzed the radiation from axial slots on a cylindrical waveguide. Using Elliott's method [115] as a baseline, and for the first time, the design equations were presented and expanded for the traveling wave mode with the use of equivalent circuits for the axial slot array antenna. Subsequently, the geometrical dimensions of the slot array on the cylindrical surface were determined by minimizing the appropriate error functions. This minimization led to accurate pattern synthesis impedance matching, formulation of the relevant design equations, and minimization of power losses. With the proposed antenna design, the computational requirements were optimized. The method is also advantageous because it combines the determination of slots' parameters and impedance matching with the array pattern synthesis, leading to a quick design with higher accuracy.

Moreover, a design example was presented to demonstrate the effectiveness of the proposed synthesis method on a cylindrical slot array. Full-wave simulation software HFSS was used to verify the proposed design procedure. To verify the simulation's accuracy and practical

feasibility, measurements were taken on a prototype design of an array of axial slots on a cylindrical waveguide, and good correspondence with the theoretical predictions was achieved.

The study indicates that the far-field power harvesting did not yield desired results; we opted for near-field wireless power transmission in chapter IV.

Chapter IV Near-Field Wireless Power Transmission

4.1 Inductive or Resonant Inductive

Tesla discovered that an alternating current in a wire loop produced an alternating magnetic field, which caused an alternating current in a secondary coil. The induced AC might be engineered to accomplish meaningful things by adding a payload to the secondary windings [126]. The level of wireless power transmission ranges for diverse systems can range from a few millimeters to a few centimeters, depending on industrial, civil, and biological applications [127-131]. Wireless power transfer is becoming an exciting subject in analog front-end design, and companies are gradually integrating innovation into various products [132-135].

The WPT principle is straightforward: a coil or resonator powered by an oscillating electromagnetic field produces a nearby current in a secondary coil or resonator [136-139]. There are two effective modalities for wireless power transmission, inductive and resonance inductive coupling. But there is an issue here for us to decide which kind of WPT modalities can be more consistent for the proposed portable wireless and battery-free EEG readout system. So, we must choose between two seemingly opposing ways to power the front-end electronics wirelessly. There are two conflicting regulatory standards and three different technologies, and both approaches are embraced by the opposing regulatory agencies [140-141]. As we found in the literature [142-144], they are more complementary than rivals, so we should get familiar with both to make the best decision based on the target application. One can debate the merits of competing protocols, but unification is the most realistic possibility based on prior standards. For designing a highly effective WPT link, two highly essential characteristics must be considered: first, power transfer efficiency PTE, and second, the power delivered to load PDL, the latter of which is sometimes more important than the first [145-166].

4.2 Wireless Powering Standards and Protocols

Qi and A4WP define two protocols as standard measures for wireless power transmission. By concentrating Qi's efforts on the more established inductive wireless powering technique and encouraging its development in smartphones, it can be said that Qi has pulled ahead of the competition in terms of technology. The AirFuel Alliance was formed in June 2015. The AirFuel Alliance, along with the Alliance for Wireless Power (A4WP) and the Power Matters Alliance (PMA), have established an inductive wireless powering specification [166-167]. The operational frequency of the powering back-end for low-power WPT (up to 5W) based on Qi standard is between 110 and 205 kHz, while the standard transmission frequency for medium-power WPT (up to 20w) is between 80 and 300 kHz [168-179].

4.2.1 An efficient Wireless Power Transfer Link's Requirements Considering the Target Application

The following conditions must be addressed in developing the EEG signal recording system:

1. Because the total efficiency of the entire set-up is strongly dependent on the Tx-Rx transmission link efficiency, it's crucial to improve the powering link's efficiency from the Tx power amplifier to the load. This measure guarantees that the mounted active electronics subsystems on the front of the EEG recording system are always operational. Coupling distance variations between transmitter (Tx) and receiver (Rx) resonators, load fluctuations on the Rx side, and detuning of the Tx and Rx resonators owing to misalignment all have a negative impact on both the PTE and PDL [180-192].

2. Due to safety concerns and the power level of front-end components, wideband and reliable data transmission links must be developed on the same power link. The real-time status of the front-end subsystems is comprehensively relayed to the back-end powering unit through such a powering link. Powering link can provide sufficient power to current involved active electronics

or add more channels to the EEG reading operation. In emergency scenarios, it shuts down the entire system [192-195].

3. Frequency selection is one of the most important factors to consider when designing a power transmission network. Strong electromagnetic-field absorption by the tissues raises the tissues' ohmic losses .as a result, the tissue temperature rises, which can be detrimental. So, lower frequencies in the MHz range are favored for target applications. However, on the other side, choosing lower frequencies may increase the resonator's size. Considering the the equations provided in literature through the conventional design procedure, the resonator size would be too large to be used for biomedical purposes. It's also worth noting that the front end's LC-tank circuit's resonant frequency should be the same as the powering back end transmitter Tx carrier frequency, f_0 [195-198].

4. Because of the significant electromagnetic-field absorption in surrounding tissues, which increases exponentially with carrier frequency, the half-duplex high-bandwidth telemetry data link must be established at the lowest carrier frequencies in the megahertz range [199-203].

5. For the design of a resonant-inductive link, first, we should calculate the inductive resonance coupling parameters. The inductive-link power-transfer efficiency is determined by the mutual inductance M_{mn} of the coils (in the case of having four loops M_{23} in our recommended design) and the quality parameters Q. The resonators' geometry, which includes their relative coupling distance, orientation, and the number of turns, is commonly recognized to impact these two parameters [204-206].

6. Regarding resonator configuration with skin effects, resonators could be wire-wound or lithographically formed on a planar conductive surface, such as a printed circuit board (PCB) or a micromachined surface known as Litz wire, to help reduce the resonator's resistive losses due to skin effects, which is especially important at higher carrier frequencies [207-210].

7. power transfer efficiency PTE and power delivered to load PDL are two key factors that must be fully understood to accomplish the design standards. The wireless powering link for the EEG recording system must provide an appropriate power level. The adequate power level must be delivered to the load (PDL) while retaining high power transfer efficiency (PTE). The power link must be designed to have the maximum possible PTE to fulfill regulatory and safety requirements. On the other hand, PDL is dependent on the electronics' power consumption in the EEG front-end unit and the power amplifier PA in the powering back-end circuits, which should have generated adequate power and delivered it to the load. As a result, the powering link should provide adequate PDL while considering all technical constraints of the power amplifier (PA) in the back end [211-214].

8. In addition to the considerations mentioned above, we must also consider heat dissipation on either side of resonators. Electromagnetic field exposure can cause additional heat dissipation in the mediums involved in the power transmission procedure. Power amplifier technical constraints and frequency cross-talk with neighboring electronics and circuitries must be considered for the optimum link design [215-217].

4.2.2 Technical Concerns Regarding the Power Delivered to Load in the Design Procedure

There are two primary concerns regarding PDL and PTE:

1. Increasing the source voltage, Vs, to increase the power level delivered to the load (PDL) may sound acceptable. However, it might reduce driver efficiency in the back end, necessitate larger transistors in the source power amplifier, and complicate meeting technical measures.
2. When space is limited (particularly on the EEG cap), the resonator's dimensions must be optimized to a modest size. The size optimization will directly impact the PDL. So, the Tx-

Rx loops in the resonators must have been adjusted to generate the highest possible voltage on the load to yield higher PDL.

4.2.3 Single or Multi-Loop Resonator

Considering Figure 4.1, the current passing through the first loop L_1 of the Tx resonator creates a magnetic field, which induces current to flow through the L_4 of the Rx resonator. The induced current's value is proportional to the $L_{eq.\,Tx}$ and $L_{eq.Rx}$ inductance values [221-224].

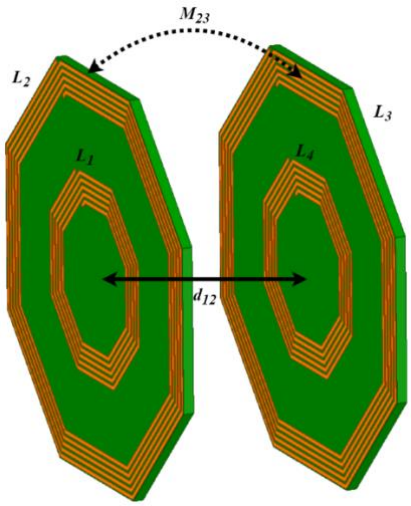

Figure 4.1. Coupling distance d_{12} and mutual inductance M_{23}

After deciding the frequency allocation, resonator geometries are one of the most critical criteria in determining link power efficiency. Most previous designs used coils in inductive coupling made up of single or insulated strands of filament wire. The latter version, also known as Litz wire, assists in the decrease of skin-loss resistive effects by expanding the circumferential area of the wire, particularly at higher frequencies. On the other hand, wire-wound resonators require specialized technologies to be batch-fabricated or reduced from a size perspective. In wireless power transmission, the spiral inductor is the most basic and significant element, and they are usually made in square, rectangular, octagonal, hexagonal, or circular forms. Many studies have examined spiral inductors using various methodologies, such as those reported in [225-228]. Inductance calculation for square spiral inductors is extensively reported in the literature [229-232].

However, when dealing with PSCs, the design methodologies developed for resonators made of 1-D filament wires are only helpful in getting the optimal lumped values for the inductive coupling. Considering Figure 4.1, the mutual inductance, M, of two linked resonators is inversely proportional to d^3, where d is the resonators' center-to-center distance when entirely lined in parallel planes. When d is relatively large, or the resonators are misaligned, i.e., when M is extremely small, the powering source unit must increase the power level to transmit the required power to the load. It depends directly on the PDL factor.

High power transfer efficiency is a factor that reduces heat dissipation inside resonators and tissue exposure to an AC magnetic field. Inductive coupling, which has lower efficiency, may create extra heat loss in wearable devices. According to our findings through simulations, using the 4-loops approach improves power transfer efficiency at large d at the expense of a considerable loss in power delivered to the load. So we decide to use the 4-octagonal loops approach. However, this proposed arrangement still lacks an in-depth comparative circuit analysis based on the coupled-mode theory CMT. Circuit designers use another theory to compare the 4-loops resonant inductive coupling to the 2-resonator equivalent, called the reflected load theory [242], which is more recognizable to the designer unwilling to get involved with the physics behind the power link.

To choose the most suitable configuration for power transmission units which consists of two resonators, we face a lot of restrictions. The majority of the design limitations are set by the resonant inductive link application, while the resonator manufacturing and production process determine the remainder.

To improve power transmission efficiency, the outer diameter of the resonator on the Rx should be increased to the maximum size allowed by the application. Using lithographically designed or wire-wound resonators would have been the first step in deciding which resonator to use. As detailed in [233] and [234], the line width (w), line spacing (s), outer diameter (D_{out}), and fill factor (the ratio of the difference and sum of a PSC's inner and outer diameters) are geometrical

characteristics that impact circuit parameters such as quality factor Q and coupling coefficient k, and subsequently the PTE.

4.2.4 Resonator Specification

Resonant Inductive coupling power link design and geometrical optimization based on power transfer efficiency for biomedical applications have also been widely investigated in the literature [238-240]. For inductive or resonant-inductive coupling, planar spiral resonators (PSRs) are often utilized in wearable applications. These specific spiral topologies allow us to have the length of the needed track in lower frequencies. This section describes a new and straightforward way of enhancing the coupling efficiency of printed spiral circuits that we used as L in a resonator with the desired shape. We need to consider both the design restrictions of the application and the resonator manufacturing technologies accessible in our lab. The inductive coupling parameter to create a resonant-inductive link should be calculated as the first step. The dominant factors in defining the inductive-link power-transfer efficiency are the mutual inductance between the resonators M (in the case of four loops M_{23}) and the quality factor Q. The Tx/Rx resonators' geometries and their relative coupling distance, orientation, and the number of turns are widely acknowledged to influence remote powering links' performance. The nominal values resonator specification, such as innermost diameter, outermost diameter, and the coupling distance, varies depending on the application.

4.2.5 4-loop resonator power transmission link

The 4-loop resonator power transmission link represented in Figure 4.1 may is designed to achieve high power transfer efficiency and power delivered to load. The circuit's power transfer efficiency can be calculated by reflecting the resistive components of each loop from the load towards the primary resonator loop and then summing the percentage of power delivered from one

level to the next until it reaches R_L [244]. In 4-resonator resonant-inductive links, there is a trade-off between attaining optimum power transfer efficiency over short distances and maintaining adequate power provided to load over long distances.

A range of parameters is evaluated to determine which resonant-inductive power transfer link is suitable for the target application. Important parameters that have an impact on PDL are the driver output resistance (R_s), source voltage (V_s), nominal coupling distance (d_{12}), misalignments tolerance, and resonator geometries. When the power transferred to the load is little, or Rs is great, power transfer efficiency (PTE) is an appropriate metric. But when the power amplifier driver is constrained, supplying sufficient power to the load becomes difficult. Another reason to employ a 4-loops two-resonator link is because of size restrictions. Different configurations such as multi-resonator linkages can be used when the resonators are loosely coupled. In this condition, the coupling distance varies considerably, or a large amount of power is delivered to the load. Finally, after evaluating the pros and cons of the proposed EEG cap, multi-resonator linkage is the ideal solution. Since in our target application, efficiency is crucial, load power consumption is minimal, resonators are loosely attached, and relative spacing and alignment are stable, which could be covered by considering a few resonators on either side the multi Tx- multi Rx is proposed as an optimal power link configuration.

4.2.6 Resonator Configurations

The spiral inductor is the most fundamental and crucial component in near-field wireless power transmission based on Tx-Rx systems. Because our proposed powering system is predicted to run at 6.78MHz, the track lengths will be pretty long, and the single loop will not meet the other design limitations. As a result, employing spiral forms allows us to have enough inductance in a small space. We follow the method reported in [233] by increasing a shape factor to obtain the inductance for the desired configuration, the octagonal arrangement.

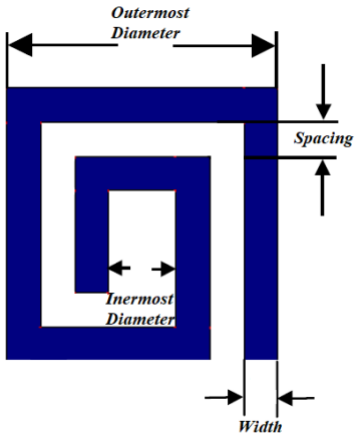

Figure 4.2. the layout of a square spiral inductor

The required equations for the geometrical calculation are provided in [233]. Spiral inductors of different shapes such as rectangular, octagonal, or circular can be converted to square spiral inductors by keeping the parameters unchanged. Their inductance can be calculated simply by multiplying a configuration coefficient with the inductance of a square spiral inductor.

4.2.6.1 The Octagonal Spiral Inductor's configuration coefficient and analytical calculations

The layout of an octagonal spiral resonator and its structural parameter is shown in Figure 4.3. When comparing the inductance of square and octagonal spiral inductors, the configuration coefficient factor of the octagonal spiral inductor ranges from 1.06 to 1.17, with a 10% variation. If the configuration coefficient factor is 1.11, the maximum error is less than 5% [233].

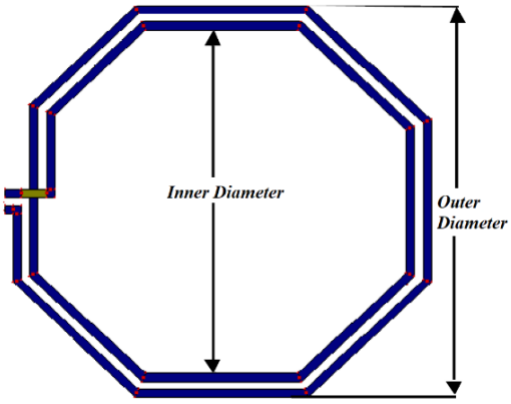

Figure 4.3. the layout of an octagonal spiral inductor

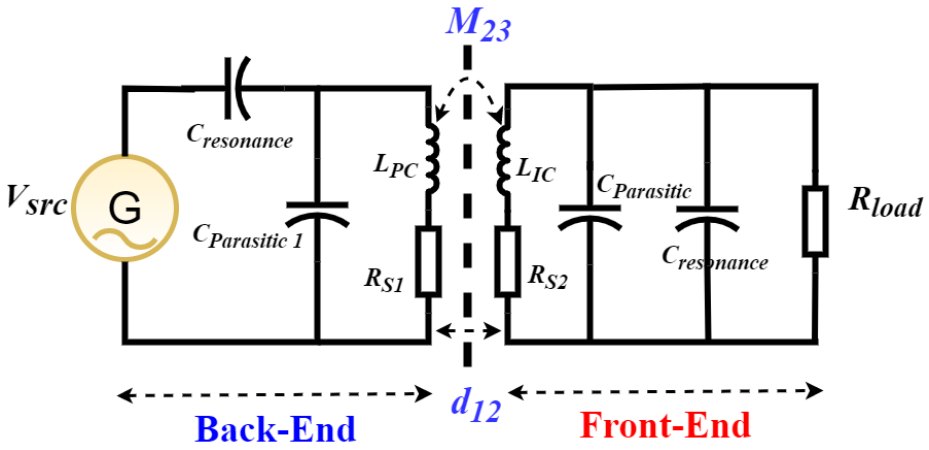

Figure 4.4. Circuit model of powering link by reflected load theory

Mutual inductance M is the essential factor in wireless power transfer link efficiency. When dealing with 3-D PSCs, what is reported in the literature is insufficient to predict the intertwined effects of scattered inductive, resistive, and capacitive components on power efficiency. Finally, optimum wireless power transfer efficiency can be attained by maximizing the resonator coupling coefficient and the quality factor. So, the resonator can be appropriately designed to achieve optimum coupling and quality factors.

As seen in Figure 4.4, the self-inductance of the powering (Tx) and wearable (Rx) resonator in two-loop powering links are L_{PC} and L_{IC}. The Tx and Rx resonator's series resistances and parasitic capacitances are represented by R_{s1}, R_{s2}, $C_{parasitic1}$, and $C_{parasitic}$, respectively. $C_{Resonance}$ is the capacitance of resonant frequency on both sides. Furthermore, M_{23} and R_{Load} stand for mutual inductance and load resistance. The capacitances Cres1 and Cres2 adjust the remote powering link to the resonant frequency. When both LC tanks are set at the same resonant frequency, $f_0 = \frac{1}{\sqrt{L_{eqTx}C_{eq\ Tx}}} = \frac{1}{\sqrt{L_{eqRx}C_{eq\ Rx}}}$ The highest PTE and PDL for the resonant inductive coupling may be reached.

4.2.6.2 Finalized Design of Resonator

Our proposed resonator design is different from what is given in the literature, which consists of a single TX -Single RX power link. Considering Figure 4.1, two octagonal shape resonators make up the Tx-Rx link for the powering block. First, we try to improve power transfer efficiency by developing $L_{3,}$ the outer loop of the Rx resonator, then we improve $L_{2,}$ which is the outer loop of Tx, to increase the amount of power transferred to the load.

4.3 The Optimum Conformal Wireless Power Transmission line

The coupling distances vary considerably when the subject's head rolls to the left or right on the pillow. A high power level must be delivered to the load to keep the front end running to compensate for the PTE drop. However, if Tx_Rx misaligned more than the normal range, the front-end electronic system shut down entirely. So, we proposed our novel powering arrangement called the intelligent multi Tx-multi Rx linkage for weakly coupled links due to severe misalignment. The multi-resonator linkage is ideal for maintaining efficiency at almost the same level. The Rx resonators can still get loosely connected to Tx by implementing the mentioned idea. By considering a few resonators with the precise structure and intelligent feeding on either side, relative spacing and alignment have a good tolerance.

Additionally, because these resonators' characteristics are application-specific, the wireless powering link shall be customized appropriately based on our purpose. The power transfer efficiency is substantially related to the inverse of the distance ($1/d^3$) in the magnetic inductive coupling; the spacing between the resonators is one of the essential criteria for effective power transmission. As a result, the gap between the powering Tx and Rx resonators should be kept short.

In recent decades, numerous techniques for improving the power transfer efficiency have been explored, including geometrical optimization of two, three, and 4-loops resonant-inductive links [255-258]. The configuration and the shape of the resonator (Figure 4.5) significantly

influence power transfer efficiency. Several resonators surround the EEG cap, as illustrated in Figure 4.6. On the other hand, these structures appear to be enough for the Rx multi resonators that are expected to be installed on EEG caps. Due to the distinctive form of the proposed EEG cap and the design constraints imposed by the necessity for precise positioning to adjust for Tx-Rx misalignment, octagonal resonators are chosen for maximum power transfer on the front-end side.

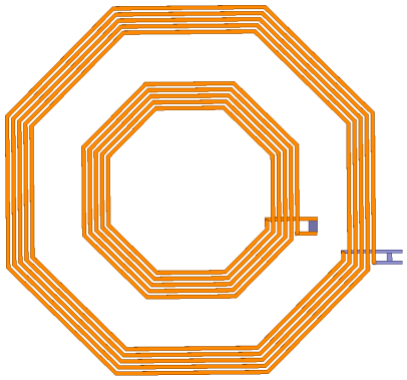

Figure 4.5. Octagonal spiral inductor designed for being installed on EEG cap

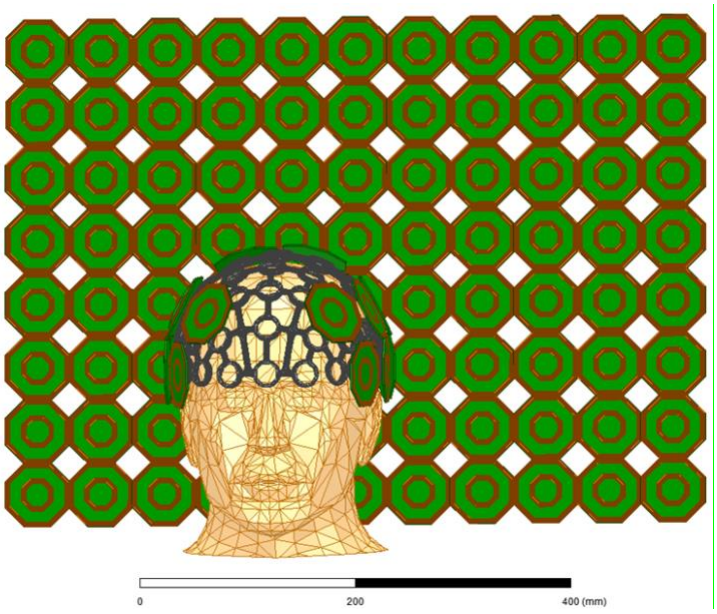

Figure 4.6. Proposed testbed for recording EEG signals

The WPT wireless powering technology employs four loops that dynamically adjust to changing environmental and circuit conditions, lowering resonator size and improving total power efficiency from the backend driver output to the load in Rx. According to the loosely linked

resonators, the distant powering channel efficiency (the Tx-Rx link) dominates the power transfer efficiency of the entire system. The circuit model of the octagonal resonator for the wireless power transmission link is shown in Figure 4.7.

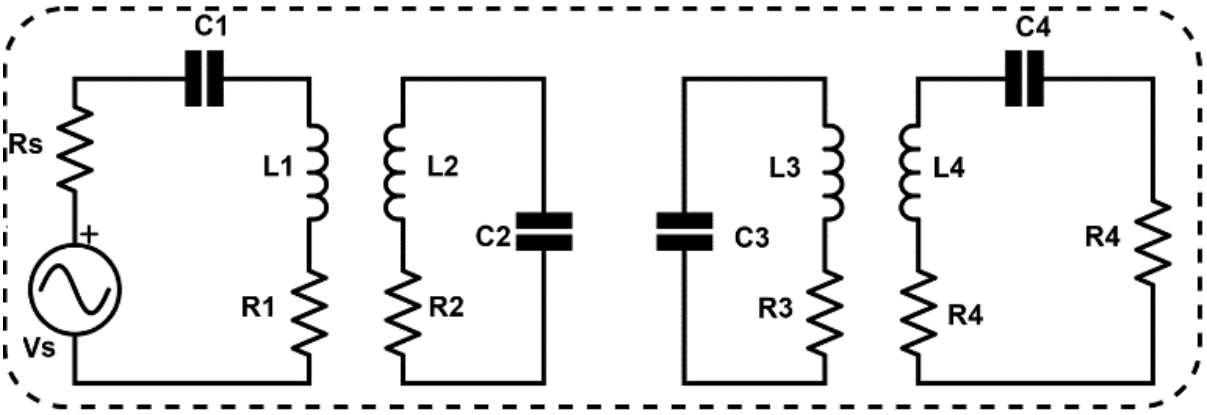

Figure 4.7. Circuit model of suggested octagonal shape Tx-Rx resonators

4.3.1 Calculation Methods Proposed Conformal Wireless Power Transmission Link

After a thorough literature review, we determined that any powering link should be built purely to benefit the target applications. Power transmission effectiveness depends on how well the Tx and Rx tank circuits are tuned at the operating frequency. The coupling coefficient k of the resonators will be important in boosting the power transfer efficiency once the distance between the resonators is significant. Furthermore, resonator power dissipation has a substantial impact on power transmission efficiency. Topological modification of the proposed WPT link is necessary to produce a highly efficient wireless powering link. However, several resonator characteristics must be optimized, including the number of turns, conductor width, the spacing between tracks, outermost and innermost radii, etc. However, all of these optimization strategies can improve resonator coupling. We may need to incorporate magnetic material in our design to improve efficiency further.

To deliver the most optimum power level for the electronics in the front end, we choose one of two methods to design the most optimum resonator geometries. First, the resonator variables

may be determined using the given mathematical formulae. This method reduces computing time. However, the outcome will not always be identical to the ideal result. Second, to determine the desired resonators based on application and operating frequency, a 3-D high-frequency modeling program provides a better outcome and fits the obtained data from measurement. The calculation time, on the other hand, would skyrocket. Based on our experience in designing the desired link, it is better to acquire the best resonator geometry by combining the abovementioned methods. The mathematical formulae conduct the rough estimation of size and resonant frequency. In addition, a high-resolution simulator is used to fine-tune the resonator designs. Each resonator's geometric parameter is evaluated in the analysis procedure to get the best resonator shape.

As a result, using mathematical formulas and HFSS tools, the lumped model elements of the wireless powering channel, displayed in Figure 4.7, are derived. The proposed link's power transfer efficiency is calculated by the formula reported in [232]. The resonators ' physical parameters can be optimized by modeling software such as (HFSS). The 3-D model of the proposed powering setup using the HFSS simulator is shown in Figure 4.5. Finally, the operating frequency is determined, and the resonators are carved on a circuit board (PCB). We can change the capacitor values to tune the operation frequency. The fittest capacitor from the capacitor bank may be added to the resonance tank when the operation frequency of the power link gets detuned.

4.3.2 Link’s PTE Enhancement Using Magnetized Strips

The data link must have a high-frequency carrier (over 50 MHz) to send EEG data via a broadband data link; raising the frequency of the high-level power carrier for the power link might induce severe temperature rises in the surrounding tissues (due to excessive power loss). We also need an estimate for the data link budget. The power carrier frequency should be kept below 20 MHz, as stated in previous sessions. On the other hand, finding appropriate electronics in the market to generate high power within the allocated frequencies is a big challenge. After careful study, we chose 6.78MHz, the lowest ISM band, as the powering carrier. However, prototyping a

highly efficient power link with a reasonable size resonator that can be compatible with the application is quite difficult due to the low frequency. The use of ferrite materials between the loops at the back of the substrate concentrates more of the magnetic field into the resonator (Figure 4.8). It steers the radiation in a specific direction, improving resonant inductive coupling significantly. Other modalities have been reported in the literature, such as utilizing magnetized material to cover the distance between the resonators using a powder-blasting method or a polymer-Mn-Zn alloy combination. Both technical ways need intricate patterning through lithography and won't help system-level design [253-256]. [257] describes a technique involving inserting a ferrite rod into the core of a printed planar spiral resonator to improve coupling efficiency dramatically. In most biomedical implants, a planar spiral coil is used. We are interested in having a magnetic material that could be made on a flexible substrate for this dissertation, but it appears to be outside the scope of this research. However, it must be mentioned that as long as the operating frequency is less than the ferrite's hysteresis response frequency, the ferrite powder may magnetize itself and modify the spatial distribution patterns of the magnetic field. As a result, increasing the mutual inductance between the two resonators with the ferrite strips confirms the coupling enhancement. This section of the dissertation shows how a simple method may dramatically improve the resonant-inductive coupling efficiency of a resonator in the form of a printed spiral circuit.

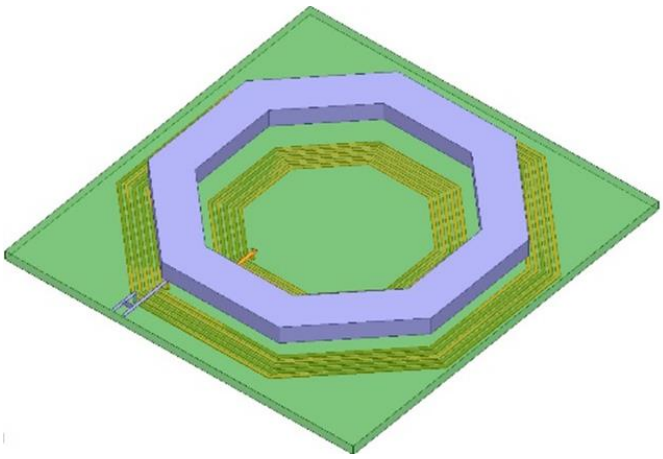

Figure 4.8. CAD model of magnetized loop placed on PCB substrate backside between the L_1 and L_2

As seen in Figure 4.9, the power efficiency declines dramatically as the distance between the Tx and Rx rises. Increasing the voltage source Vs can somewhat compensate for the loss, but there is another effective technique to handle this issue. The induced open-circuit voltage is increased when a porous ferrite layer is added between the loops, and the efficiency rises again. Thanks to a ferrite coating, the mutual inductance between two resonators is improved by 42 percent (Figure 4.10). Because adding a ferritin layer to a planar spiral, the board is still a planar manufacturing process. The present way to increase the resonant-inductive coupling efficiency of resonators may be more effective than alternative options.

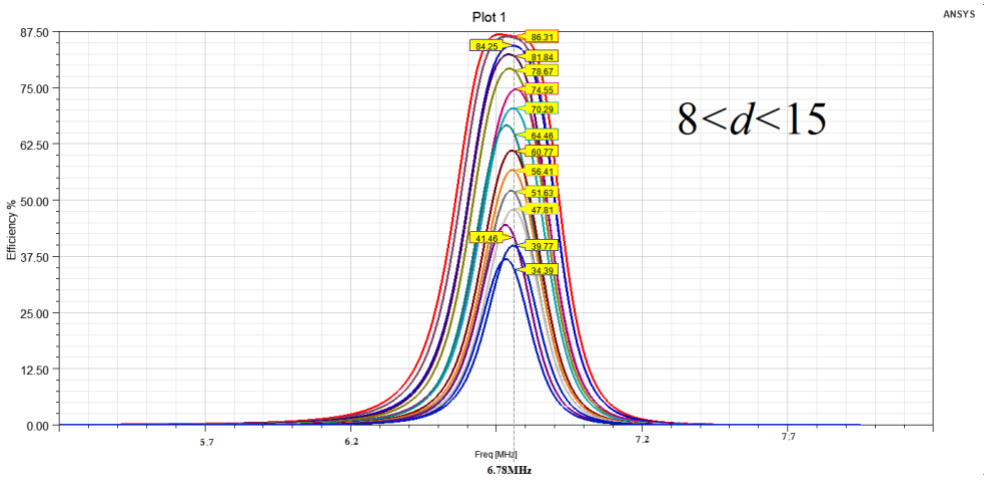

Figure 4.9. PTE drop when the coupling distance increases between 8 to15mm

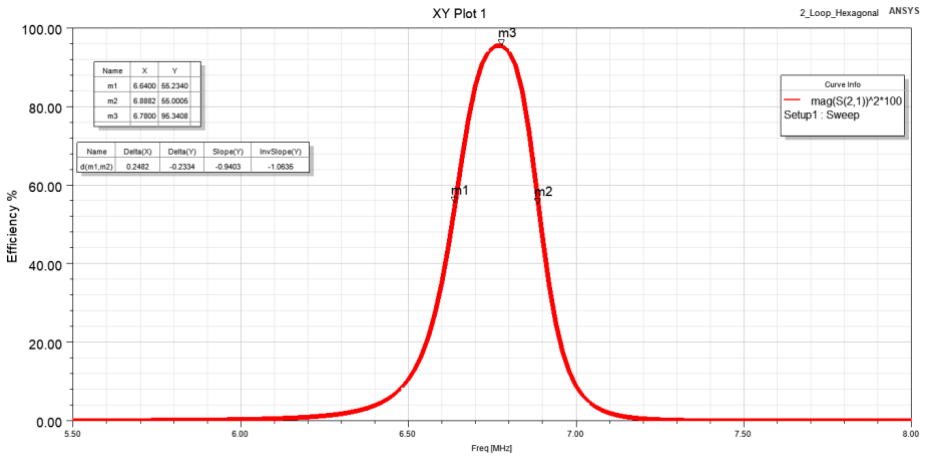

Figure 4.10. frequency drop compensation by adding magnetize strips in 10cm coupling distant

Because the approach discussed in this section does not need accurate lithographic patterning. It is simple to implement and may be utilized efficiently in resonators to deliver the energy to the power conversion chain in our proposed EEG caps electronics.

4.3.3 An Analysis of the Alignment and Misalignment of the Proposed Wireless Powering link Positioned on an EEG cap

4.3.4.1 Lateral and Angular Misalignment

Keeping the EEG cap received power stable across a wide range of coupling and loading fluctuations is a crucial design measure. So, the coupling coefficient, k, between the transmitter (Tx) and receiver (Rx) resonators is essential in determining the amount of power provided to battery-free and cable-free EEG recording setup. Fluctuation in coupling coefficient k can significantly impact the amount of electricity received in the Rx resonator. Misalignments and distance discrepancies between the resonators due to their relative movements are the common causes of coupling coefficient k. Changes in the received power might cause large voltage fluctuations across the Rx resonator. Such differences are particularly undesirable in our design since little power fluctuations might cause malfunction. At the same time, too much power can create heat dissipation within the electrodes, causing them to malfunction or even damage the subject's skin.

As seen in Figure 4.10, the power transfer efficiency is 96.34% under the perfect alignment situation. However, considering Figure 3.26, two significant displacement events, or a combination of them, change the coupling coefficient, resulting in a reduction in power transfer efficiency. However, these adverse effects of misalignment should be compensated in some way. The first misalignment might happen when the subject head is deviating by an angle α according to the x-axis, so, in consequence, the Rx resonators mounted on the EEG cap get misaligned with the Tx resonators which are embedded into the pillow.

Under this situation of angular misalignment, the efficiency drops. In the case of lateral or diagonal displacement, the Rx resonator is moved by an offset distance d concerning the Tx resonator's axis. Still, as long as the subject's head is on powering pillow, the lateral misalignment doesn't significantly impact PTE. Both angular and lateral misalignment may occur in the third scenario. The Tx and Rx resonators are shown in Figure 3.26 with perfect alignment, angular misalignment, lateral misalignment, and both angular and lateral misalignment situations. The magnetic field intensity that generates the current on the Rx in the case of angular misalignment can be calculated through a formula that has been proposed in [258]. The magnetic field is proportional to the resonators' centers lateral displacement relative to the horizon axis in lateral misalignment. The efficiency of the link diminishes as the displacement increases.

Considering the clinical application, since the subject spent 80% of their testing time sleeping on the Tx powering pillow [269], lateral misalignment is not the primary source of power efficiency losses utilizing our proposed EEG cap. However, due to patients' predisposition to move their heads to the right or left side, angular misalignment poses a major challenge for our design. As a result, we'll need to develop a new Tx and Rx resonator arrangement to solve this problem. The simulated power transfer efficiency for several different misalignment conditions, normalized to optimum alignment, is shown in Figures 3.27 and 3.28.

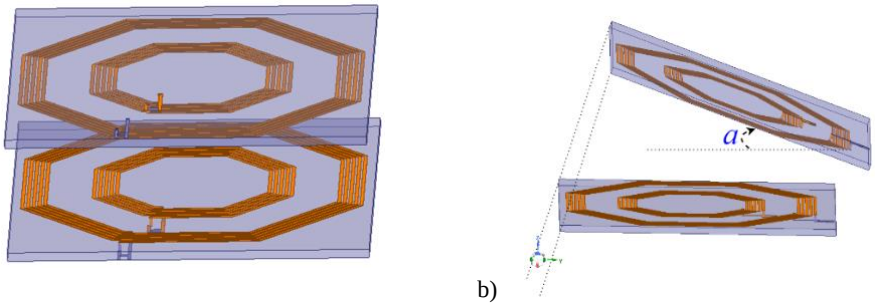

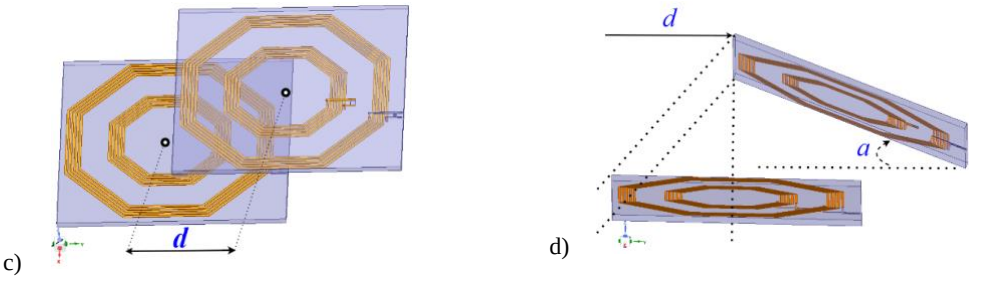

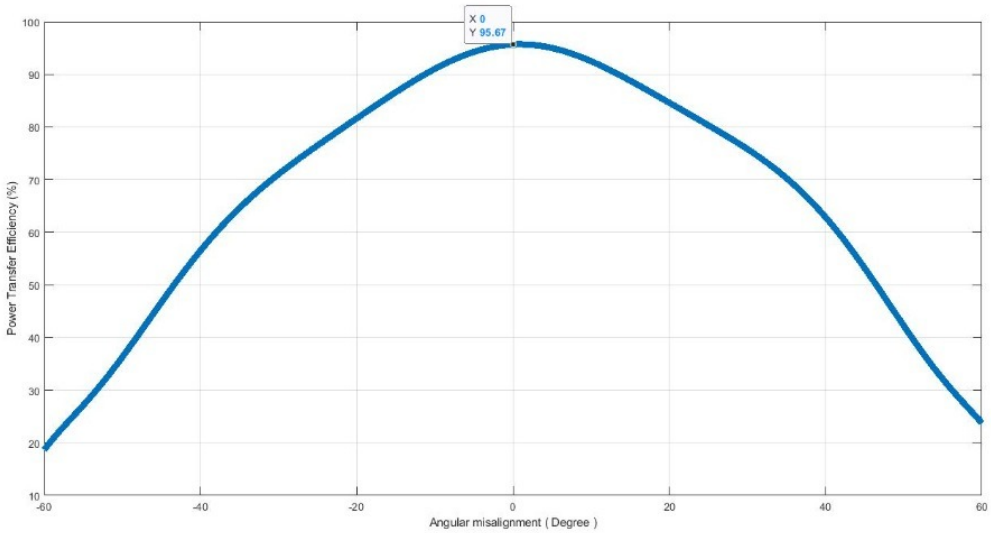

Figure 4.11. a. perfect alignment, b.angular misalignment, c. lateral misalignment, and d. both angular and lateral misalignment

Figure 4.12. Simulated angular Misalignment Versus Link's power transfer Efficiency

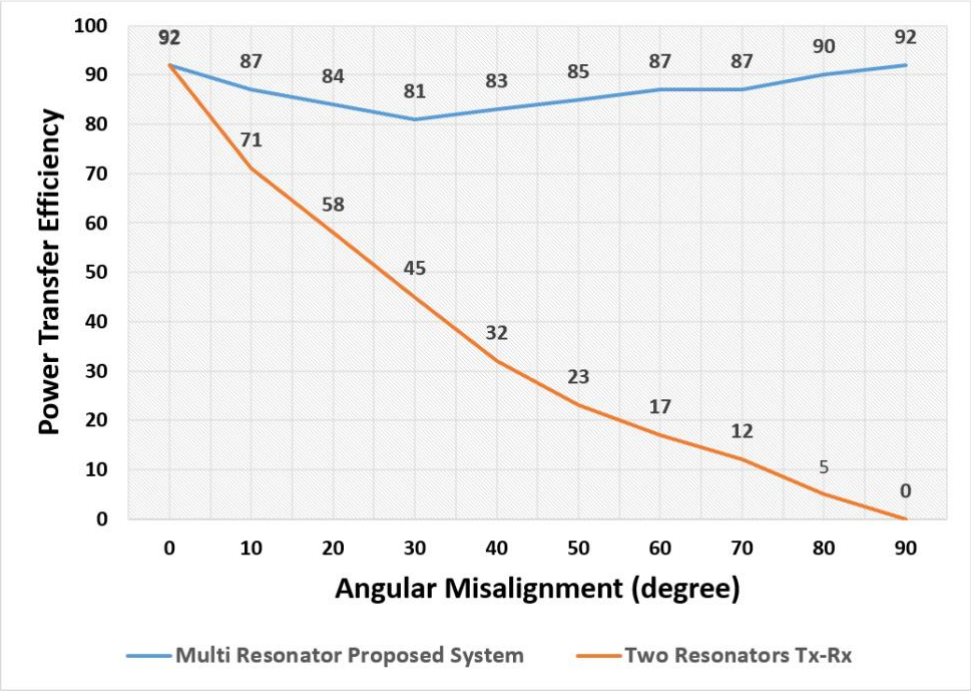

Figure 4.13. Two and multi-resonator configuration angular misalignment versus power transfer efficiency

4.4 Wirelessly Powered EEG Readout Systems via Intelligent Powering Setup

A single resonator can be used beneath the powering test pillow as a preliminary solution, but in actual circumstances, even the smallest powering pillow size is more extensive than a single Rx resonator. In addition, because the sizeable powering resonator has a low self-resonant frequency, putting a single resonator beneath the pillow that covers the whole baseline alters the operating frequency and diminishes the resonant-inductive coupling's PTE, rendering the link incompatible with the back-end powering electronics.

The usual size of the typical pillow, the size and number of resonators, and other potential positioning sensors are all taken into account to design a lattice frame as powering Tx resonator array holders (Figure 4.14). The operating frequency shift is compensated by substituting a sizeable octagonal resonator with multiple small resonators. The frequency compensation allows for a higher operation frequency and relatively large bandwidth for transferring powering data and a stronger magnetic field. The magnetic field in the resonators is focused on the core. As shown in

Figure 4.14, better homogeneous spatial distribution is achieved by expanding the number of resonators, eliminating position-dependent power transmission efficiency. However, as the number of resonators grows, the system may require more power. An intelligent feeding system is designed and manufactured to feed the linked resonators on both sides. In addition, a feedback system to regulate the power level of the Tx resonators is considered for the feeding system to address the difficulty of delivering a high level of power for every single Tx resonator.

4.4.1 Intelligent Positioning System Frame

To completely comprehend the system's operation, keep in mind that the required energy is sent from an external source to the electronics mounted on an EEG cap system via a powering link, including a highly efficient external transmitter and an external receiver. The received powering waves are rectified before being regulated to power up the EEG reading system. In such procedures, the distance or alignment between the transmitter and receiver resonators changes due to transmitter or receiver displacement in angular or lateral misalignment. Any perturbations make variations in the induced voltage on the receiving resonators even though we addressed the misalignment problem by implementing a network of Tx-Rx power links that are fed by an advanced feeding system.

We require intelligent powering to complete the intelligent positioning and feeding system, which may be achieved using digital circuits that contain a microcontroller, ADC, DAC, and multiple MOSFETs functioning as appropriate route switches. The power link operation frequency influences the bandwidth and, consequently, the highest data rate. In addition, the Rx resonator's induced voltage is proportionate to the operating frequency. Furthermore, the highest resonant-magnetic field is created near the resonator's core. Considering the design procedure notes mentioned earlier, the received power reduces considerably when the Rx resonators displace from the center to the corners of the powering resonator Tx. The front-end unit may turn off as a result of insufficient power transmission. To ensure the functionality of the front-end unit in any

circumstance, at least the minimum level of needed energy must be delivered to the Rx resonator. So, the Tx resonator must operate at maximum capacity to ensure the setup function flawlessly. This may be accomplished by constructing an array on either side of the powering link with several resonators, which looks more successful.

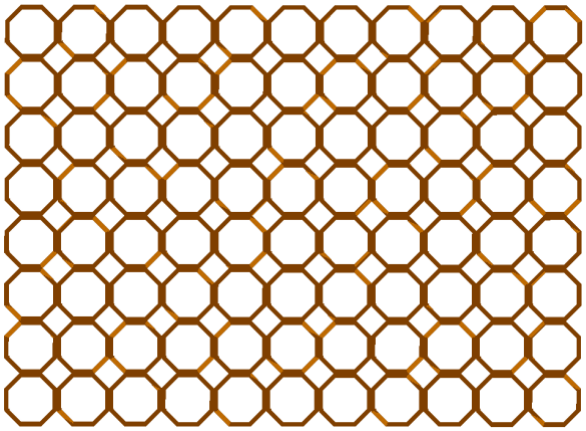

Figure 4.14. a lattice design framework for Tx array

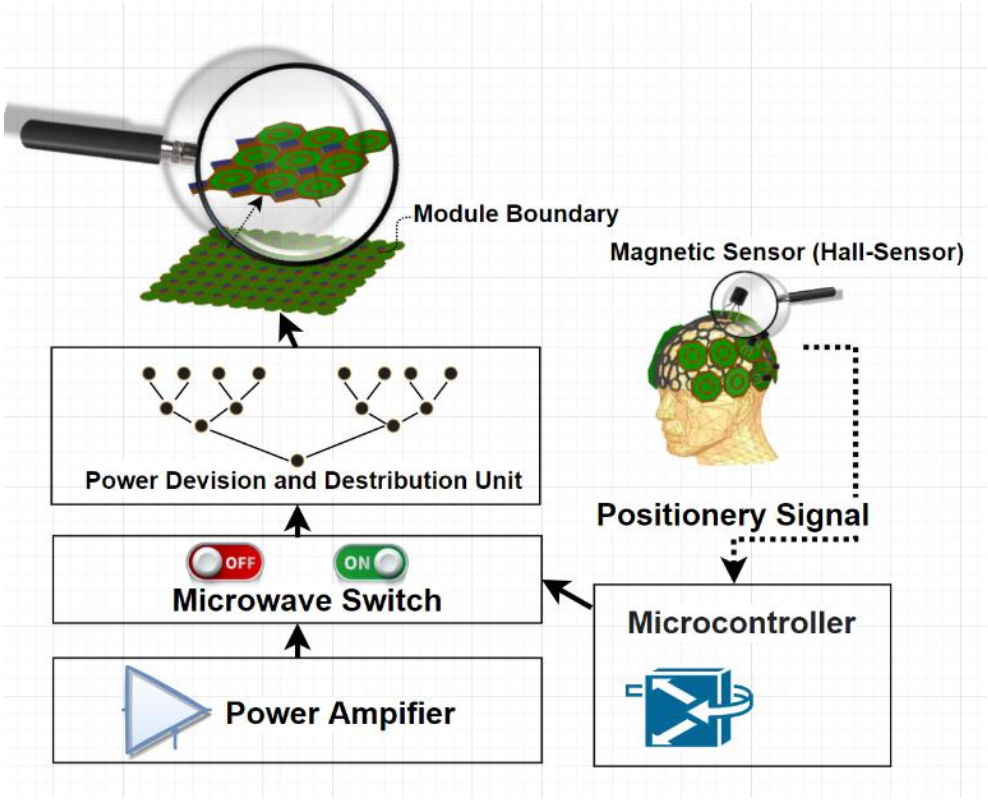

Figure 4.15. Intelligent positioning and feeding system

Figure 4.15. shows a lattice design framework for the Tx array, and Figure 4.15 depicts an array of resonators regulated by a feedback system and supplied by an integrated PCB feeding mechanism. The total energy usage of the system is reduced by using the feedback loop, which involves the most appropriate resonator among the other resonators based on the position of the head.

Using this system, only four of the resonators in the array would be powered up at any powering cycle, and the remainder of the resonators would be turned off. In contrast, the head turns and deviates from the normal position. In proposed remote monitoring that aims at head position, the tested person can freely rotate his head to the left or right. From the clinical perspective, the measurement may not be exact due to the rotational restriction, which may cause discomfort to the patient. The patient can turn his head to any side on the powered cushion during the experiment. As a result, the subject's head must be monitored, and appropriate power can be provided. The suggested feedback system for remotely powered issues is shown in Figure 4.18, with the subject's head freely rotating to either side. A Hall effect sensor (also known as a Hall sensor) uses the Hall effect to detect the presence and amplitude of a magnetic field. A Hall sensor's output voltage is proportional to the field strength. When a Hall effect sensor is near a permanent magnet, it transmits a voltage signal, which activates a set of Tx resonators embedded in the powering cushion.

4.4.2 Positioning System Algorithm

Because the system is supposed to be completely untethered and the amount of power wirelessly transferred to the front-end device is limited owing to safety considerations, we must be careful about the positioning sensor we use in the EEG cap. So, as the alternative idea, we can place active elements (hall effect sensor) on the powering side and passive components (permanent magnet) on the front end (Figure3.32). The hall effect sensor (also known as a Hall sensor) detects the presence and amplitude of a magnetic field using the Hall effect. The output voltage of a Hall

sensor is proportional to the field strength. These sensors determine the subject's head position on the powering pillow (powering back end).

To understand how the proposed positioning system works, assume that the subject's head rotates from point A to point B by alpha degrees on the pillow while it moves on the Y-axis by d cm. This is an example of angular and lateral misalignment occurring simultaneously.

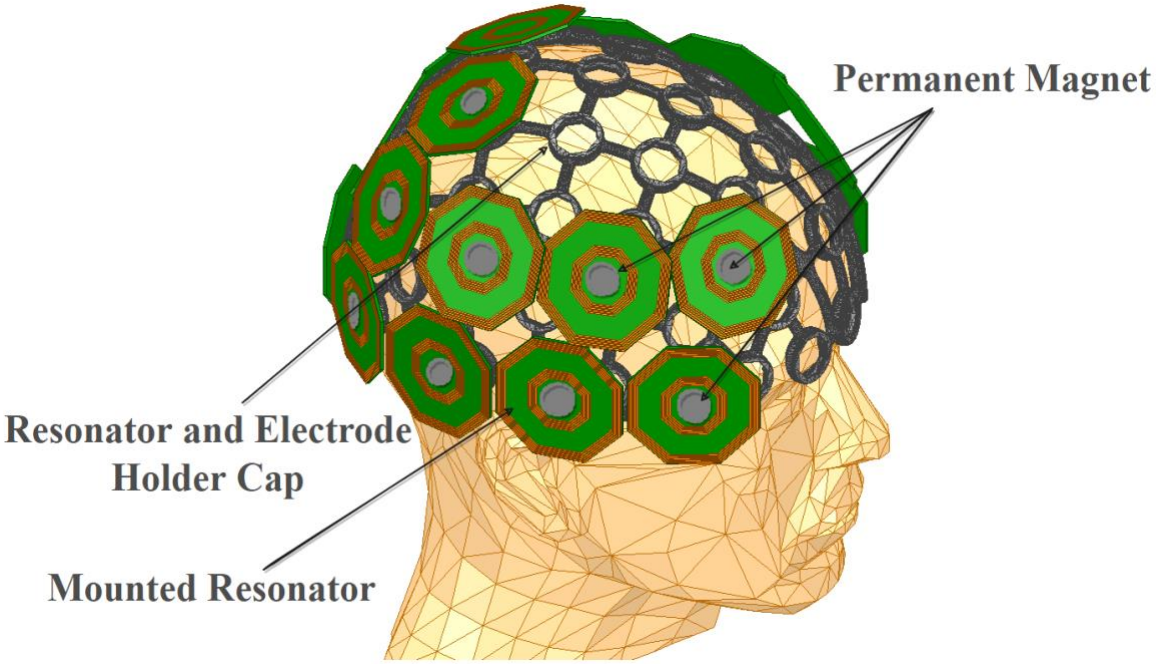

Figure 4.16. the designated permanent magnet positioned in the center of the Rx resonator

Considering Figure 4.17, while the head is in its typical position in A, the output voltage of the S_{34} sensor is first the highest, followed by S_{33}, S_{35}, S_{24}, S_{25}, S_{26}, S_{43}, S_{44}, S_{45}, and finally S_{33}, S_{35}, S_{24}, S_{25}, S_{26}, S_{43}, S_{44}, S_{45}, while the remainder of the sensor is virtually off. The output of the S_{34} sensor decreases as the head travels from point A to position B, whereas the responses of the S_{37}, S_{38}, S_{39}, S_{47}, S_{48}, S_{49}, S_{57}, S_{58}, and S_{59} sensors increase. Therefore, the required switches are flipped on, and the supply voltage from PA is routed to resonators R_{48}, R_{49}, R_{58}, and R_{59} through the almost lossless power divider network. At point B, the output of S_{47} reaches its maximum. A microprocessor generates the control signal to turn on the required MOSFET switches to deliver

enough power to the involved resonators, and voltage comparator circuits compare hall effect sensors' voltage levels and alert us which of the two has the more significant response. The power delivered to load PDL is a superposition of the four resonators surrounded by the nine hall effect sensors grid. The best chance of having the highest voltage responses to permanent magnets positioned in the middle of EEG cap resonators. The voltage level of the Hall effect sensors and the location of the subject's head on the powering cushion decide which four resonators must be powered at any given time.

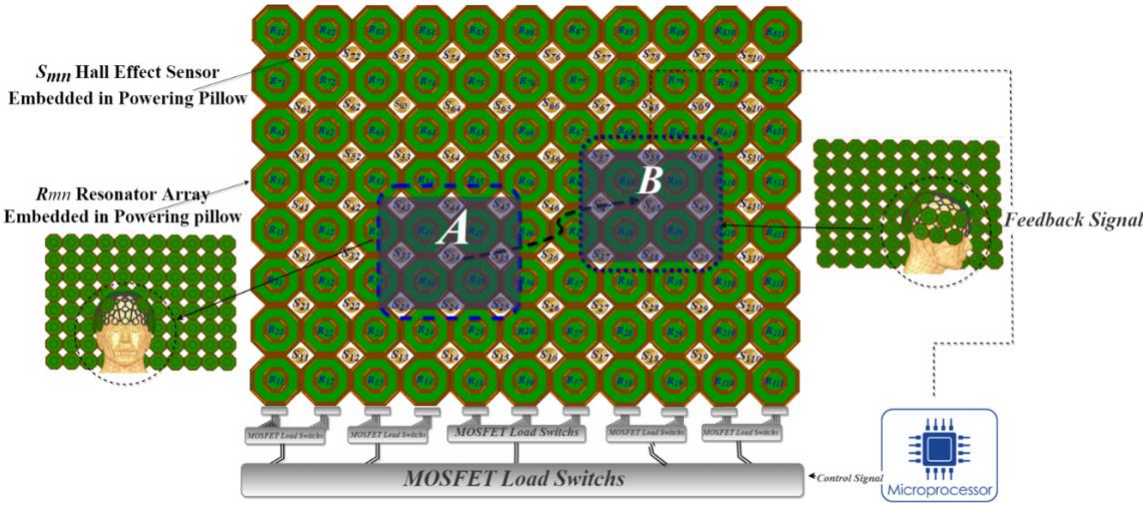

Figure 4.17. The feedback system for remotely powered untethered EEG cap

Since the power transmission efficiency of the resonant-inductive link is strongly dependent on the magnetic flux density (H), which varies with lateral and angular misalignments, the position of the Rx resonators should also be defined according to the center of the Tx powering resonators to supply adequate energy. However, many clinical studies reveal that the individual under the test lays his head on a pillow most of the time vertical (the Tx-Rx are aligned well) [269]. Consequently, the most common cause of excessive misalignment is angular and, on rare occasions, lateral, which both are being investigated in this dissertation. Figure 4.19 shows the power transmission efficiency of the resonant-inductive power transmission (Figure 4.13) as a function of angular and lateral misalignment, as calculated using the 3-D electromagnetic simulator (HFSS).

When the subject's head rotates to either side or moves from the center to the margins of the powering resonator grid, the power provided must be increased to activate the front-end unit. The output of Hall effect sensors may also be utilized to define the location of the engaged Tx resonator concerning the center of the relevant Tx powering resonator. As a result, the front-end system gets enough power it needs by switching techniques that our proposed intelligent feeding systems provide from the primary supply voltage of the power amplifier.

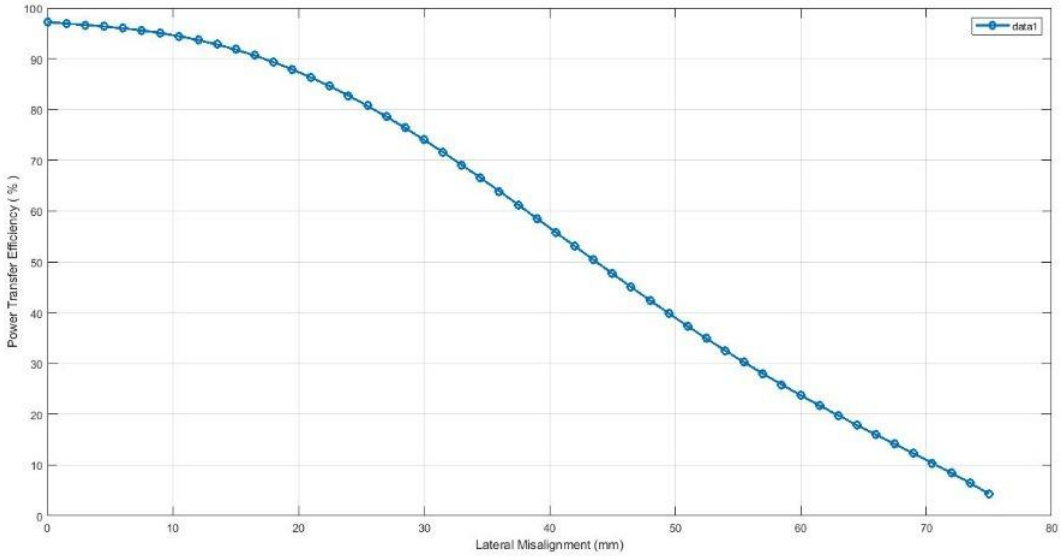

Figure 4.18. The power transmission efficiency of the resonant-inductive power transmission lateral misalignment

The output voltage of each Hall effect sensor monitors the distance between the permanent magnet and the accompanying detector to regulate the power level and turn on a set of resonators. A microcontroller receives the Hall effect detectors' output voltages and translates them to digital signals. Each voltage level has a linear and angular distance kept in a Lookup Table (LUT). The front-end resonators' coordinates are then calculated using the spaces determined earlier. The amplifier triggers the suitable Tx powering resonators by switching and selecting the most appropriate routs based on the location of the front-end Rx resonators in the WPT scenario. To

transfer adequate power to the front-end unit, the area of the Rx resonators is also determined according to the center of the selected resonators where the permanent magnet is positioned; the required power is calculated using the curve of power transmission efficiency shown in Figure 33.3.

Calculating efficiency using a microcontroller is difficult due to the various complex mathematical equations that must be solved. Each power level has its feeding line and several in route switches that connect them to the power amplifier, which is saved in the controller unit's LUT. Finally, the desired route's supply voltage is digitally conveyed to the external DAC, allowing the appropriate power to be transmitted. The abovementioned calculations can also collect data about the subject's head position and resonator state. As a result, the same microcontroller is used to track and show the rotation and movement of the subject's head to provide the adequate required power to the front end considering which resonators are engaged on either side. Linear output magnetic field sensors AD22151, with configurable offset for unipolar or bipolar performance and minimal offset drift over a wide temperature range, are used in the feedback mechanism. As illustrated in Figure 33.3, the designated permanent magnet has a diameter of 10mm and is positioned in the center of the Rx resonator fixed on the head cap. The magnet is 6 cm above the surface of the sensors. Figure 5.8 depicts the Hall effect sensor's response for the north and south poles of a specified magnet in the situation of lateral misalignment. The output voltage is symmetrical for both poles, and the control unit is set up to handle both scenarios. However, the distance between the sensor is another challenging issue since the Hall effect sensor's output saturates at 3 cm from its edges. Consequently, enough Hall effect sensors have been added to the lattice structure to fill the pillow and accurately detect the subject's head position.

The sensors are positioned as shown in Figure 4.16 and Figure 4.17. The Hall effect sensors' output voltages are transformed to 10-bit digital, and the DAC interacts with the controller unit via the evaluation board's serial port. The DAC requires 11 bits to tune the power amplifier's supply voltage. The first three bits are used to choose the right channel, while the remaining eight

bits transform the voltage value. DAC output changes from 0 to 3V with a 10mV step size to manage the power amplifier supply. Because of its outstanding efficiency, the power amplifier (PA) is a Class-E type, and the link's operation frequency is 6.78 MHz.

4.4.3 Design and Analysis of Testbed

Different resonators are created based on geometrical limitations while considering the desired EEG cap design. The optimization strategies stated so far should be employed to explore the EEG cap's best wireless power transfer link. Because of the desired use, certain factors are considered, such as the coupling distance (d_{12}) between the resonators and the outer diameter of the Rx resonator, which defines the resonator's size. Many aspects of our design, such as the capacitor's standard values and the total size of resonators, have a restricted degree of freedom, so we can't do too much with them. They must be correctly packed to achieve the desired outcomes while developing wireless power transfer links. The design parameters of the link, which are specified by the target application, are shown in Table 3.3.

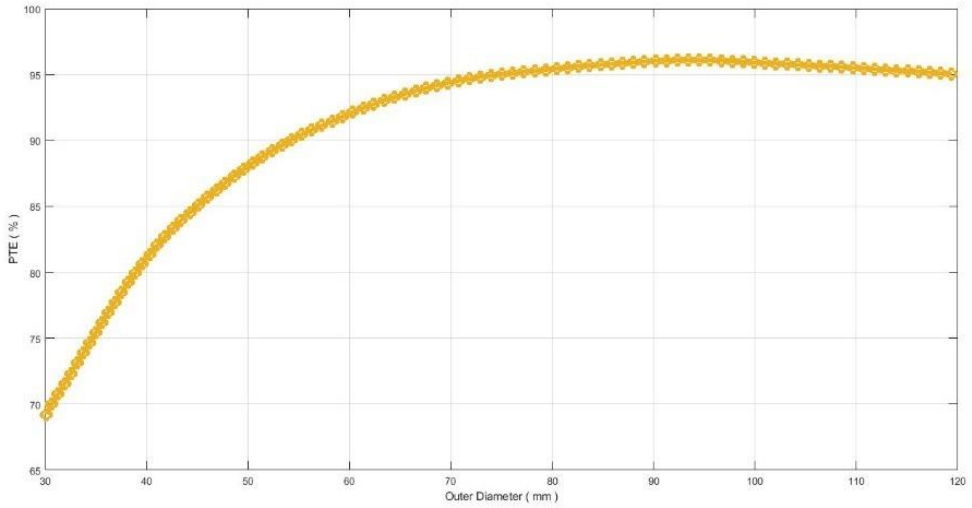

Figure 4.19. The effect of the outermost diameter of resonators on power transfer efficiency

Table 3.3 The design parameters of the link

Parameter	Value
Operation Frequency	6.78 Mhz
Coupling Distance	60-80 mm
Outermost diameter of the resonator	61mm
Minimum spacing between tracks	150µm
Minimum width of tracks	150µm
Load Resistance	1600Ω

The ideal outermost diameter may is calculated as 6.1cm by positioning the Tx resonator under the pillow to reduce the spacing. The perfect diameter for power efficiency is calculated analytically, the same as Rx. Extending the total size of the Tx resonator to encompass every single spot of powering pillow's bottom may seem a solution for receiving power from any corner of the powering pillow. At the same time, the subject's head rotates or moves to either side. But, owing to the restricted self-resonant frequency of the excessive size of the Tx resonator, it may not be the best option because overextending Tx resonator aspects might reduce link efficiency severely. The powering pillow configuration is shown in Figure 3.35. (a) But there must be enough resonators to encompass the entire bottom of the powering pillow. Figure 3.35 (b) depicts the optimized Rx resonators considered for the proposed EEG cap and the resonator network that occupies the base of the powering pillow. There are still a few more variables that influence power efficiency. The self-inductance value increases as the number of turns grow for a given conductor width, while the self-resonant frequency drops.

Furthermore, the quality factor rises in direct relation to conductor width. On the other hand, the parasitic capacitances grow, and the self-resonant frequency decreases. The ideal Tx and Rx configuration must be researched based on theory, simulation, and manufacturing to achieve optimal wireless power transmission link efficiency in resonator geometry parameters. According

to the abovementioned optimization technique, the link power efficiency is tied to the coupling coefficient (k) and the resonator quality variables.

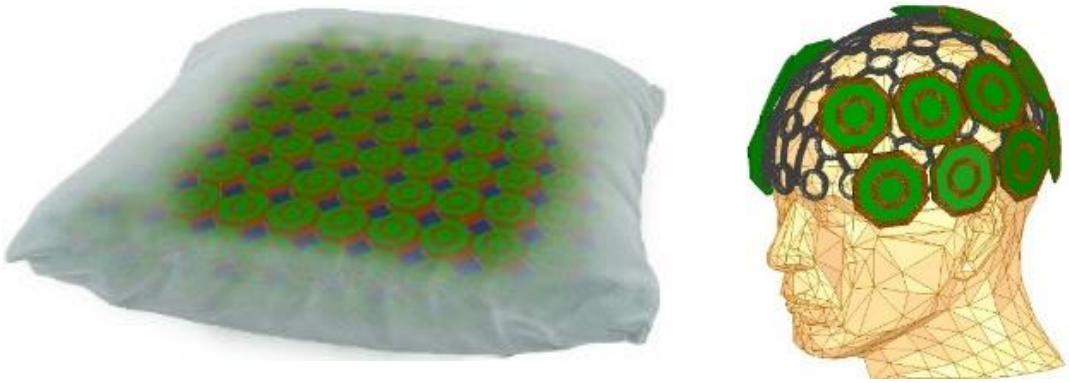

(a) (b)

Figure 4.20. (a) an array of Tx power transmitter resonators embedded in the pillow and (b) a variety of Rx Power receiver resonators placed around the EEG cap

4.5 Electronics and drivers of proposed Wireless power transmission link

Figure 4.21 depicts a powering setup for a wireless and battery-free EEG reading device intended for freely moving targets such as the human head. Any movement and displacement of the head alter the coupling between the powering and the resonators mounted on EEG caps, resulting in a misalignment of the Tx and Rx resonators. Because the load impedance varies as the coupling coefficient changes, a well-designed, highly efficient power amplifier should be developed or chosen to work effectively under various load situations.

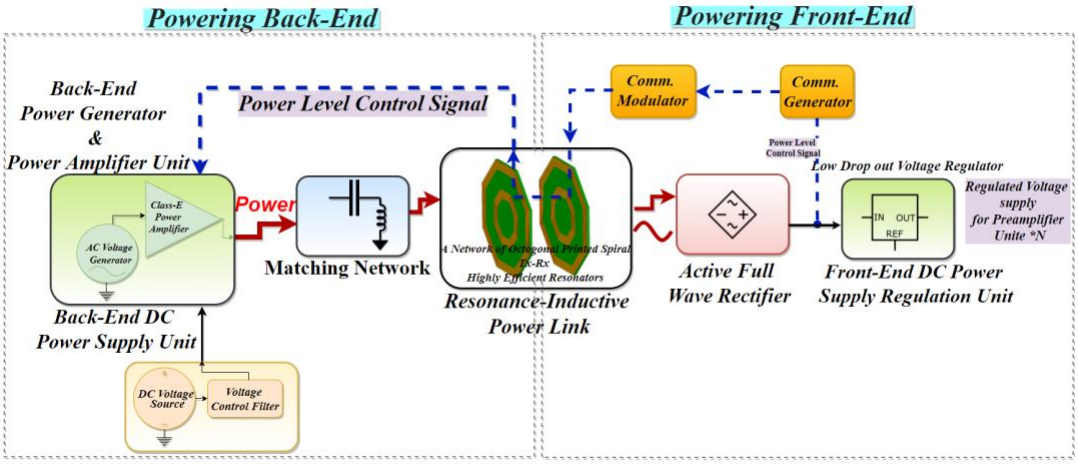

Figure 4.21. The recommended powering set up for wireless and battery-free EEG reading devices

The main goals of this section are to study an appropriate power amplifier working at 6.78 MHz, optimize resonant inductive power transmission for high power transfer efficiency, develop the most efficient power conversion chain for the front end, and integrate the components of the power conversion chain (PCC) on the EEG cap side to fit within the volume allowed for wearable EEG cap.

Delivering appropriate power to the load (PDL) while retaining high power transfer efficiency (PTE) is an essential design requirement in wireless power transmission. Increased power transfer efficiency is necessary to fulfill regulatory standards since it reduces heat dissipation within the resonators and exposure to electromagnetic fields, which can cause further heat dissipation in the power transmission medium. Higher frequency to reduce resonator size occurs at the expense of higher energy loss due to absorption by surrounding tissues. Considering the mentioned issues, the powering link must give enough power to the load while also considering the realistic capabilities of the energy source and power amplifiers. There have been several approaches to creating the most optimum wireless power transfer systems. [261] and [262] changed the Tx and

Rx resonator configurations, L_2 and L_3, to attain the most considerable voltage on the load and high power delivery. When space is restricted, such as the suggested EEG cap, the amount of power given to the load is an important design element, and resonators' size must be reduced. A great deal of research has gone into the design and geometrical optimization of resonators in resonant-inductive coupling for a typical Tx-Rx based on power transmission efficiency. [272] uses a slightly different approach, in which L_3 is optimized first for optimum power transfer efficiency for a given R_L. Then L_2 is adjusted to deliver the appropriate voltage gain from source to load, increasing the amount of power transferred. Unfortunately, there is no detailed research in the literature for a specific target application that can incorporate both power transfer efficiency and control delivered to load to assist designers in emphasizing crucial but seemingly competing criteria. Based on application needs, well-designed research can provide designers with valuable insight into improving resonant-inductive power transmission networks. First, it guides designers toward resonant-inductive power transmission lines with the highest possible power transfer efficiency and power delivered to load. Second, it assists the designer in determining the number of loops on each side resonator required for a given application. On the other hand, energy management is critical for the proposed wireless EEG recording systems' safe and uninterrupted operation due to human health concerns.

Considering the following equation, which is the total PCTE of the link:

$$\eta_{total} = \eta_{PA} \times \eta_{coupling} \times \eta_{rectifier} \times \eta_{regulator}$$

As a result, the selection and optimal design of the electronics that drive the powering link are critical for effective wireless power transmission.

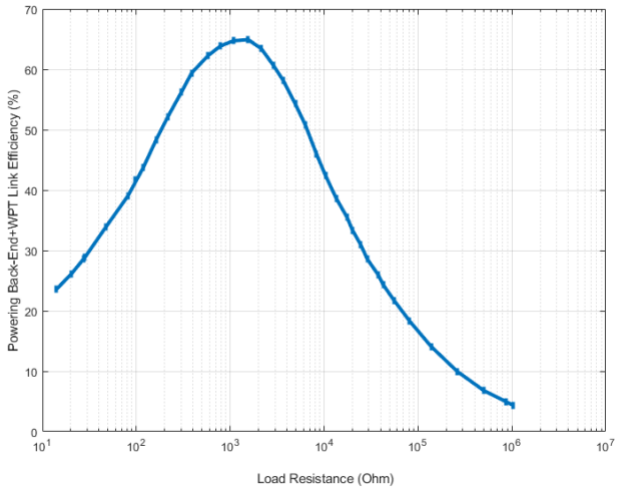

Figure 4.22. Simulation result of power transfer efficiency of powering back-end and WPT link

4.6 Power Amplifier

The circuit model wireless power transmission link set up for the proposed EEG cap is shown in Figure 4.23. An effective amplifier must drive the powering Tx resonator array. The energy is transmitted from an E-class power amplifier in the powering back end over a uniquely engineered, efficient wireless powering link scheme. The power received on the Rx side is then rectified and regulated to turn on the power-hungry circuitries on the front-end side. As seen in Figure 4.23, the inductance, parasitic resistance, parasitic capacitance, and the resonant capacitance for adjusting the inductance to the operation frequency, the distance between the resonators, and the coupling coefficient between the resonators are shown with the circuit model of TX- Rx link.

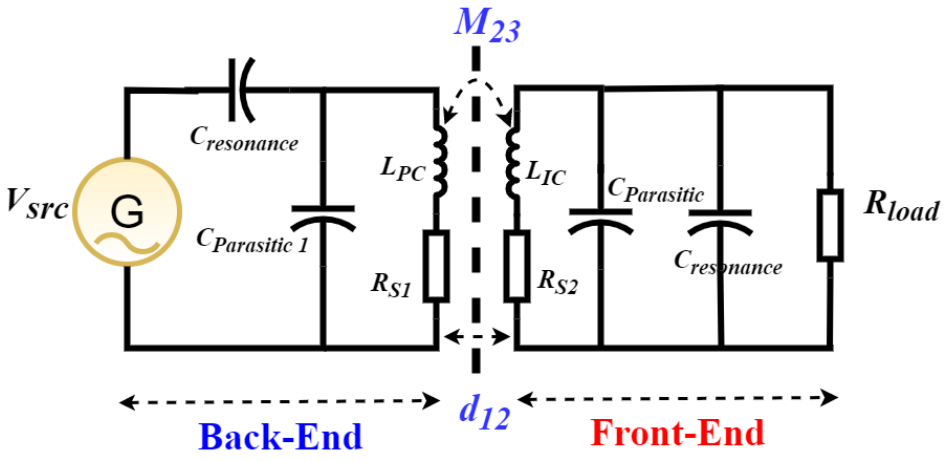

Figure 4.23 Circuit model of Tx-Rx powering link

The resonators and a power amplifier run at a resonance carrier frequency to power up the active power conversion chain's units. This resonance causes the WPT and runs the front-end electronics mounted on the EEG cap. When utilizing this transmitted power at the receiver, a rectifier, regulator, and bandgap voltage reference must provide a stable, load-independent voltage to the circuit. These power management devices must be low-power, low-cost, and produce as little as 1/f noise for the system. As seen in Figure 4.24, the clock generator provides a 6.78 MHz clock signal in the back end, which is amplified by the power amplifier (PA). The primary and secondary resonators' LC values must be designed to achieve LC resonant at 6.68 MHz.

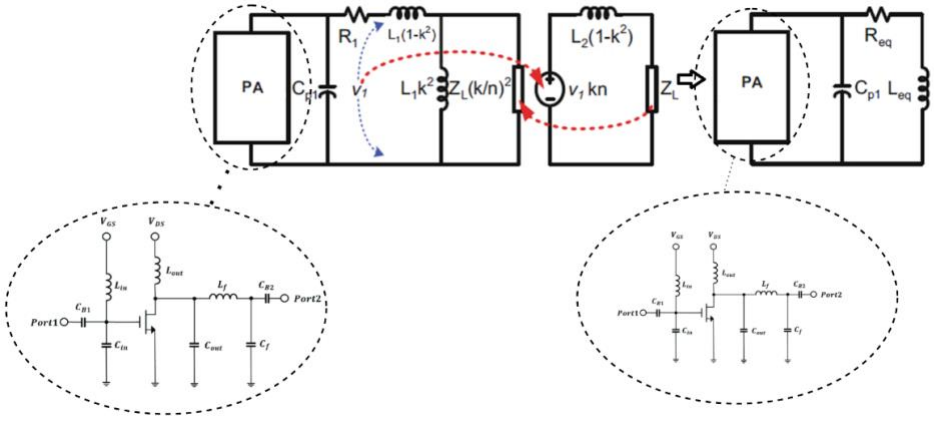

Figure 4.24. resonant inductive link and E-class external link driver

One or more primary Tx resonators receive power from the amplifier through an intelligent feeding system and begin radiating depending on the engaged Rx side resonators mounted on the head cap. In the front end, an identical situation exists, and one or more resonators get employed in a power transmission scenario. As the subject's head moves or rotates in the given space, the misalignment between the resonators changes the coupling coefficient.

4.6.1 Coupling Coefficient Impact on Wireless Power Transmission -

Considering Figure 4.21, because every single component's efficiency counts in the overall design, the transmitter resonator Tx should be powered by a high-efficiency amplifier PA.

A link driver, a data receiver, a power controller, and a Tx powering resonator make up the back-end's powering unit. The drain performance of a Class-E amplifier is exceptionally high, and the efficiency of such a power amplifier is potentially up to 100 percent [273]. Furthermore, the Class-E amplifier is well suited for wearable application link drivers [274]. The Class-E amplifier is straightforward to implement compared to the other conventional power amplifiers. The gate driver, which controls the entire amplifier's performance at a higher frequency, is significant in optimizing energy consumption and lowering power loss. The gate driver in a Class-E amplifier is a simplified oscillator circuit, which decreases design intricacy and energy usage compared to other power amplifiers that we can use for our setup: a desired class-E power amplifier and the wireless power transmission and conversion chain as shown in Figure 4.24. The C_{res1} and C_{res2} capacitors fine-tune the resonators' operating frequency.

Furthermore, R_{load} denotes the load of the WPT link, which is the front end's rectifier's input resistance. Because the subject's head moves or rotates during the test, the EEG cap is unavoidably shifted out of its ideal alignment, causing the coupling between the Tx and Rx resonators to vary. The power amplifier must have a high-power efficiency in various coupling

conditions. Figure 4.25 depicts the simulated power efficiency vs. coupling coefficient results for a Class-E power amplifier optimized with k =0.04.

The power efficiency for k =0.08 is 96.82 percent and constant for a broad coupling situation. The overall energy transfer efficiency remains high even when the subject's head is moved away from the most efficient position.

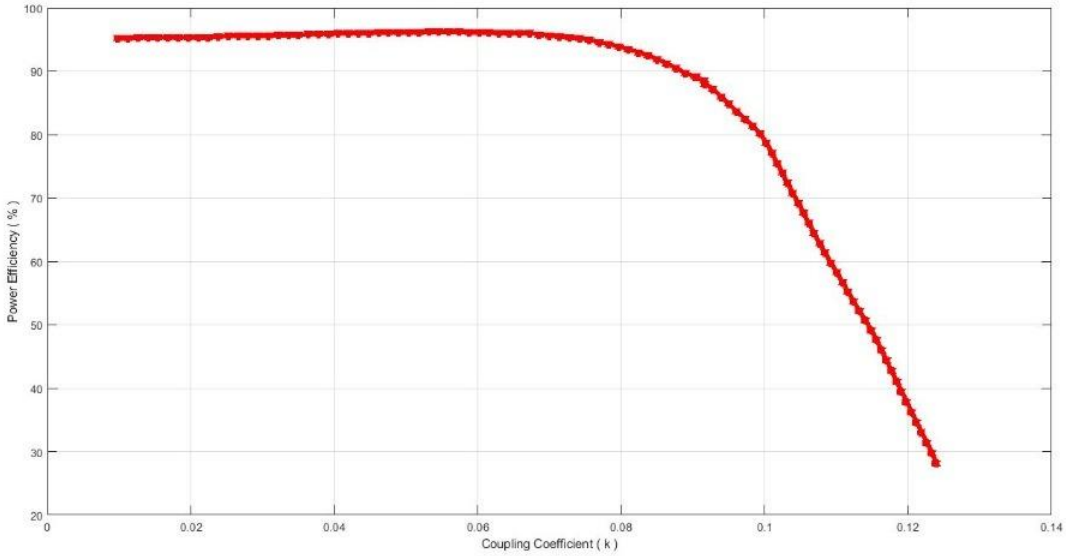

Figure 4.25. the simulated power efficiency vs. coupling coefficient results for a Class-E power amplifier optimized with k =0.01

Because the power amplifier is tuned for a specific load impedance, its power efficiency drops as the load impedance increases. The power amplifier is selected and engineered to perform well under various load circumstances. Furthermore, given the difficulty encountered throughout implementation, choosing the best power amplifier is critical in the initial design steps. The amplifier design should reduce the power amplifier and the overall setup's complicity.

4.6.2 Powering Front-end and Back-end Circuits and Electronics

WPT can be compared to a transformer to envision the wireless power transmission network. Considering Figure 4.21, The main resonator Tx receives power from PA and generates

an electromagnetic (EM) field, and the second resonator is being exposed to this field. At the intended carrier frequency (fc=6.78MHz), a power amplifier (PA) powers the Tx resonator, L_1. The rectifier rectifies the AC signal over the secondary resonator L_2C_2-tank, tuned at f_c. The rectifier output is then sent into a low drop-out voltage regulator. In the WPT link, the coupling efficiency is related to the power transfer efficiency. Wirelessly transmitting the front-end's power information to the back-end and driver side is also possible through the same resonant inductive powering link.

Regarding the budget link, the EEG cap platform requires a maximum of 1.25 watts of power, which it obtains via wireless power transfer. The power chain conversion unit requires a resonator transmitter and a suitable receiver module to create a power transfer link. Due to safety issues, they must all resonate at a frequency below 20 MHz to build a safe, complete wireless power transmission system. Our system's technical specifications require a maximum output of 5V/250mA to run the entire setup.

The long-term and uninterrupted operation of the EEG read-out system highlights the practical design of the resonant inductive link and power-management circuits in the power link. When employing resonant-inductive coupling with a limited amount of received power, the problem of low-power data transmission must be considered, such as undesirable interference with the powering link frequency. As a result, low-power consumption power management and data transceiver units must be established as critical elements of the power conversion chain.

A key element of our design is the utilization of high-efficiency power conversion chain circuits. The power management unit's controller IC manages the system and executes the power transfer protocols, while the resonator drive IC provides the required power level to the transmitter resonator. The back-end circuitries and the front-end electronics can handle systems with up to 5 watts of power. However, our proposed EEG cap system would only have about 1.25 watts of power. In the proposed setup, the supporting components, on the other hand, maybe changed to fit

our goals. The performance of the power management unit must be evaluated since it allows us to see how the power receiver and Tx transmitter resonator constantly regulate the wireless power process to supply and transmit the required energy for our setup. As shown in Figure 4.21, the power transmitter electronics are made up of six subsystems that, when correctly coupled, can execute the transmitter's full function in our power management unit. The V volt filter block smooths the input power supply. Then the smoothened voltage as a constant power supply goes to the controller unit, a wireless power controller that monitors all transmitter activities. Then, the Tx resonator driver, a transmitter driver, drives the Tx resonator using controller inputs. The Tx resonator comprises a series of octagonal shape resonators in spiral con PCB transmitter (a pair of batch-fabricated printed spiral resonators (PSC) utilizing micromachining technology) that work in tandem with the receiver resonators, which are basically in the same arrangement. A Feedback signal module will also be required to change the resonator and drive settings as a feedback input to the controller. Figure 4.26 shows the powering back-end system-level design.

4.6.3 Powering Front-end Units

The induced AC voltage captured by the group of resonators on the EEG cap must be transformed into a continuous, steady dc voltage to run the EEG recording set up. As a result, an AC-to-DC converter and a voltage regulation block are needed. A power management unit is also required to control the received signal level and alter the transmitted information regarding the front-end power level to the power transmitter side, part of the design's back-end. We may measure the efficiency of power transmission across the system using the suggested plan by comparing the power received by the receiver at the output (not the Rx resonator) to the power received by the transmitter (not what we supply to the Tx system from the power amplifier). The graph shows that the slope flattens as additional channels are added to the system as load (for example, having 256 channels to achieve high spatial resolution). This indicates that if the load on the system increases, we'll need to give 250mA current to power the entire EEG signals recording system, resulting in a

95% efficiency. Because the Tx-Rx resonators in wireless power transfer links lose more power when energy is transmitted from the Tx resonator to the Rx, improving the system in the resonator's units can considerably improve the overall system efficiency.

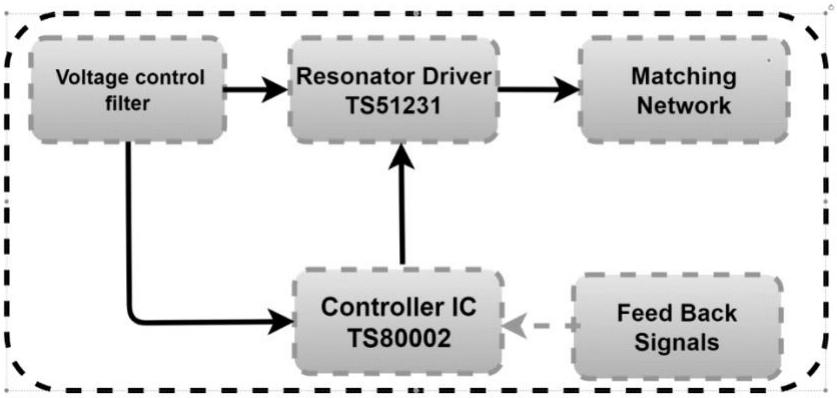

Figure 4.26 Tx resonator driver electronics

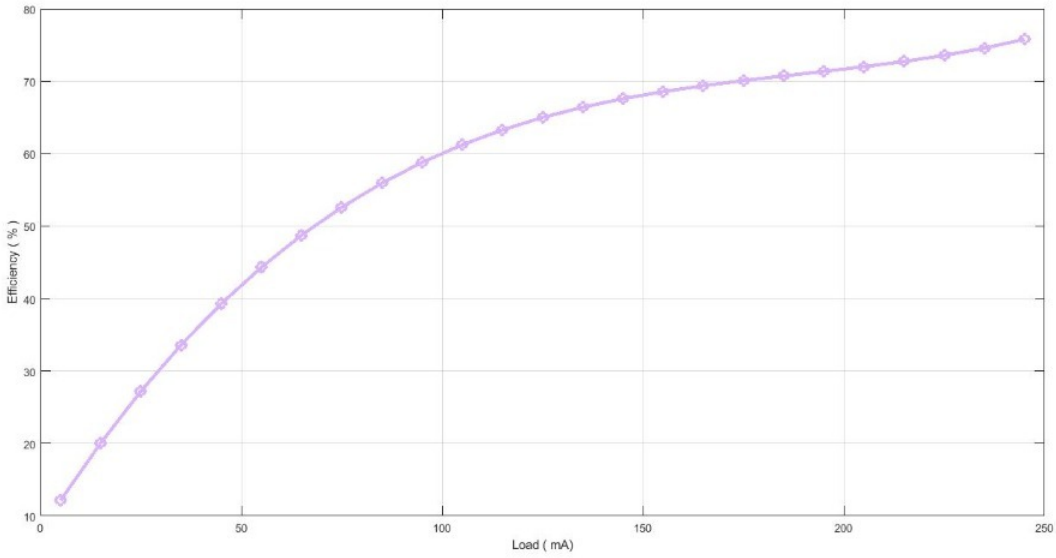

Figure 4.27. Driver Efficiency Vs. load

4.6.4 Powering Algorithms

Three wireless power transfer methods have been developed from the literature's standpoint of the power consumption of front ends. The first category includes our battery-free and cable-free EEG readout device.

1. Wearable devices with a minimal power consumption of up to 3 watts, such as headphones, wristband devices, medical sensors, etc.

2. Devices with medium power consumption, such as mobile phones, tablets, and medical electronics, consume 5 to 15 watts.

3. Power-hungry devices that require a high level of power to run. This category includes devices that require 15 to 100 watts of power, such as power tools, Remote controls devices such as drones' RC, and other equipment. In addition to being intelligently regulated, wireless power systems used in wearable or implantable devices, such as our proposed design, differ from traditional WPT systems in another crucial sense. It is the high efficiency of the entire system. For the safety and maintenance concerns, we considered a few design requirements. First, the Tx resonator through the powering back end unit only supplies power when the right Rx side receiver resonators are activated and linked to the Tx resonator. It only delivers the precise amount of power that the front-end demands.

Second, the system must identify when the electromagnetic field is disrupted by an undesired condition and immediately turn off power transmission to prevent any significant amount of power from being absorbed by anything other than the respective receiver resonators. So, before doing anything, a programmable IC (TS80000) scans for a power receiver to identify the right Rx receiver resonators. This allows us to intelligently regulate our power management unit's wireless power transfer process. When the receiver detects a power demand, it informs the transmitter, and the powering via the wireless system begins. The system then double-checks that the right level of electrical power is being transferred and, more importantly, no energy is being wasted owing to

foreign material. To keep the WPT procedure running, the receiver will make repeated requests for power, and the process will end if the requests stop.

This technique can support even complex powering patterns for devices with a higher level of sensitivity since the transmitter may supply varying quantities of power depending on what the receiver (load) requires. When the receiver no longer requires power, such as when only a few channels must be turned on while the others are turned off, or when the EEG reading process is over, it may notify the transmitter. The transmitter may lower its output correspondingly. When the receiver no longer requires a high level of power, such as when only a few channels must be switched on while the others are turned off, or when the EEG reading process is completed, the transmitter may be notified. The transmitter's output may be reduced accordingly.

4.6.5 Front end Power Management Description

As shown in Figure 4.21, the suggested power management in the front-end unit is composed of many sub-systems. A power management unit must develop a complete wireless power transmission system that can directly power up our suggested EEG recording equipment for roughly 250mA of current. The front-end electronics of the power management unit are connected to a 6.78 MHz transmitter resonator, and the back-end electronics are coupled with a 6.78 MHz receiver resonator. The Tx resonator is a printed spiral resonator (PSC) batch-fabricated using micromachining technology to transmit power from the back-end to the receiver resonator Rx at the front end. Due to a misalignment issue that may drastically reduce power link efficiency, a group of Rx resonators with delicately chosen positions are placed on the back hemisphere of our proposed EEG recording cap. These are the secondary resonators in the flux field of the TX resonator and are part of the 6.78 MHz resonant tank. The rectifier, which transforms the AC voltage received from the RX resonator to positive values, is the first block following the Rx resonators. It is preferable to use FETs in the design of the rectification unit for maximum conversion efficiency. The regulator turns the rectifier output into regulated 1.8,3.8 and 5v outputs

while also providing protective circuitry. This sub-block is crucial since a super smooth DC voltage must power ICs. A few additional subsystems must be addressed in the design to completely regulate the entire powering unit. First, a command generator device informs the backend unit to switch the power. Another command modulator unit delivers the handshake signal to the transmitter using the same power link.

To develop complete wireless and battery-free portable EEG recording system, we'll need a powering unit that can provide about 250mA of electricity to directly power up the electronics, including 64 channels and front and back-end powering circuits. The design and module selection in our power management unit is created in such a way that they maximize the efficiency of the process. For a recommended low-power, wearable wireless, and battery-free EEG readout system that necessitates a low-cost and space-saving solution, an IC, which is a fully-integrated, plays a vital part as the core of the wireless power receiver. The IC can function as a single-chip wireless power receiver in customized applications such as our design. It can also work with a wireless power controller, microcontroller, or microprocessors to handle standard wireless protocols such as Qi, PMA, or A4WP and custom standards operating in higher frequencies up to 2W combined system. When one or more Rx resonators are within the range of power transmission (at least 60 mm), the back-end provides enough power to the transmitter resonator, and communication begins. Suppose the transmitter transfers an inadequate level of power to the front end. The front-end unit can inform the backend via the same power link about its power level requirements, indicating that the total number of channels currently involved in the EEG signal reading procedure has increased. The back end should respond by increasing the level of power. When this exchange is complete, the power amplifier in the back-end unit begins to give the necessary power to the front-end. So, throughout the power transfer process via the same link, the receiver, Rx, interacts with the transmitter Tx and actively controls the wireless power transmission process. This guarantees that power is only given when the front-end requests it. In addition, the quantity of power is determined

by the EEG readout set up and delivered in a way consistent with its needs (considering the number of channels involved with the reading procedure). The front end can actively raise or lower its power request for safety reasons, and the transmitter will respond adequately. Consequently, the most intricate WPT measures may be perfectly satisfied by transmitting only the appropriate amount of power from the back end to the front end through the same power link. It's vital to remember that, unless the application only requires a small amount of power (a few tens of mW or less), a high driving voltage (Vs) will be required in all other circumstances, that it results in limiting driver efficiency and posing safety risks in clinical settings.

The framework of the proposed wireless powering electronics for our suggested EEG cap is shown in Figure 4.22. A low-dropout (LDO) voltage regulator follows the rectifier to provide a smooth and steady supply voltage (1.8, 38, and 5V) for the other super-sensitive ICs designed to amplify, digitize, and code, decode and transmit recorded EEG data. A completely CMOS reference voltage generating circuit provides the reference voltage for the LDO voltage regulator. Two essential subsystems perform Power-On-Reset (PoR) and a power feedback mechanism that makes up the power management unit. Compared to a given voltage level, the PoR circuit checks the power flow in the EEG head cap and activates or shuts down the entire front-end system.

Moreover, the front end's received power is kept constant by regulating the transmitted power level. A closed-loop power feedback system monitors the front-end power level and sends feedback information to the back-end. The provided power level drops to zero if there is excessive power consumption in the front end unit, which indicates a malfunction in one or more subsystems, resulting in extra power dissipation in heat. On the other hand, it may rise to a certain level to compensate for any efficiency drops due to misalignment or other disturbances that cause the system to deviate from its optimal operation.

4.6.6 Technical Specifications of Power Conversion Chain

Because power budget, weight, and size are the most critical design considerations, low-power design optimization methodologies may be used at various design phases, from the algorithmic and system level down to the circuit level. This is due to the significant power required to execute the essential operations while considering biological constraints; thus, we must build the system so that the maximum amount of power can be transmitted via barriers between Tx and Rx. So Low-power design necessitates the use of precise power estimation and optimization techniques. Just right after the Rx resonator, we have power conversion chain units. A diode-connected transistor rectifier, a voltage regulator, and a single or multi-channel active electrode with two electrodes and a reference point for each channel make up the load of the proposed wireless and battery-free EEG reading system. Because the base is primarily made up of digital blocks, it is frequently provided at the technology's nominal supply voltages.

The primary purpose of a power conversion chain for our proposed EEG setup device is to allow power transmission and distribution. A rectifier, regulator, and bandgap voltage reference are required to give a stable, load-independent voltage to the circuits on the front end. These systems are active circuits and need energy sources to perform their intended purposes. As a result, acquiring sufficient energy to power them up remains challenging. Rectifiers are commonly built with diodes or diode-connected MOS transistors. Full-wave bridge structures are more often used than half-wave rectifiers because they have greater power efficiency, fewer output ripples, and a higher reverse breakdown voltage. The proposed EEG recording system requires linear series voltage regulators to create a ripple-free voltage supply. The model includes a pass device, error amplifier (comparator), sampling circuitries, and a reference voltage generator as a rectification unit. The power management units must be low-power, low-cost, and produce as little as 1/f noise.

It's also ideal if the entire powering link’s electronics and circuitries are fully integrated on the CMOS substrate, but it imposes more restrictions.

Another point that must be highlighted as a crucial piece of practical advice is that we apply a passivation layer to shield a wireless power transfer (WPT) resonators' network from the outside environment and substantially enhance the safety measures, in addition to the noticeable size reduction compared to the usual EEG system already in use today. Because resonator design essential factors such as conformal shape and necessity of being relatively small in size (particularly Rx resonator), as well as considering the restrictions related to mediums between the Tx and Rx resonators in the vicinity of other powering channels, it is expected that any perturbation could affect the efficiency entire system and reduce it drastically, so any other stationary electronics must be designed or selected with this point in mind that they must have their ultimate efficiency while preforming in our system. Furthermore, due to low coupling efficiency (when the individual moves or rotates his head to one side or the other), the provided power in these systems varies from hundreds of μW to a few mW. It is crucial to remember that the maximum back-end (base station) power radiation to turn on the EEG readout system is mainly dependent on the efficiency of powering link.

The system's overall volume is dominated by several parameters, such as the secondary resonator Rx's size, and the resonator's size is related to the power carrier's frequency. Even though the resonator size is reduced by increasing the carrier frequency, the power loss increases due to medium and nearby tissue absorption above a few tens of megahertz. In addition, providing compatible electronics is another decisive factor in choosing powering frequency. For a wide range of biological applications, the required power budget is in the mW regime, and the power delivery unit must be optimized for this power range, and this introduces new tradeoffs and circuit design alternatives. We need to consider a low-offset amplifier with a high gain for the amplification unit. During the early phases of a project, a model may be used to analyze the contribution of each circuit

module to total power consumption and forecast the input and output voltages of these modules. Verilog-A can be developed based on a power consumption model with average power usage.

Chapter V Fabrication, Testing, and Experimental Results

5.1. Conformal Resonator's Geometries and Parameters

Resonator shapes and configurations are among the most critical factors that define a link's power transmission efficiency. To comply with most applications, those resonators intended for biomedical applications in the future generation should have been planar, flexible, and lithographically fabricated in one or more layers on rigid or flexible substrates. Spiral shape inductors are one of the most significant components of WPT.

The layout and the structural parameter of the fabricated octagonal spiral resonator are shown in Figure 5.1. depending on the target application's requirements, Tx and Rx resonators are PSCs with non-overlapping octagonal shapes fabricated on 0.8382 mm thickness FR4 sheets with a copper thickness of 18 μm. For Tx-Rx design, the PCB manufacturing technique requires w_{min} and s_{min} to be 150 μm.

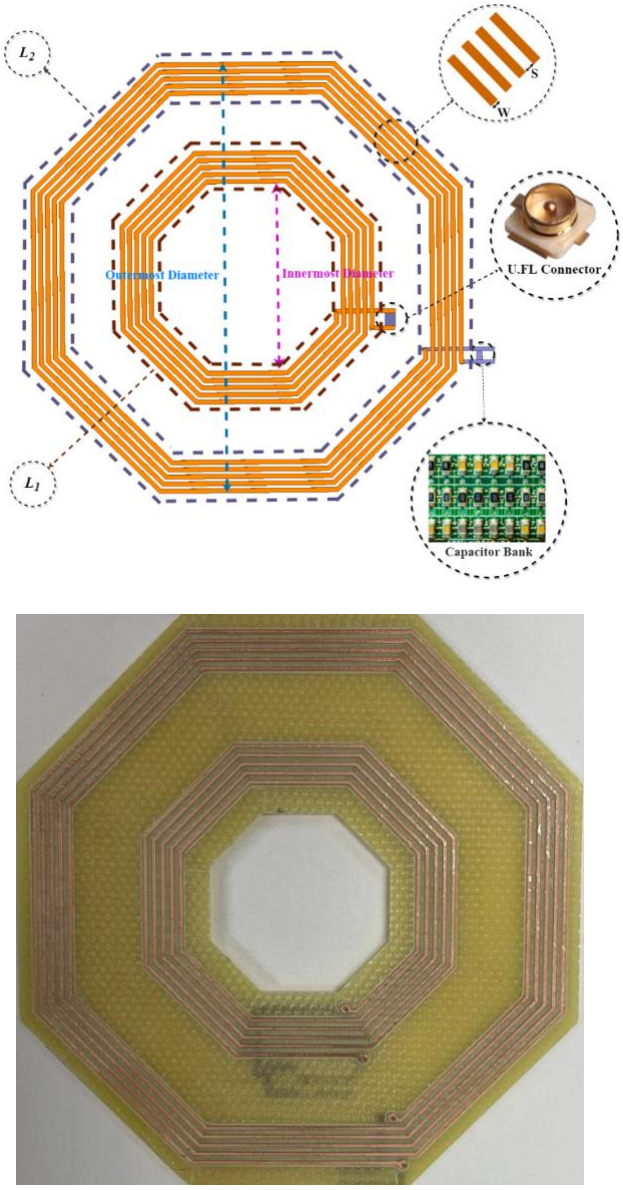

Figure 5.1. The layout, excitation port, and resonance capacitor bank of the proposed octagonal spiral resonator.

Due to the overlapping L_1 and L_2 in the 2-loops configuration on either side, the resonator size affects coupling distance. Because of the size limitations in the EEG cap, electrode holder size, and predetermined scenario defined for powering procedure while the subject's head is rolling on the powering pillow, the outermost and innermost diameters are limited to 6 and 2.6 cm. A few more variables still influence the link's power efficiency: the self-inductance value increases as the number of turns grows for a given conductor width, while the self-resonant frequency drops.

Furthermore, the quality factor rises in direct relation to conductor width. On the other hand, the parasitic capacitances grow, and the self-resonant frequency decreases.

The ideal Tx and Rx configuration must be researched based on theory, simulation, and manufacturing to achieve the most optimum wireless power transmission link efficiency considering the smallest size of the resonator in the desired frequency. The link power efficiency is tied not just to the coupling coefficient k but also the resonator quality variables.

The fabricated optimized powering link is shown in Figure 5.2; the links consist of two loops meandered orthogonal resonator on each side in the front layer, and the resonance capacitor and the matching network are considered in the back layer.

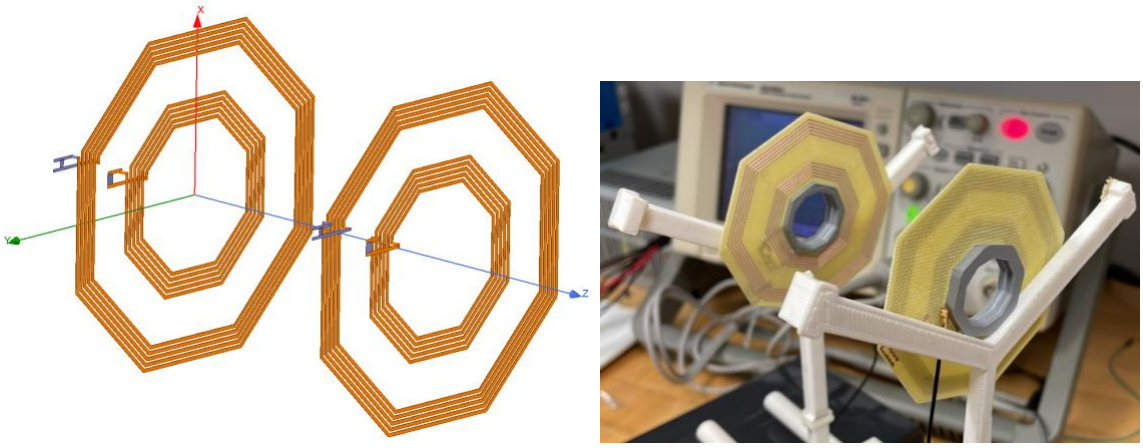

Figure 5.2. CAD model and experimental setup for measuring the power transfer efficiency in a 4-loops resonance- inductive link operating at 6.78 MHz.

For measuring power transfer efficiency and power delivery to load, particularly in multi-loop resonance-inductive links, the Tx and Rx resonators are coupled to the resonance capacitors and R_L, making the system a full 2-port system with the multi-loops resonance-inductive link. The network analyzer is then used to measure the S-parameters. In the two-part configuration, power transmission efficiency in percentage terms is calculated by setting the S_{21} or S_{12} to Magnitude mode at a power of 2 and multiplying the results by 100.

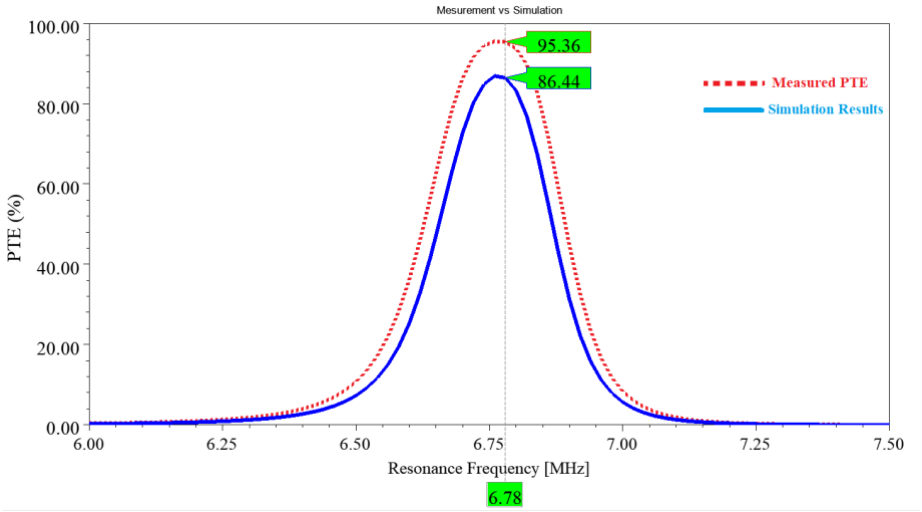

Figure 5.3. Comparison of the proposed powering link's measured and simulated power transfer efficiency in 60 mm coupling distance.

Figure 5.3 compares measured power transfer efficiency with HFSS simulation results from Ansys software. In the simulation, the suggested link has a power transfer efficiency of 95.36 %, and we tested 86.44% using a network analyzer, which is entirely consistent. The fabrication and measurement process errors account for 7% of the variation between measured and simulated results.

5.2 Frequency Shift Compensation-Capacitive Effect

The capacitive impact of foreign items in the vicinity of the proposed link reduces power transfer efficiency. This phenomenon directly impacts the resonance frequency shifting to higher or lower frequencies (Figure 5.4). The effects of the head on the nominal transmission frequency are the same. The frequency shift is prevalent in wireless power transmission, but it must be adjusted quickly after being detuned. The most practical solutions are employing a varactor, a variant capacitor, or an advanced switching three networks to include the most suitable capacitors from a capacitor bank in the WPT link.

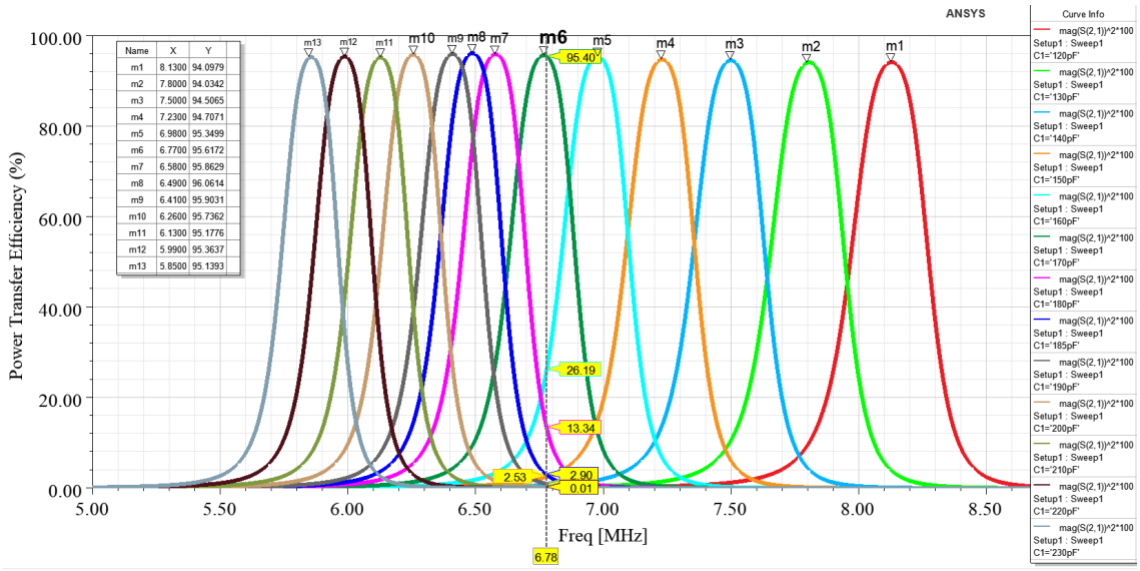

Figure 5.4. Capacitive effect of the power transmission link (HFSS simulation results).

Any frequency shift due to misalignment or other external causes can be adjusted by including the most appropriate capacitor in the WPT link. So through this way, the link will promptly be turned back to a nominal operating frequency (6.78 MHz). As shown in Figure 5.4, when the EEG cap is worn, the powering link operating frequency for the precisely adjusted resonator moves from nominal operating frequency to 7.5 MHz, but by switching the capacitor from 160pF to 170pF, the frequency shifts back to 6.78 MHz again. The measured results of capacitor effect on wireless power transmission efficiency, tabulated in table 3.4, show that the measured and simulated findings data are in good agreement.

A Figure of Merit (FoM) is a metric that describes how a system or technique performs compared to its alternatives. Figure 3.47 shows how the FoM graph compares PTE's simulation results to measured data to evaluate the consistency of the simulation approach and testbed measurement results. This graph gives us an idea of whether the simulation is accurate and reliable for developing the proposed WPT system. In addition, we can better understand how to compensate for the frequency shift caused by the subject's head proximity effect or foreign object disturbance on the powering link. In Figure 5.6, the relative consistency and matching between simulations and

measurements as a major factor for link design validation demonstrates that the intended WPT system is appropriately designed and fabricated.

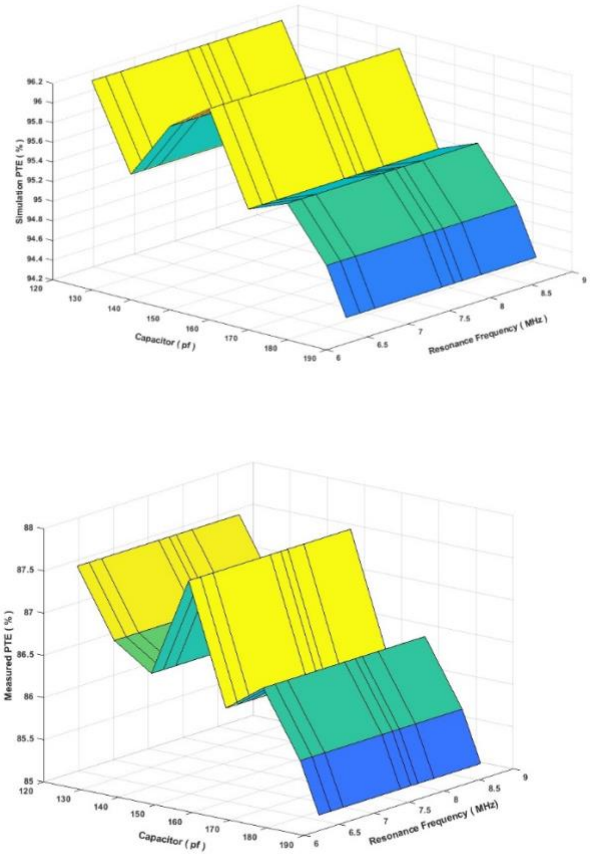

a) b)

Figure 5.5. The Figure of Merit comparison for simulation results and measured data vs. capacitor and resonance frequency: a) Simulation results b) Measured data.

The resonance inductive link's PTE variations due to capacitive effects are summarized in Table 5.1.

Table 5.1 Measured data of capacitor impact on wireless power transmission efficiency

Capacitor Value (pF)	**Resonance Frequency (MHz)**	**Simulation PTE (%)**	**Measured PTE (%)**
120	6.48	96.10	87.43
130	6.65	95.25	86.64
140	6.83	95.84	86.34

150	7.65	96.12	87.53
160	7.80	95.20	86.11
170	7.90	95.36	86.44
180	8.13	94.83	85.67
185	8.80	94.35	85.07

5.3 Coupling Distance Effect on Link's Power Transfer Efficiency

As shown in Figure 5.6, to evaluate the coupling distance influence on power transfer efficiency, an expandable 3-D printed testbed is designed and fabricated. By sticking Tx and Rx resonators in each holder, we can measure the influence of distance on the WPT link by increasing or contracting the distance between the resonator holders. As seen in Figure 5.7, when the distance between the Tx and Rx resonators increases, the power transmission efficiency drops inevitably. The simulated coupling distance variations on the link's PTE show that a distance of 80mm between Tx and Rx still yields above 50% power transfer efficiency, which is sufficient to run the front-end electronics while still considering the subject's safety concerns.

A 3-D graph for coupling distance variation versus PTE’s simulation results and PTE Measured data is shown in Figure 5.8. The distance variation and the link’s power transfer efficiency is measured. PTE values are summarized in Table 5.1.

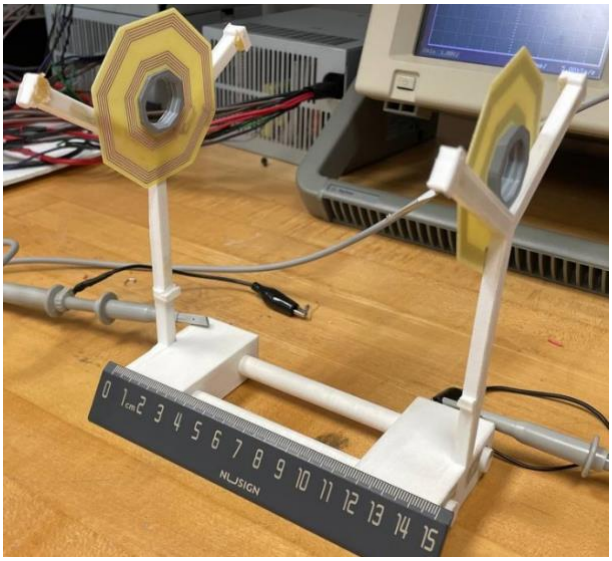

Figure 5.6. A testbed to evaluate the coupling distance effect on power transfer efficiency

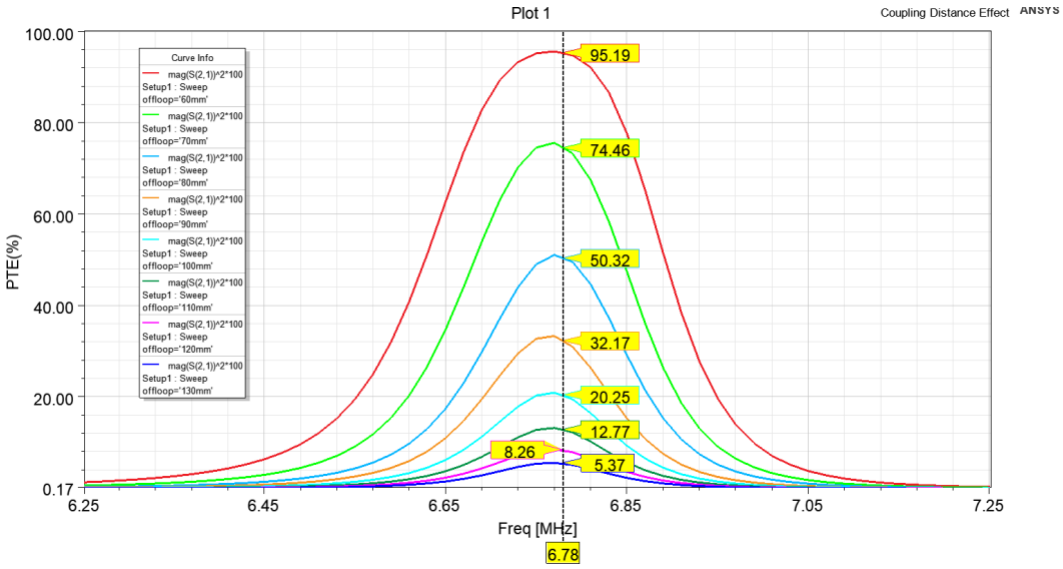

Figure 5.7. link's power transfer efficiency versus Tx-Rx coupling distance

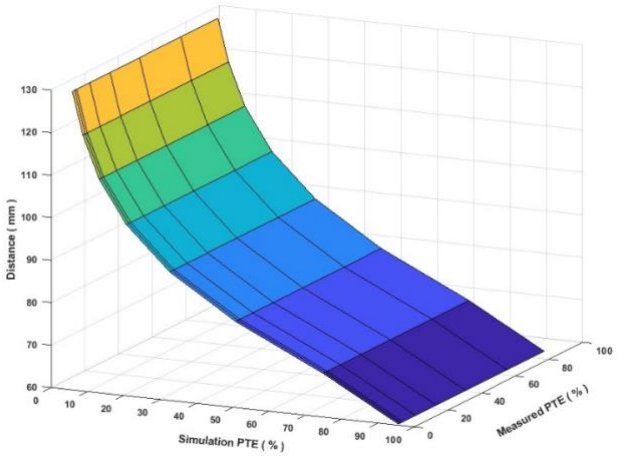

Figure 5.8. Coupling distance variation vs. Simulation PTE results and measured PTE data.

Table 5.2 Simulation and measured data of coupling distance variations impact on wireless power transmission efficiency

Distance (mm)	**Simulation PTE (%)**	**Measured PTE (%)**
60	95.19	86.44
70	74.46	65.43
80	50.32	40.91
90	32.17	23.46
100	20.25	11.32
110	12.77	3.67
120	8.26	2.48
130	5.37	1.09

5.4 Planar 20-way Octagonal Power Combiner

In the WPT procedure, the power received by the Rx resonators should be delivered to the rectification unit. The received power may originate from multiple resonators concurrently due to the power receiver's particular structure, which includes multi-Rx resonators designed to prevent the detrimental impact of misalignment on PTE. In practice, based on the subject's head position

on the powering pillow, the most suited Rx resonators are paired with Tx powering ones. Combining the acquired power can be difficult, but a well-designed 20-way power combiner operating at 6.78 MHz can be a highly successful solution. For this goal, many power combining techniques have been investigated. The combining corporate approach is an ideal solution for combining the received power from a few resonators. As the number of resonators grows, the total length of lossy transmission lines grows consequently, resulting in a parasitic resistance and capacitance effect that causes considerable power loss. The suggested wireless power transmission and conversion chain was a circular power combiner comprising microstrip transmission wires. The configuration proposed is both planar and compatible with the remaining powering subsystems. A low-loss planar microstrip circular form power combiner is designed and manufactured using the described technology.

Figures 3.51 show the CAD view and the fabricated prototype power combiner's design. A two-layer PCB with 0.031 inch thick FR4 substrates is used in the proposed combiner. The input and output tracks of the combiner are printed on the top metallization layer, while the bottom layer acts as ground. As shown in Figure 5.9, the combiner's input component comprises 20 identical exterior Surface Mount U.FL Receptacle, Male Pin, connected to the combiner's core through a tapered microstrip transmission line. The line's characteristic impedance rises linearly from 50 at the perimeter, where the input ports are, to 100-ohm in the center, where all 20 tapers meet on the circumference of a central circle. Using a taper aims to increase the impedance in the center circle, where all 20 tapers meet.

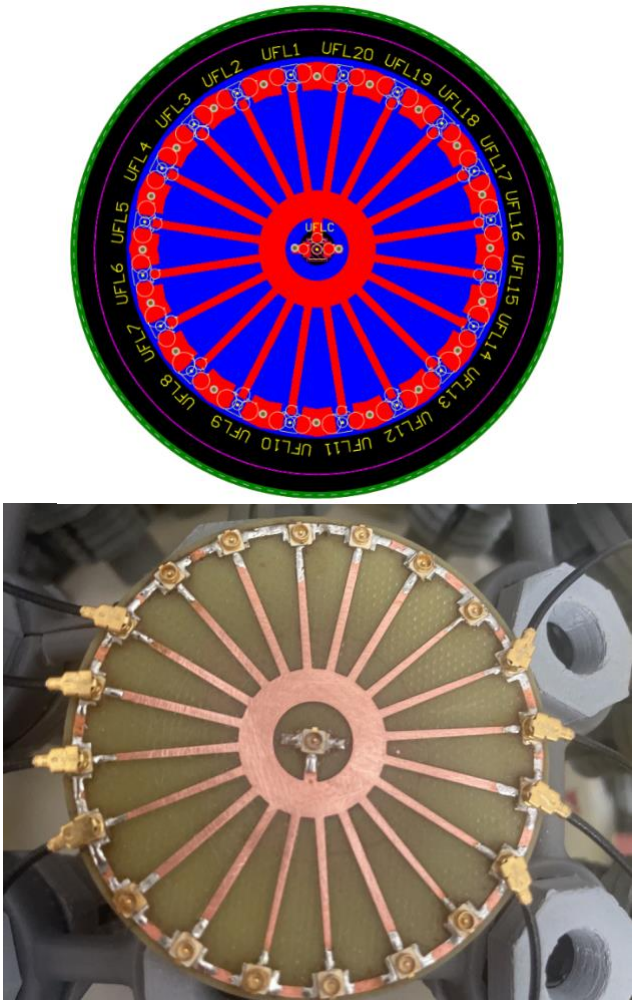

a) b)

Figure 5.9 a) CAD View and b) The fabricated circular power combiner 20*1

The circular substrate form architecture provides additional advantages while being compatible with the remainder of the Tx-Rx setup. By raising the impedance of the tapers at the center, we may increase the overall impedance at the central point. Very long tapers cannot be fitted in the available space without the proper arrangement. This issue might result in a large size power combiner and minimal lines, decreasing the power handling and PDL of the powering link. RA U.FL Resonators are connected to the power combiner using a male cable with a core diameter. The via ends in a center ellipse on the output side serves as the launcher. The input ports have a significant amplitude imbalance when utilizing a round disk as a launcher. We can keep

the amplitude balance by transforming the circular disk into an ellipse and optimizing its major and minor axes. The primary purpose of the output section is to transmit the received power signal from the through to a 50-ohm output connector. Although this appears to be a simple operation, the substantial impedance mismatch between the Via and the output port makes it more challenging. Because a low impedance microstrip line is approximate twice the width of the via and cannot be effectively connected to the via, a simple taper between this via and a 50-output port is impossible. Two parallel lines were employed to transmit the received power from the through to the output port to fix the problem. Figure 5.10 shows the measured return loss of the output port ($S_{n,out}$, n=1 to 20), and a comparison to the simulation result, demonstrating good agreement between selected input and output ports. AS seen from 2 MHz to 10MHz, the output port has a return loss of lower than -27 decibels which indicates that the received power doesn't get reflected and will be delivered efficiently to the output port.

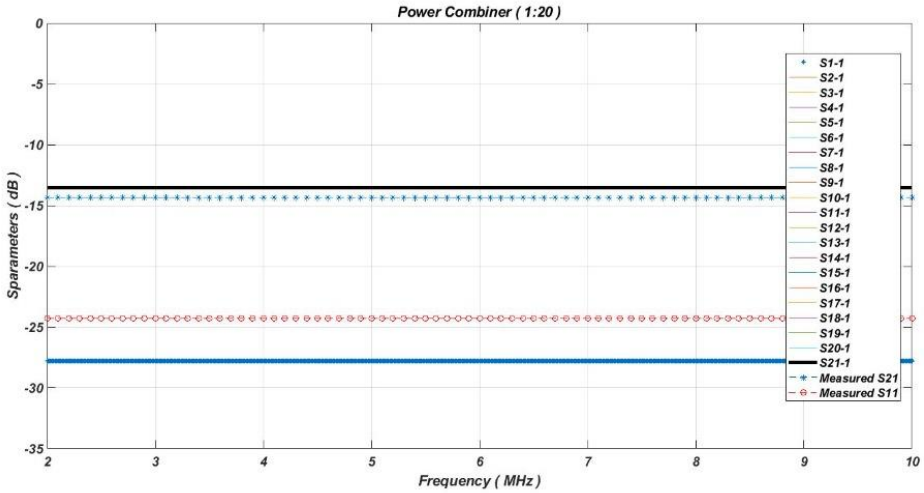

Figure 5.10. Simulated and measured return loss of the output port.

5.5 Power Transmitter Resonator Array (Back-end Tx Testbed)

The methodologies suggested in the preceding sections led to the design and fabrication of a power source for any wireless electrophysiological experiment on freely rotating or moving

subjects, such as the human head, that would eliminate the need for batteries for continuous operation.

As shown in Figure 5.11, the wireless power supply can be employed with an approach that combines an array of resonators (9 or more planar resonators) and power drivers for wireless power transmission with magnetic sensors for subject positioning. The suggested fabricated powering system can be employed in experiments requiring real-time biological data gatherings, such as neurological signals, body temperature, pressure, blood ph level, and experiments requiring continuous electrical or mechanical stimulation.

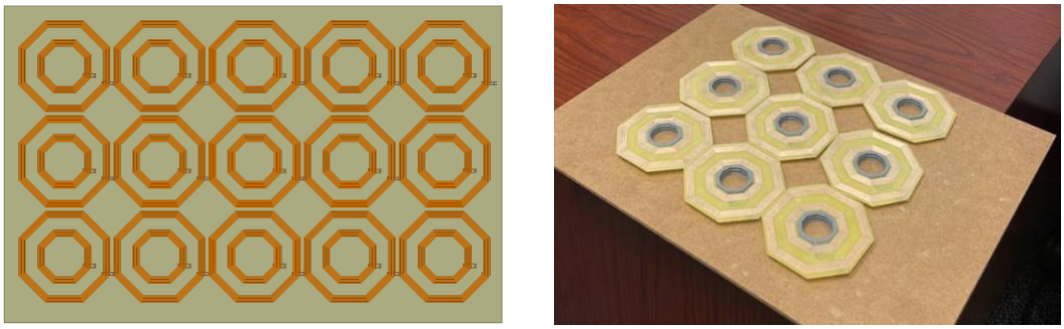

Figure 5.11 CAD model and experimental setup for powering resonator array.

3.11.6 Power Receiver Resonator Array (Front-end Rx Testbed)

Current wireless wearable neural recording systems developed for neuroscience applications have a primary constraint. They require the patient to carry a considerable payload of batteries for continuous recording over several hours or even days. As a result, users of such gadgets must find a balance between the length of the experiment and the weight of embedded batteries. We used resonance inductive power transfer technology to power our recommended Tx-Rx system, allowing neuroscientists to conduct brain interface research on a daily experimental testbed (Tx embedded in a pillow and RX placed on an EEG cap) without having to change batteries. The power receiver resonator array consists of 15 or more planar resonators installed in a 3-D printed

EEG cap, as seen in Figure 5.12, to wirelessly receive energy from Tx and power up multichannel neural interfacing devices.

Figure 5.12 CAD model and Fabricated setup of power receiver resonator array (Front-end Rx array mounted on EEG head cap).

Chapter VI: EEG Read Out System's Front-End Electronics/Electrode and bio amplifier

6.1 Introduction and Prior Works

This chapter aims to study active electrode technologies for acquiring EEG data with sixteen or more channels using a unique, cable-free, battery-less setup. This aim demands a thorough examination and understanding of existing technologies. The next step is to create a design and improve the proposed system. This chapter examines the performance of current state-of-the-art procedures and existing medical standards for creating a package containing an EEG capturing electrode and a bio amplifier to establish the system's qualifying requirements. To capture EEG signals, amplify them, filter out noises, and prepare them for the digitization unit, in this chapter, as the fourth major stage of the proposed wireless and battery-free EEG readout system, we need to design a cost-effective, easy-to-use, lightweight, portable, and long-lasting EEG signal amplifier unit. This chapter covers several decades of literature and design. Excellently suitable objects were researched to acquire further study for a functioning overview. The system was broken down into modules, each representing a different aspect of its operation.

Brain control interface systems based on EEG data are now more ubiquitous and simpler. These gadgets allow users to control many machines or cars merely by thinking about them. Because nearly all wireless BCI systems rely on batteries to function, energy management is critical to extending their lifespan. Battery life is limited, so low power consumption modules are essential in the design, but it comes with low spatial resolution and poor EEG signal quality. However, through this thesis, we are willing to study how to eliminate the final power line and use resonant inductive coupling to wirelessly transmit the required energy to the EEG cap, using modules with better spatial resolutions.

6.1.1 EEG Capturing and Monitoring Systems

As seen in Figure 4.1, Electrodes, differential amplifiers (one for each channel), analog-to-digital converter (ADC), and data processing and visualization device are the five essential components of multi-channel electroencephalography systems. On the other hand, modern multi-channel BCI systems now feature wireless data transfer in their system (see Figure 6.1) [265-267]. Depending on the architecture, some systems are augmented by additional pieces, such as hardware filters, pre-processing data units, etc.

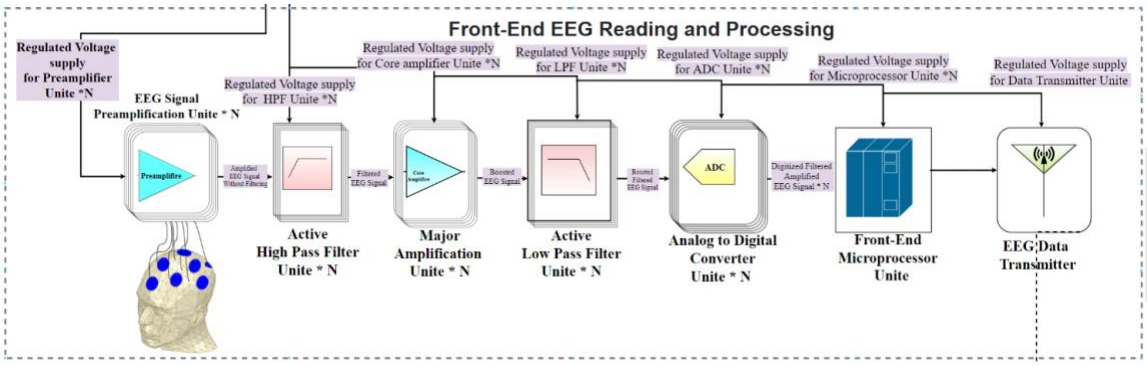

Figure 6.1. Block diagram of EEG measurement and recording subsystems

The EEG recording electrodes are critical for obtaining high-quality data. Different kinds of electrodes are now utilized in EEG recording devices, including disposable, reusable silver/gold disc electrodes, headbands, electrode caps, saline-based electrodes, needle electrodes, etc. Wet and dry electrodes are the two types of non-invasive scalp electrodes. Wet electrodes provide better signal quality due to better skin contact and lower electrode-tissue impedance. Ag/AgCl disks are among the most preferred electrodes placed for multi-channel EEG systems with many electrodes. Because high impedance (greater than 5k) between the brain and the electrodes might cause distortions, impedance measuring sensors are frequently included in current EEG recording equipment [268].

Pre amplification and amplification unit are essential parts of modern EEG measuring systems because the magnitude of the EEG signal obtained from the scalp is just a few μvolts. These amplifiers must fulfill specific standards in hopes of avoiding distortions. First and foremost, they must have a high input impedance (at least 10M) to ensure that the signal being monitored is loaded as little as possible. Aside from that, the input circuit needs to offer safety, as any current flowing over the amplifier's input terminals can alter the signal getting monitored. The amplifiers should also include isolation and control circuitry. The current through the electrode circuit is kept at a tolerable range, and any artifact caused by that current is eliminated.

Further, the amplifier's output impedance must be smaller than the load impedance, and it must operate within a specific frequency spectrum to provide the best signal-to-noise ratio (SNR). Differential amplifiers are used in modern EEG systems, which receive data from bipolar electrodes. The differential amplifier must have a high common-mode rejection ratio (CMRR) (at least 120dB) to avoid interference from the common-mode signal [269].

6.1.2 Metrics in EEG recording amplification Unit

Amplification unit design is a significant factor in front-end EEG recording systems, as it lowers power consumption, noise, electrode offset and increases common-mode rejection ratio (CMRR).

In most cases, wearable EEG recordings are non-invasive, meaning no external object is implanted into the subject's head. Contact electrodes are placed at predefined standard spots on the subject's head skin, and electrolytic gel is often used to lower the skin's resistance and improve signal strength. However, on the other hand, signals with an amplitude of 100μV are detected inside the scalp (intracranial electrodes like Utah electrode) of a human subject, and movements with an amplitude of roughly 1-2μV are seen on the surface of the cortex regional contact electrode using Ag/Agcl [270]. The EEG signal spectrum's bandwidth is usually less than 50 Hz (1Hz to 50Hz).

The electrodes used in the EEG readout system might be bipolar or single-polar. In the unipolar measurement technique, we compare each electrode's potential to the reference electrode or the electrode's average potential, whereas bipolar measurements examine the potential difference between two electrodes. Both techniques contribute to the debate on signal perception [261]. Another essential metric is ETI, which stands for the electrode-tissue interface. The ETI measures the impedance between the electrode and the surface tissue, impacting signal quality, and increased ETI can degrade signal quality.

A capacitor and a resistor can create a circuit model, an equivalent electrode circuit for the electrode-tissue interface. Figure 6.2 shows a dry electrode equivalent circuit with an interface voltage of V_{In}.

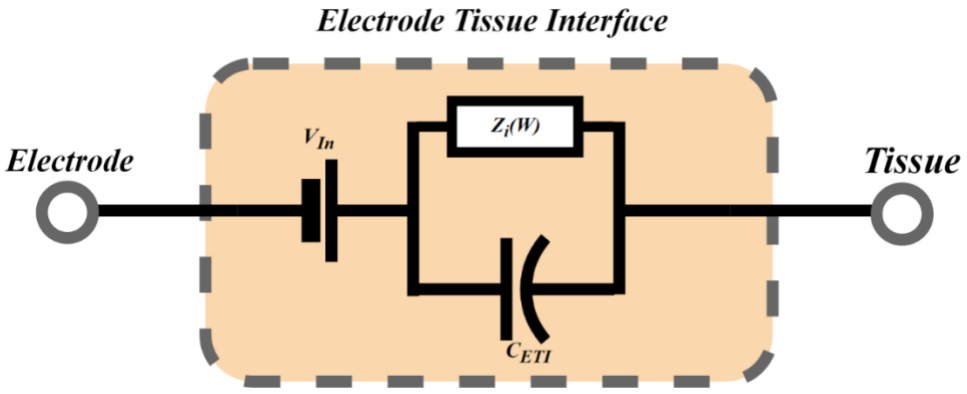

Figure 6.2 Electrode Tissue Interface circuit model

Because of their excellent signal quality, low polarization voltage, and low baseline drift, Ag/AgCl electrodes are the most preferred. These non-polarizable electrodes can be used for DC measurements. Some electrodes are expensive and polarizable, such as gold or platinum electrodes. Even though they can create powerful signals, they cannot make DC measurements [272]. Numerous rhythms can be found in the EEG data, classified into frequency bands. These bands include but are not limited to the alpha, beta, delta, and theta bands. A thorough investigation has been conducted to determine the cause of varied wave patterns and their relationship to brain health [273], but they are out of the scope of this dissertation.

In an efficient EEG readout system, attempts must be undertaken to eliminate noise and unsound signals from the collected EEG data even early in the signal route. The quality of equipment, such as amplification and buffering, impact the noise level. Whether physiological or not, unwanted signals are commonly referred to as artifacts. Electromagnetic fields created by the body are known as physiologic artifacts. Physiological artifacts are signals released by surrounding muscles and hearts for enhanced amplitude electromyography (EMG) and electrocardiography, but they are not caused by undesired interference from nearby electronic equipment (ECG) [274]. The low spatial resolution of EEG readout devices is a significant shortcoming compared to other neuroimaging approaches. High-density EEG systems with 126-256 channels have evolved to address this problem, although they have several downsides, such as a lengthy set-up time [275].

On the other hand, an EEG system with a single channel is a popular topic now. Because such devices only have one measurement channel, this approach does not seek to achieve high spatial resolution. However, a limited number of channels allowed for a faster setup and increased user comfort [276].

Conventional EEG recording devices usually necessitate considerable effort (around 45-60 minutes [277]). When the channels are connected to local processing systems through cables, typical EEG recording devices become highly voluminous, which may prevent surveillance during ambulation. Almost in any of these systems, an electrolyte gel matches Tissue-electrode impedance, but the gel eventually dries up, reducing signal quality and necessitating electrode replacement [277].

As mentioned in chapter 3, providing a reliable source of energy for the system, on the other hand, is a significant issue as well. The power line limits the user's comfort and using the large batteries might be risky and challenging to manage by hand. However, this problem could be solved by our suggested wireless and battery-free EEG recording device using dry electrodes. This alternative would be more tempting to consumers if it came with a more comfortable and discreet headset. As mentioned above, dry electrodes have a high impedance at the electrode-tissue contact,

which increases noise and interference from the surroundings, either physiological or electronic equipment, which is one of the main disadvantages of using them. In addition, one other significant drawbacks of dry electrodes are the existence of motion artifacts in the recorded data. To rectify this issue, active electrodes (AEs) have been created, and they are a strong competitor for providing reliable EEG data that may be used for further processing [277]. Such amplifiers integrated with electrodes must meet a variety of highly exact requirements, and the superposition of a more significant signal of noise and interference complicates the work. Through this dissertation chapter, a bio-amplifier is designed at the system level to prepare the desired movement so that the ADC and subsequent electrical equipment may appropriately interpret it. The electrode-measured EEG signals are the inputs to the amplification process. They are commonly separated into five elements: First, the signal sought is the EEG signal which can be a delta, theta, alpha, and beta. In addition, there are unwanted signals from various sources, including physiological and non-physiological signals that originate from the body or nearby electrical equipment. The interference from power lines (50/60Hz) is another leading noise source. The interference at the electrode-tissue interface is a significant issue that must be addressed by a decent hardware design. Finally, flicker noise is the dominant noise in this range of frequency.

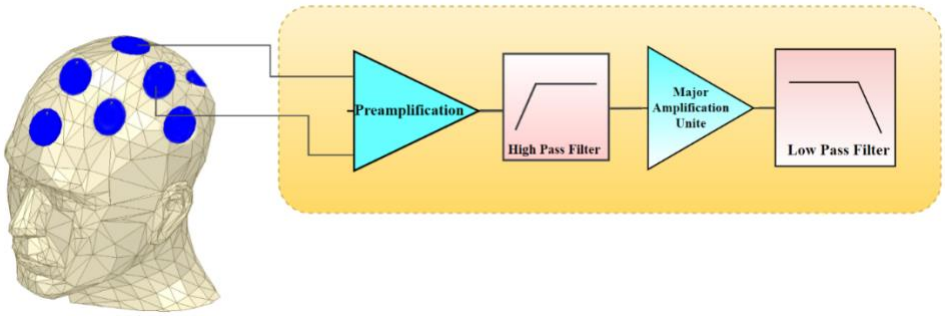

Figure 6.3 Conventional EEG readout system block diagram

The preamplifier is perhaps the most crucial phase since it manages the first signal modification and might be the decisive factor in signal quality. An effective bio amplifier design can reject the undesired components above. The high- and low-pass filters aim to prevent

interference caused by electrode polarization voltage and noise cancelation by limiting the amplifier's bandwidth. The core amplifier offers the required isolation between the subject being tested and the electrical equipment while simultaneously amplifying even more [288-290]. Instrumentation amplifiers can be used to construct the initial step in the preamplifier unit since they have a high input impedance, low noise, high CMRR, high open-loop gain, low DC offset, and low drift. In addition, because EEG signal amplitudes on the scalp are roughly 1-2 mV, the IA should have an input-related inaccuracy in the nV-mV range [281], so the IA should have a common-mode rejection ratio (CMRR) of greater than 120 dB to compensate for this.

6.2 Instrumentation Amplifier Circuit

the three-opamp structure is the most general IA topology. Switched capacitor, capacitively-coupled, current-mode, and current-feedback topologies are other topologies. IA's 120dB CMRR criteria are difficult to satisfy, especially given existing circuit design approaches that demand trade-offs on other essential metrics. As a result, there are two options. First, to enhance the CMRR, even degrading the different design's important components. Another alternative is to reduce the CMRR requirement by raising the bio amplifier’s common-mode input impedance, which is possible with active grounding. The reference electrode is actively pushed to the common-mode voltage observed at the measuring electrodes rather than grounded. The reference electrode then delivers the inverted common-mode potential back to the measurement electrodes, thereby attenuating the common-mode signal. This matter is referred to as a driven-right-leg (DRL) circuit [282]. Considering Figure 6.5, a driven right leg (DRL) circuit is typically added to a biopotential amplifier to reduce the common-mode voltage (i.e., increase the common-mode rejection ratio, CMRR). The basic biopotential amplifier is an instrumentation amplifier with a buffer and single output amplification stages. The DRL is introduced after the first step, as shown in Figure 6.5. The driven right leg funnels some common-mode voltage away from the first stage

but before the second. The DRL enhances the CMRR by functioning as an antenna to pick up EMI from surrounding power lines or other electrical equipment.

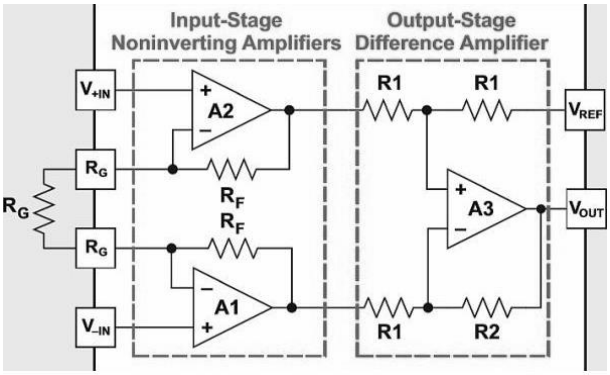

Figure 6.4 The three Op-Amp IA configurations

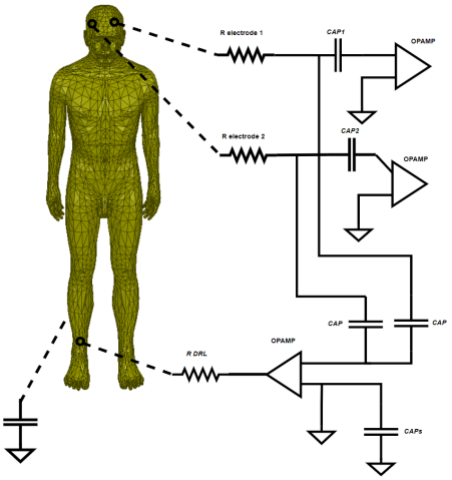

Figure 6.5 Active Grounding Drivel -Right Leg DRL for One Channel EEG readout system

6.3. Single-channel versus multi-channel EEG recording system

The use of only one channel to record brain activity raises particular challenges, which they're all related to the limited amount of data that a single track may acquire. Another challenge is separating the intended source from unwanted signals originating from other brain sections or nearby muscle tissue. So, various blind source separation techniques are required, such as independent component analysis.

The essential components of (A) a multi-channel EEG system and (B) a single-channel EEG system are shown in Figure 6.6.

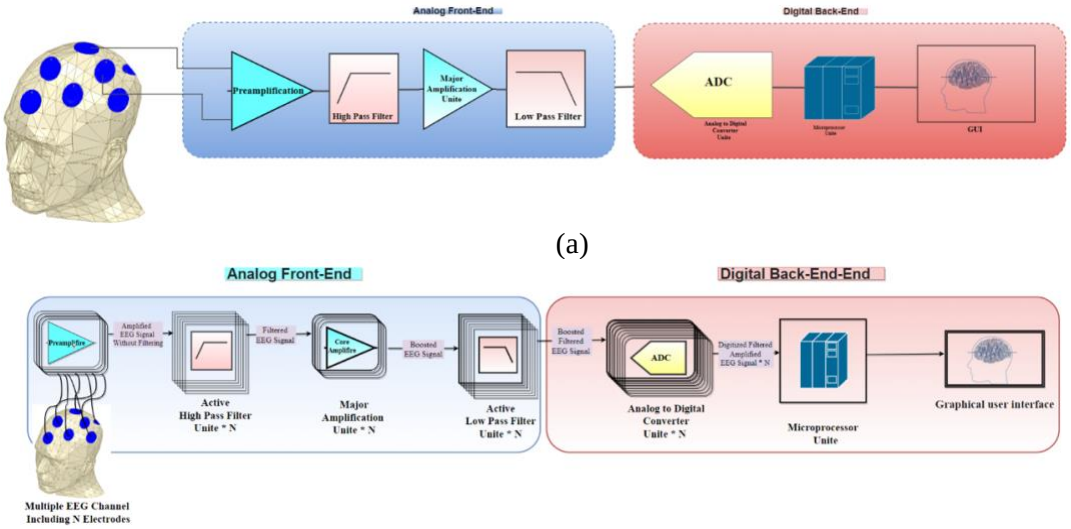

Figure 6.6. (a) a single-channel conventional EEG system and (b) a multi-channel EEG system

Because one of the critical purposes of single or multichannel EEGs is long-term and transportable recording, the device's power consumption is a significant concern. Because large, heavy batteries detract from the device's attractiveness, eliminating the battery as a power source is needed. Another stumbling block in deciding the recommended Electroencephalography cap is the amount of data transmitted from any channel; this is crucial in multi-channel systems. On the other hand, compressed sensing is a relatively new approach based on data compression concepts [283]. This technology can save energy by shortening desired signals in real-time, lowering the amount of processing power required for subsequent stages in the signal path.

6.4. Active Electrode

Numerous cables are frequently used in conventional EEG readout systems for the power supply and data transfer between the active electrode and the back-end electronics. The number of

linking lines between the dynamic and back-end systems can impact system cost, complexity, and preparation time. We need a portable, enjoyable, easy to set up, and straightforward approach to develop a wireless and battery-free EEG readout system. However, the designer must consider several key metrics, including CMRR, spatial resolution, electrode polarization, and DC electrode offset. An AE-based (Active electrode) EEG read-out system is depicted in this Figure 6.7. The suggested EEG readout cap arrangement requires an active electrode because motion artifact is a primary concern in such a system. Thanks to its low output impedance, the active electrode reduces motion artifacts by preventing parasitic current from entering the channels. Furthermore, active electrodes can maintain signal quality without using cumbersome and visible shielded wires. More crucially, given the limited number of leads and tiny integrated circuits utilized in the design, the power consumption and power loss in active electrodes are significantly lower than in other comparable topologies, making it ideal for application in a wireless and battery-free arrangement.

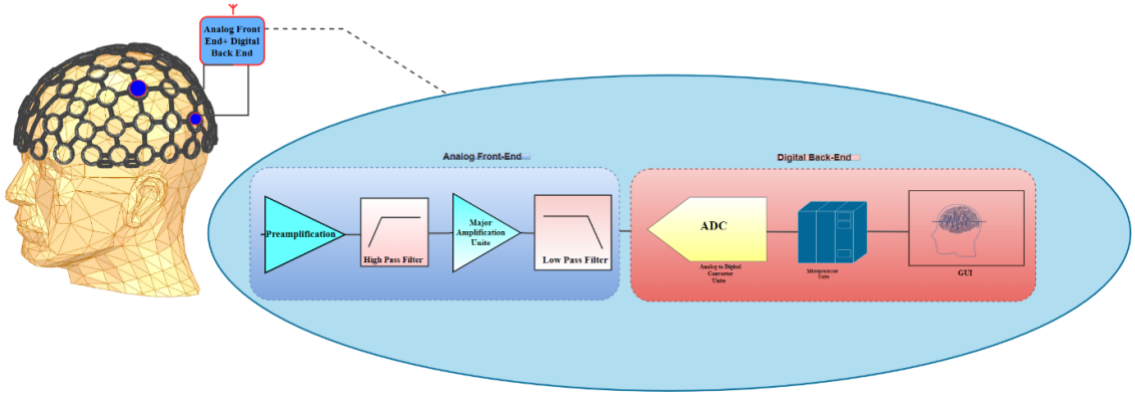

Figure 6.7. Active Electrode AE based EEG readout system

Various aspects must be considered when designing active electrodes, including noise, electrode offset tolerance, common-mode rejection ratio (CMRR), input impedance, power dissipation, and the number of wires. The following measures must be considered for designing active electrodes:

1. The system should have a maximum input-referred noise (IRN) voltage of 6 mV_{pp}, which translates to a root mean square (RMS) noise of 0.91 mV_{rms}, to comply with applicable medical device rules from the International Electrotechnical Commission (IEC) [284].

2. The electrode offset is the difference in polarization voltage between electrodes, as high as 100mV. As a result, the active electrode may saturate and lose dynamic range. According to IEC standards, the EEG system should withstand a 300mV electrode offset [285].

3. At 50/60Hz, the IEC recommends an input impedance greater than 100MW. A high input impedance is essential to avoid gain attenuation in the active electrode. The voltage division generated by electrode-tissue impedance and the amplifier's input impedance causes gain attenuation. The voltage divider resembles the input impedance substantially higher than the ETI [286].

4. with Active electrodes, the number of cables and wires will no longer be an issue because the proposed EEG readout system and, as a result, active electrodes are designed primarily for wearable applications and are powered by a wireless source (e.g., Tx, Rx resonators through WPT).

5. The power consumption of a suggested wearable EEG readout system is critical due to safety concerns. One of the main criteria is not surpassing the body tolerance threshold, so we must design the subsystems to consume less power. Furthermore, one of the primary determining factors for the system's size is the size of the resonator and power control unit, which may impact user acceptance. Consider a 3.6 V conventional WPT in continuous operation. The current of the EEG reading device is regulated to 5mA for the system to remain operational for as long as the test takes, bearing in mind all safety rules. In addition, a mismatch between the dry electrodes and the amplifier's restricted input impedance is the fundamental CMRR constraint in wearable applications.

6.4.1 Active Electrode Architectures

Because an analog buffer only provides high input impedance and no voltage gain, succeeding circuitry must meet the same noise and offset tolerance conditions, resulting in higher power consumption. AC-coupled inverting amplifiers with capacitive feedback have been used extensively [287]. Its low power consumption, low noise, rail-to-rail offset rejection capability, and tiny size contribute to this. But Low-frequency rhythm acquisition, such as in the sigma, theta, and mo bands, is not possible using AC-coupled amplifiers because they suppress low-frequency signals. On the other side, because of the dynamic range necessity, these amplifiers have a restricted electrode offset tolerance, which impacts gain. Furthermore, high-resolution ADCs (>16 bit) are necessary to eliminate noise, which increases the system's power consumption.

6.4.2. Noise Cancellation Challenges for AE Circuit Design

1/f noise (or flicker noise) is the most common noise source in amplifiers [288]. This matter has various disadvantages since parasitic capacitance increases, affecting the amplifier's size and the input impedance. Alternative procedures that do not require negative trade-offs are available. Chopper stabilization and autozeroing are two dynamic techniques that could be used [289]. The Auto zeroing approach captures undesired noise at the amplifier's input or output and subtracts it from the signal. The CHS technique modulates the signal to a higher frequency where the 1/f noise is negligible after amplification, then demodulates it [290].

As a result of this strategy, the offset and low-frequency noise is pushed up to a higher frequency, resulting in output ripple. A ripple reduction loop is one solution to this problem (RRL). This includes sampling and modifying the ripple to send a compensation voltage proportional to the ripple back to the origin [290].

6.5. Technical Metrics for Active Electrode Design

6.5.1 Electrode Offset

Another difficulty is the signal's DC offset caused by the electrode-tissue interface. Typically, the DC offset is 20-50 mV and 1000 times larger than the acquired signal. A low-noise instrumentation amplifier amplifies EEG signals and eliminates the DC offset. As previously mentioned, placing a capacitor at the input can avoid the electrode offset. A DSL connection is an attractive choice. This method uses a closed-loop active system to verify that the desired DC component is present at the output [291].

6.5.2 Common Mode Rejection Ratio

Two main components influence the amplitude of the CMRR for active electrodes: first, Electrode tissue impedance mismatch, and second, gain mismatch in two independent, active electrodes. It must be mentioned that increasing the amplifier's input impedance as much as feasible is a common way to reduce electrode-tissue impedance mismatch. It's more challenging to reduce the gain mismatch between the active electrodes because they're on different boards. The primary circuit strategies used to overcome this problem are common-mode feedback (CMFB) and common-mode feedforward (CMFF). The DRL topology is the most prevalent CMFB technique utilized in amplifiers. The downside of DRL circuits is that they are prone to causing instability. CMFF circuits are believed to be easier to build and show more stability. Rectifying the common-mode signal before amplification at each active electrode is being tested. The common-mode current is neutralized by connecting the reference inputs of the active electrodes [292].

6.5.3 Input Impedance

The non-inverting amplifier architecture has a high input impedance and is a preferred initial general planning at the system level. However, a highly successful circuit design method for

impedance boosting is called impedance bootstrapping at the circuit level. This method is based on positive feedback, which sends the amplifier's output back to the input, resulting in a higher effective input impedance. A voltage or current feedback can be used [293].

6.5.4 Power Dissipation

In circuit-level design, the noise specification is the determining factor for the device's power consumption. It is well understood that increasing the drain current to reduce thermal noise results in increased power dissipation. Current reuse is a new circuit design technique that uses n-channel and p-channel MOSFETs (NMOS and PMOS) as input transistors. The input transconductance is doubled without increasing the tail current. The drawback of this method is that the dynamic input range is reduced by half [294].

6.5.5 Number of Wires

Active electrodes frequently require a cable or track connections for power, analog/digital output, clock, data, CMFF / CMFB, reset, and other tasks. The circuit's complexity determines the number of wires needed and the design approaches used. One method for minimizing the number of cables is to combine the active electrode output with the power supply via a current source driver [295]. Another option is to combine the active electrode digital I/O signals or pulse-width-modulation (PWM) to mix the clock and data lines [305]. Furthermore, the digital active electrode concept significantly decreases the number of wires by including a five-wire bus to transport digital I/O signals, power, and other feedback leads. Given the vastness of the design space and the fact that attempting every possible component combination to find the best solution takes time, it's vital to carry out the design systematically and orderly. Even though the metrics used to assess the quality of digital circuits differ from those used to evaluate the quality of analog circuits, efficiency, size, and energy consumption all impact their performance. Other constraints and the circuit layout dominate the quality of analog circuits.

6.6 Design of an Active Electrode Preamplifier for Single-Channel EEG readout system

This section will demonstrate designing an active electrode preamplifier unit for a single-channel EEG recording system. However, the objective was not to develop a new architecture but to enhance and modify an existing one to the application's requirements. To learn as much as possible about current knowledge and technology, the first step is to conduct a thorough literature study. The design requirements were determined, and the appropriate architecture and circuit design methodologies were adopted to enhance the amplifier's functionality. This chapter aims to improve single-channel EEG signal quality by upgrading current active electrode circuit design methodologies. This method may provide a feasible alternative to unsatisfactory standard EEG systems in diagnosing various illnesses by giving high-quality signals in single-channel EEG recordings. The quantity of noise level is influenced by the quality of measurement equipment, such as the amplification and buffering stages. Unwanted signals that are either physiological or non-physiological are referred to as artifacts.

6.6.1 Electronic Circuit Design Analysis Type

6.6.1.1 Transistor Sizes

The power and noise level are essential in determining the transistor size. The appropriate circuit is created based on a literature study and current state-of-the-art designs for the proposed setup. The Current Feedback Instrumentation Amplifier was chosen as the circuit topology (CFIA). Throughout the chapter, several tools were used, either because they were essential or just because they simply aided in obtaining the desired goal. In the electronic circuit design process, the CadenceR VirtuosoR environment was employed. The schematic design, circuit simulation, and layout design were all part of this. The CadenceR SpectreR circuit simulator was used to do SPICE-level simulations, part of the VirtuosoR environment. Finally, when it was time to set the transistor pair architectures during layout design, the constraint management tool came in helpful.

6.6.1.2 Transient Analysis

Cadence's transient analysis evaluated the circuit's transient response to different input signals. There were five distinct types of analysis carried out. The circuit's reaction to a large input signal step was also studied to ensure stability. The circuit's response to a sinusoidal input at various frequencies was also studied. The input signal frequencies were chosen to fit inside the amplifier's bandwidth constraints, with a second simulation conducted at a frequency in the center of the bandwidth range. Finally, a transient model is simulated using actual EEG data from an online database resource. The EEG data was converted into a format that could be read by the Cadence environment using a Verilog-A block.

6.6.1.3 Common-Mode Input Range

The common-mode input range of the circuit is determined by doing an ac analysis in Cadence and sweeping the common-mode input voltage. The circuit's gain behavior and dc operating points were next investigated. The constraints of the common-mode input range were recognized, and the circuit continued to function correctly.

6.6.1.4 Maximum Input and Output Swing

Analyzing the amplitude of an input sinusoidal signal and assessing the consequent output signal evaluated the circuit's highest input and output swings. The maximum input swing was calculated just before the output saturated, and the maximum output swing was also determined. This issue was accomplished in the same manner as the transient analysis.

6.6.1.5 Input Impedance

Calculating the inverse of the current at the amplifier's input yielded the input impedance. Cadence's ac analysis and a current probe were used to measure.

6.6.1.6 CMRR

The amplifier's differential gain and common-mode gain calculated the CMRR. The common-mode gain may be calculated similarly by short-circuiting the amplifier's inputs. As a result, by dividing

the differential gain by the common-mode gain at the required frequency, the CMRR may be calculated.

6.6.1.7 Power Consumption

The overall power consumption of the circuit is calculated using a dc analysis in Cadence. Also, checking the components' operational measures helps us estimate the required amount of power for this unit. The current across all branches may then be summed together, and the power consumption can be calculated using the power source's voltage.

6.7 Design Process and System Components

The functionality of state-of-the-art solutions and current medical norms for EEG recording systems were investigated to identify the essential specifications for the system to meet. According to the IEC and IFCN standards, the preamplification unit must satisfy the following requirements: The input voltage range must be around 0.5mVpp, and the input-referred noise voltage per channel should be 0.91 μVRMS in the range of 0.5 to 100 Hz. The bandwidth should be between 0.17-100 Hz, electrode offset must be above 300 mv, and the input impedance should be above 100 MΩ. It was chosen to develop a current-feedback instrumentation amplifier that met the IEF and IFCN standards and the active electrode requirements (CFIA). The CFIA was then tweaked to fit the application's demands, and a few circuit approaches were applied to increase its performance. CFIA configurations are the most appropriate IA for being more efficient, having a lower CMRR, and creating negative rail output voltages as an instrumentation amplifier. In this layout, the gain of the instrumentation amplifier is defined by two resistors, and resistor matching does not affect the CMRR.

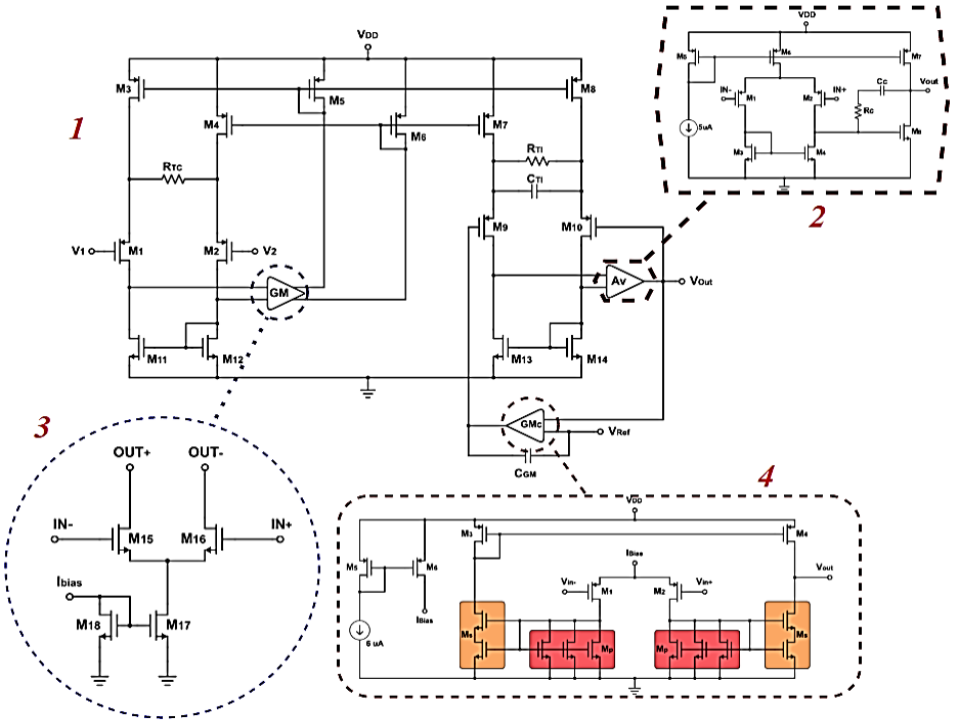

(a)

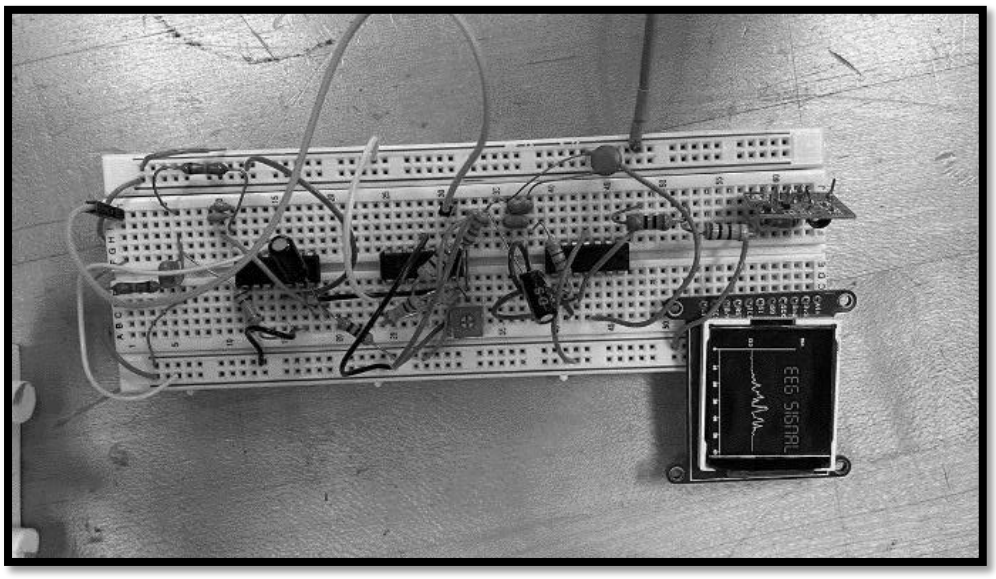

(b)

Figure 6.8 Optimized proposed pre- amplification unit CMOS designed based on CFIA (a) Experimental evaluation modular design of preamplification unit (b)

6.7.1 Parametric Analysis and Optimization of MOSFET and Simulation Results

This section simulates the amplification of actual EEG data by optimizing the W/L ratio and parametric sweep of resistor and capacitor values. The suggested architecture is a current forward instrument amplifier, as described in [296], and we try to tweak the parameters to achieve the best results possible. For MOSFET technology, the gate length stated is the minimum length. It can be longer than the minimal length in design. The transconductance and current capacity, and multiplicity factor m are all factors that influence the W/L ratio. For a given Vg, a larger W/L ratio improves current gain and, as a result, current. The same is true for a higher m, which denotes mW/L. In reality, big transistors with large W/L ratios or/and large m are beneficial for gain stages. The differential input stage of OpAmps, for example, requires a lot of gains. However, the input differential stage's proper matching must also be regarded. We must also comprehend the circuit's geometrical sensitivity. So, if it's a biasing circuit, such as a current mirror, or a current source that has to match another source on the die, we'll need to lengthen it and make the width a notional 5um use numerous legs to size it. Make sure that all matching transistors have the same orientation and layout, with the multiplier being the only difference. Devices with the most petite length and breadth have poor compatibility. The MOSFET parameters are optimized and listed in Table 6.1 using the notes mentioned above.

Table 6.1 CFIA components operating points, sizes, and values (refer to 1 in figure 6.8)

MOSFET	**W/L(Micro)**	**I_{DS}**	**Passive components**	**Value**
M_1,M_2	720/7.2	8	R_{TC}	8KΩ
M_3,M_4,M_7,M_8	360/18	8	R_{TI}	200 KΩ
M_5,M_6	720/18	14	C_{TI}	50nF
M_9,M_{10}	90/9	8	CGM	10UF
M_{11},M_{12}	36/144	8		
M^{13},M_{14}	144/144	8		

Table 6.2 The voltage amplifier components' operating points, sizes, and values (refer to 2 in figure 6.8)

MOSFET	W/L(Micro)	I_{DS}	Passive components	Value
M_1,M_2	14.4/1.44	8	R_C	100Ω
M_3,M_4	36/7.2	8	Cc	100 pF
M_5,M_6	72/3.6	14		
M_7	36/3.6	8		
M_8	36/7.2			

Table 6.3 Operating points, sizes, and values for the OTA components (refer to 3 in figure 6.8).
1

MOSFET	W/L(Micro)	I_{DS}
M_{15},M_{16}	90/2.6	15
M_{17}	28.8/14.4	40
M_{18}	72/3.6	20

Table 6.4 Gm-C filters trans conductor component operating points and sizes (see 4 in figure 6.8).

MOSFET	W/L(Micro)	I_{DS}
M_1,M_2	144/3.6	2
M_3,M4	72/90	0.4
M_5	360/72	8
M_6	180/72	7
M_p	18/360	1.5
M_s	7.2/540	0.45

Additional transient simulations using EEG data from an alcoholic patient were conducted for the alternative AE CFIA [73]. The data was collected at the scalp's Fz electrode location. Figure 4.9 depicts a simulation of a 1.3-second section. The DC drift seen in Figure 6.9 is caused by the input signal's DC component being filtered out; however, as previously explained, it may be recovered at the DSL's output and coupled with the AC component at subsequent stages in an active electrode system.

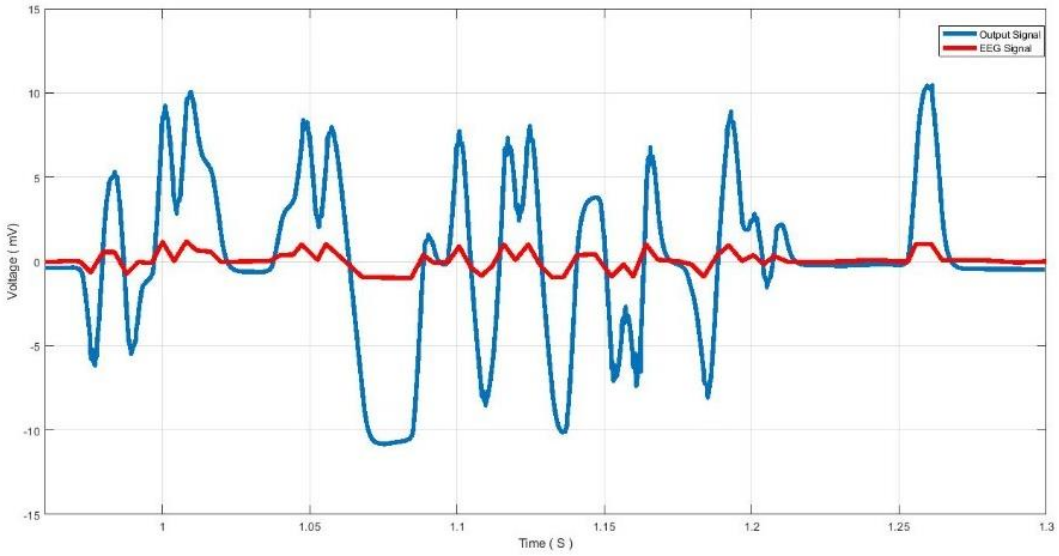

(a)

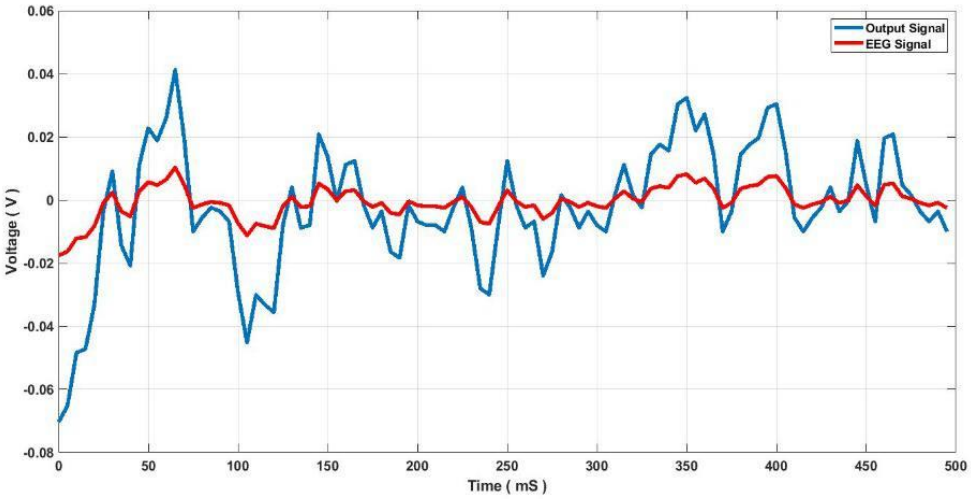

(b)

Figure 6.9 Signal Amplification using the CFIA circuit The time response of the CFIA to a given signal (red) and amplified using the CFIA circuit (blue) ,(b)The time response of the CFIA to the actual EEG signal (red) amplified using the CFIA circuit (blue)

Chapter VII: Filter, Analog-to-Digital Converter (ADC)& Microcontroller

7.1 Filters

Filters are necessary for developing explainable EEG measurements while capturing and visualizing EEG signals. Various EEG waveform parts might be incomprehensible if we don't filter the EEG spectrum. Filters would have multiple effects on the EEG signal, ranging from minor to significant. The fundamental advantage of filters would be that filters seem to wipe up the EEG pattern, providing a way to read and thus more visually appealing. Filter configurations could also be utilized to highlight specific forms of EEG waveform. On the other hand, Filters can sometimes be misunderstood, and their use can often result in the undesirable interpretation of EEG signals. While the comprehensive study of filter design also isn't required to analyze EEG signals, knowing the electronics or techniques used to construct these filters can help improve filter performance and the complexity of EEG reading.

7.1.1 The Most Common Way to Choose a Filter for Electroencephalography

The ideal filter design would filter out any noise from physiological or electrical sources from the EEG, leaving only genuine brain activity to get through. However, there are no intelligent filters, and filtration can effectively exclude signals based on mathematical limits. These generalizations are founded on the premise that the brain exclusively creates EEG waves in a specific frequency range. Therefore, any activity in and around that scope that is unusually slow or rapid activity is unlikely to be caused by the human brain nervous system.

Furthermore, a few of the basic tenets of EEG filter design would be that activity under 1 Hz higher than 35 Hz doesn't originate in the brain and is most likely a physiological or electrical artifact. EEG filters are typically set up to refuse a significant proportion of high-frequency activity. Another filter disregards the large percentage of very low-frequency activity, founded on the idea

that the frequency of about most brain electrical impulses of involvement lies within a particular bandwidth. The bandpass refers to the frequency range permitted to pass through the filter arrangement between these undesired high and low frequencies. Different bandpasses are connected to different filter configurations in a novel method. Filtering methods can sometimes draw out the specific band of EEG signals waveform that would otherwise be concealed in other, higher voltage activity instead of discarding erroneous action. Ones working with EEG signals may dampen slow waveform in a recording, even if it reflects genuine brain activity, emphasizing quick activity that would otherwise be lost amid high-voltage slow waves.

7.1.2 Type of Filters

Low-frequency, high-frequency, and notch filters are the three most prevalent filter categories in commercial and therapeutic Electroencephalography. A low-frequency filter's function filters unwanted low-frequency waveforms while leaving high-frequency components alone. Designers refer to low-frequency filters as high-pass filters since they mitigate low frequencies while allowing high frequencies to get through the rest of the setup. On the other side, high-frequency filters are meant to block out high-frequency waveforms while allowing low-frequency signals to get through and are commonly alluded to as low-pass filters by designers. Even though the phrases high pass and low pass are widely used in electronics to describe filters, they are not the favored phrases in therapeutic electroencephalography. The terms high-frequency filter (HFF—filters out the high frequencies) and low-frequency filter (LFF—filters out the low frequencies) are used interchangeably in commercial or medical EEG, with the labels high filter (HF) and low filter (LF) being referred as short and acronyms. As a result, HF and HFF are interchangeable, and LF and LFF are alike.

The next sort of filter is the notch filter. Its goal is to block out waveform that occurs at a given frequency instead of a sampling frequency. Electric fields created by 60-Hz power line signal in the nature surrounding us in our interior habitats commonly affect the EEG since the AC in

conventional electric plugs in the United States oscillates at 60 Hz. This undesired signal is attenuated or eliminated using sixty-hertz notch filters built mainly to filter out the 60-Hz activity. 50-Hz notch filters are applied for the same reason in locations where power line frequencies are 50 Hz. When a low-frequency filter encounters a sinusoidal waveform precisely at its cutoff frequency, it reduces the amplitude by around 30%. Signals with frequencies less than that are suppressed by more than 30%; the lower the wave's frequency, the more dampened it is. Surprisingly, sinusoidal waves with frequencies slightly above the cutoff frequency also decrease in size primarily by filter but by a smaller than 30%. The less the sinusoidal wave's outset the standard frequency of the low-frequency filter, the less the filter influences it. The significant impact of using classic low-frequency filter selections for lower frequency filters, such as a cutoff frequency of 1 Hz or below, would be to help maintain each EEG channel inside the horizontal region, preventing significant displacements upward or descending through into area of many other channels. This is because the standard displacing is a very low-frequency signal. Higher cutoff frequencies, such as 3 Hz or 5 Hz, dampen delta frequencies initially, whereas as higher cutoff frequencies are used, they practically erase specific slow activity, frequently with the extra advantage of showing out some other elements of the EEG. When actual EEG signals are filtered, the oscillations delivered to the filter have mixed frequencies. Even in wave mixes, the filter tends to reduce each harmonic component of the oscillations according to the roll-off characteristic rule. Low-frequency filters are particularly beneficial for removing artifacts generated by patient movements, which can cause a channel's background to change and other low-frequency noise causes. High-frequency filters also include a roll-off function, but it works opposite to LFF roll-off curves, with higher frequencies dropping off to the right [298].

7.2 Analog-to-Digital Converter (ADC)

An essential component of wireless& battery-free EEG recording equipment is an analog-to-digital converter (ADC), which may save a lot of energy if the architecture is designed well. An analog to digital converter captures an analog voltage at a particular instant and transforms it into a digital output code that replicates the original value. The resolution of the A/D converter determines the number of binary digits (bits) used to represent this analog voltage value and the analog-to-digital converter (ADC) is one component of this system that can considerably minimize energy usage by decreasing the amount of data [299]. To choose the most optimal ADC, a research evaluation of EEG signals and BCI systems is conducted first to identify the prerequisites for ADC choosing. Then, using these criteria as a guide, a detailed analysis of synchronous and asynchronous ADCs is carried out to identify their strengths and drawbacks and their suitability for target applications to choose the best type for use in front-end design. Based on a review of power consumption, sampling rate, resolution, and ADC Coding Complexity among synchronous and asynchronous analog to digital converters, successive approximation register analog to digital converter is the most beneficial option for our target application.

7.2.1 Successive Approximation Register Analogue-to-Digital Converter

Whenever the input voltage is compared to the output of an N-bit DAC during the counting process, a register monitors the comparator's output (high or low) to detect if the binary count is higher than or less than the analog signal input and modifies the bit values accordingly (Figure 7.1). The outcome of the SAR correlates to the value of the analog input signal and forms the foundation of the SAR ADC serial output as each bit is determined. It's also worth noting that the internal DAC determines the accuracy level and smoothness of the SAR ADC.

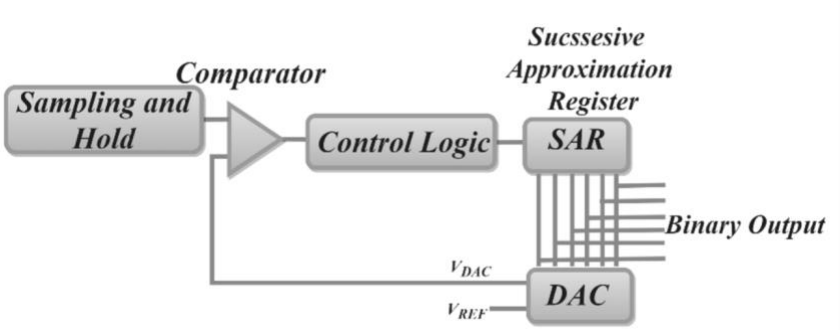

Figure 7.1. block design successive approximation registers

SAR ADCs are often utilized in low-power, medium-to-high-resolution systems with sample rates of up to 200 MS/s. Low latency, excellent precision, low power dissipation, energy usage, and a simple design are the key benefits of SAR ADC. SAR ADC cumulates on the input signal quicker than Digital Ramp ADC and has a fixed sampling rate. Because of the benefits listed above, the SAR ADC is among the most often utilized ADCs for bio-potential monitoring. SAR ADCs come in a range of power consumptions, sample rates, resolutions, input and output choices, prices, and packaging designs [300].

7.2.2 SAR ADC's Efficiency in terms of energy

SAR ADCs consume the lowest energy of any ADC, particularly whenever the resolution is between 4 and 10 bits, and the sampling rate may be a few KS/s. According to the current study, a SAR ADC with the energy usage of 717pW for 8-bits and 1 KS/s [342] and 3nW for 10-bits and 1 KS/s may be built. The energy usage for better resolution applications is likewise substantially greater, although still reasonably modest. For instance, a desirable 12-bit SAR ADC costs 100nW (1 KS/s), but an 18-bit SAR ADC requires 30.52mW (5MS/s).

7.2.3 SAR ADC Coding Complexity

SAR ADCs have one SAR, one DAC, one comparator, and a logic control unit, but their analog architecture is costlier and more sophisticated than a Digital Ramp ADC; hence they are

considered moderate sophistication. With 100nW of energy usage, 12-bit resolution, and a sampling rate of 20 KS/s, the best SAR ADC will take up 0.3mm2 of the silicon die [300].

7.2.4 SAR ADC Resolution and sampling rate

Recent technical advancements have allowed SAR ADC resolution to be increased to 24, although most SAR ADCs are in the 8-18-bit range. The rate at which samples are taken. Latest developments in SAR ADC architecture have increased the sample rate to the GS/s range, although this is solely true for low-resolution SAR ADCs. One of the most optimistic cases is a 36 GS/s, 6-bit, 110mW SAR ADC; however, for needed 12-bit resolution, the sampling rate may be as high as 36 MS/s with nW power consumption.

7.3 Microcontroller Unit

A microprocessor module is a high-speed, input-output (I/O) computer that can handle many tasks. The microcontroller unit can supervise all signal processing units and command and start data flow between them. Because all additional electronics that the microcontroller unit may need are already available, it does not necessitate peripheral components for functioning. For the proposed Wireless and battery-free EEG readout system design, such characteristics minimize the required room, resulting in power optimization and the time for manifesting fabrication [301]. There is no standard protocol for choosing a microcontroller unit for the desired purpose. It's a challenging task to balance the running energy required and the energy usage of the microcontroller unit and its peripherals. The advent of new, improved devices besides new novel and better capabilities might make selecting the microcontroller unit tiring. The additional characteristics necessary for this section of the dissertation push us to hunt for smaller parts to reduce the occupied space on the EEG control board. Bus architecture, interconnection, the possibility of using internal Digital signal processors (DSP), power usage, an elastic memory, and technical assistance are all characteristics that must be considered.

Dialog Semiconductor and Atmel were the brands evaluated (Arduino). Considering our system design, the following sections offer the most appropriate choices for these two corporations.

7.3.1 Different types of Microcontroller

7.3.1.1 Dialogue Semiconductors:

Dialogue Semiconductors has many Smart bond chips in its product category, from the DA14580, which has a 32-bit ARM Cortex M_0 microcontroller, to the DA14680, which has an 8 Mb FLASH and 64 kB OTP memory. Throughout the selection process, the primary qualities identified in the various systems were the system architecture, power control, and versatility in connection, such as SPI, UART, and Bluetooth [369]. The other type, DA14680, attracted attention thanks to the high integration and complete Bluetooth 4.2 capability, low energy usage, and tiny dimensions. The DA14680 differs from the DA14681 because it contains flash memory, infinite processing space, and over-the-air upgrades [375]. Its ARM CPU has a 16kB cache that may function in direct, two-way bidirectional, or four-way associative mode.

Furthermore, the cache line can be programmed to be 8, 16, or 32 bytes. The DA14680's CPU may be tuned to unutilized an XTAL16 crystal oscillator (16 MHz) or a relatively low energy consumption PLL to raise the frequency to 96 MHz, enabling complicated methods to be implemented with no external or particular microcontroller unit. This component's energy management makes it perfect for wirelessly powered portable designs. A universal constant current/constant voltage (CC/CV) charge, which enables the support of WPT powering, and a State-of-Charge engine, which manages PTU when the system is active, are two major power management features [302].

This module also has three-phase power rails that may drive peripherals like Vsys, V_{flash}, and Vext. The Dialog SmartSnippets Studio was used to create the DA14680 and all other members. Dialog SmartSnippets Studio is the application framework for all Smart Bond products, and it's made up of a SmartSnippets toolkit that covers all app developers, FLASH or OTP programming, and

testing. The SmartSnippets IDE is an Eclipse CDT-based IDE with pre-configured modules that simplify building and debugging.

7.3.1.2 Atmel

Atmel offers a variety of micro-control unit boards designed on chips, including the Arduino Leonard, which is based on the ATmega32u4 microprocessor, and the Arduino Uno, which is based on the ATmega328P. The constraints mentioned earlier, such as connection (SPI, UART, and Bluetooth) and programming freedom, restricted the accessible possibilities while looking for the perfect solution. The following subsection presents the Arduino gadget that was chosen (Atmel).ATmega328 board sparked our curiosity to be chosen as a Microcontroller unit since it is small, complete, and breadboard-friendly, plus it is based on the ATmega328. Six of the fourteen digital input/output channels on the Arduino Nano could be used as pulse modulation (PWM) outputs. It also features six analog channel inputs and a quartz crystal with a frequency of 16 MHz. The Arduino Software (IDE) is used to program the Arduino. Because the ATmega328 on the board included a bootloader software that allowed directed loading of the code, a hardware interface programmer had not been required to program the board. An external power source, such as a wirelessly powering up, can power the Arduino Nano through the WPT link. The Nano's Atmel MCU contains 32kB of memory, of which the bootloader consumes 0.5kB. Furthermore, SRAM requires 2kB, while EEPROM requires 1kB [303].

7.3.2 MCU Comparison

Without evaluating the restrictions and peculiarities of any device, it is impossible to identify which MCU should be used for the proposed EEG readout system as a modular design. The given MCUs and their fundamental properties are summarized in Table 7.1. The MCUs shown here are interesting, but the DA14680 is perhaps the most suited MCU for this application, as it uses the ADS1298 in daisy-chain mode. Furthermore, the BLE offers configurable charging capabilities, a

slim design, and the flexibility to reduce the number of components necessary. This MCU allows the project to expand, allowing for a more significant number of ADC.

Table 7.1 MCUs types & properties [304-310]

MCU	**DA14680**	Atmega328
Flash	8Mbit	32KB
SRAM	16KB	2KB
Clock Speed	1 MHz	16MHz
Analogue 1/0	31 general purpose	8
DC Current per 1/0	10µA	40mA
Digital 1/0	-	22
Input Voltage	1.7-4.75V	7-12V (operational SV)
Bluetooth	BLE device	Peripheral device
Changed mode	Programmable	External device
CPU type	ARM Cortex -MO	AVR
SPI	2	1
1/0 Supply Class	1.8,3.3	3.3

According to what is reported in publications so far [311-314], the processing unit can vary from microcontrollers with limited capabilities to super small microprocessors with a great deal of performance operating in the GHz range of frequencies or even greater frequency, based on the target application and needed computing capabilities. Microcontrollers will integrate microchips with operating frequencies of 1 GHz or more based on the desired application and required computational capabilities. Even a high-performance CPU is unsuitable for wirelessly powered EEG recording equipment. Although we can provide a large quantity of power for the analog front end, we are mainly concerned with human safety due to the allowed power transmission. Machine learning and other computationally intensive processes must be executed locally on a computer's

back-end unit. This project's CPU was chosen to provide the required maximum analog front-end sampling speed of 1 kbps and wireless sensor components necessary for network connectivity.

The ATmega line of minimal CMOS 8-bit microcontrollers, including the 640/1280/1281/2560/2561, is developed on the AVR improved RISC design. The ATmega 640/1280/1281/2560/2561 delivers throughputs approaching 1 MIPS per MHz by performing strong directives in a single clock cycle, enabling the system developer to balance energy usage vs. computational and processing performance. The Atmel® AVR® core has 32 working registers and an extensive instruction set. The Arithmetic Logic Unit (ALU) is linked directly to all 32 registers, enabling two autonomous registers to be accessible in a single program performed in a single clock cycle. The resultant design is more code efficient than the conventional CISC microcontrollers, with a throughput of 10 times quicker [315].

7.4 Transmitter

7.4.1 Bidirectional Communication link for power management unit

One option to keep the received power stable is to use a closed-loop system to change the transmitted power so that the received power stays marginally higher than the minimal level required to make our EEG recording equipment operational. Furthermore, wideband bidirectional data communication may be created by utilizing the same short-range wireless link or a separate near-field/far-field link. IMDs (implanted microelectronic devices) is an excellent example of how power and data transmission lines may be linked. Increasing the number and electrodes improves the quality of perception in EEG recording systems. These devices can use tens to thousands of EEG channels to record brain activity, and they often demand a lot of power and bandwidth [316]. Data transmission has been a well-known subject that employs various high-data-rate technologies. We have specific circumstances in wearing EEG readout systems, either positive or negative. To decrease total weight and volume, such a suggested system should operate for longer durations

without needing an additional battery. As a result, the device must have a low power consumption to last a long time without recharging for the individuals' comfort.

The received power information is delivered from the EEG setup to the back-end TX, either by back telemetry based on load shift-keying (LSK) or actively together with data [317]. A digital-to-analog converter (ADC) digitizes the rectifier voltage to produce power bits for digital transmission,

The rectifier voltage is compared to a reference voltage, and a power bit is delivered to the Rx. A detecting circuit receives the data in the external unit, and a control unit provides the appropriate voltage for the PA through a power-efficient DC-DC converter [318]. These efforts have produced an application-specific integrated circuit (ASIC) to shut the power loop through a lengthy and expensive procedure.

Most commercially available wideband wireless technologies, such as Bluetooth or WiFi, which run at 2.4 GHz, are incompatible with the requirement of our setup. Medical Implant Communication Service (MICS), which operates in the 402-405 MHz range and has a restricted bandwidth (300 kHz), is an example of a particular standard for data communication.

Carrier-based modulation methods have been employed in the majority of inductive telemetry lines. Such approaches include amplitude shift keying (ASK), frequency-shift keying (FSK), binary/quadrature-phase shift keying (BPSK/QPSK), and load shift keying (LSK). These carrier-based approaches were appealing in the early days of wearable or IMDs since the same low-frequency carrier could power the setup.

Because the power carrier's frequency cannot be raised due to tissue loss at high frequencies, the power carrier must be separated from the data carrier in high-performance wearable applications that demand additional bandwidth. Furthermore, because these approaches rely on carrier signals, they also consume significant Tx power. Wideband communication with high-frequency data

carriers involves the adoption of expensive and power-comsuming frequency-stabilization RF circuits, not desired in our suggested EEG configuration.

The use of ultra-wideband (UWB) technology for low-power communications was permitted by the Federal Communications Commission (FCC) in 2002. Short-range ultra-low-power applications quickly embraced a form known as impulse-radio (IR) UWB, in which data is sent through sub-nanosecond pulses via wideband antennas. The lack of a carrier in IR-UWB transmitters eliminates the need for high-frequency oscillators that consume a lot of power, resulting in lower power consumption. The IR-UWB is a suitable choice for IMDs because of these properties. The standard IR-UWB is highly absorbable in water and cannot penetrate or pass through tissue, which is a drawback. It is designed for far-field interactions in the 3.1-10.6 GHz range.

Given the difficulties of adopting carrier-based modulations, a novel pulse-based data-transmission technique known as pulse-harmonic modulation (PHM) might effectively push the bounds of energy usage and data rate (DR) in near-field telemetry systems.

Despite the wide bandwidth of pulse-based techniques, the intense power-carrier interference on the Rx side may overpower the faint data signal, making data restoration difficult, though perhaps not unattainable. As a result, power-carrier interference must be filtered out, increasing the Rx's power consumption and complexity. Pulse-delay Modulation (PDM) is a breakthrough dual-band data and power transmission technology for wideband near-field applications that exploit undesirable power-carrier interference on the wireless data link (due to the proximity of the power and data coils) to transmit the data. The proposed approach saves both power and space by filtering out power carrier interference. It also takes advantage of IR-low-power UWBs and low-complexity characteristics, particularly Tx, to further reduce EEG cap power consumption. The primary benefit of using a single carrier for both power and data transmission is that power coil coupling is relatively stable, resulting in more reliable data transfer. Another

advantage is that the power resonators may be reused several times, saving space. It achieves high power transfer efficiency and high data-transmission capacity on the same carrier. The fundamental problem is that changing the power carrier significantly complicates the power Tx circuitry and reduces the power transfer efficiency. The low frequency of the power carrier is another critical issue since it decreases data transmission capacity to insufficient levels for most wireless applications. The primary advantage of utilizing a single carrier for power and data transmission is that power coil coupling is generally steady, resulting in more reliable data transmission. Another benefit is that the power resonators may be reused several times, resulting in space savings.

Due to competing objectives, obtaining high power transfer efficiency and high data-transmission capacity on the same carrier will be difficult. The core issue is that altering the power carrier makes the power Tx circuitry more complicated and lowers power transfer efficiency. Another significant difficulty is the power carrier's low frequency, which reduces data transmission capacity to levels insufficient for most wireless applications. However, a separate power carrier from the data carrier is recommended for high-performance since a wearable EEG cap with more channels necessitates a broader bandwidth requirement. And also need to consider that increasing the frequency of the high amplitude power carrier may cause dangerous temperature increases in the tissue due to excessive power loss. It is the other reason for separating power and data channels. A high-frequency carrier (> 50 MHz) is essential for the data connection to achieve effective communication; however, the power carrier frequency should be kept below 20 MHz due to human safety issues. Due to human safety issues, the power carrier frequency should be controlled below 20 MHz. The data link is also built to provide bidirectional high-bandwidth communication with wearable or implantable devices.

7.5 Modular Design

Because of the noisy and unpredictable nature of the EEG input, implementing a wireless and battery-free is a complicated process. Advancement in this area is limited by authentication, design expertise, and evaluation for such systems. To record non-stationary EEG signals in μv ranges, high-quality and high-resolution front-end electronics are necessary. Professional and high-quality EEG capture hardware is available from several businesses. Due to their high cost, these devices are not designed for widespread public use or research entry-level research. However, no designer can disregard the concept of modular hardware design. Modular electronics design is the technique of linking multiple electrical devices into a single system. The standardized electrical connections used in electronic gadgets are employed to accomplish this aim. While it would be preferable to design and fabricate all the subsystems on a single chip using the ASIC design technique, modular architecture provides its benefits.

The number of components that can be crammed onto a PCB is limited, and a single-PCB design may not fit into the enclosure if you're developing for items with restricted space. By dividing the procedure into many modules, it is possible to verify that all the components fit within the space restrictions. Some of the suggested setup's components will likely become outdated. We will only need to modify a piece of the circuit when an update is required by retaining fast-changing elements on the same module. We may repurpose the same module for multiple items designed based on a modular design. It reduces the time and the cost of redesigning and lowers the cost-per-unit when more of the same module is produced. Modular hardware enables testing to be limited to certain portions of a circuit without breaking traces. Faulty modules may be easily identified and replaced, making troubleshooting and maintenance more straightforward.This modular and vertically stackable development board can acquire entry-level EEG signal acquisition. Additionally, the suggested architecture allows the system to be readily scaled and tailored to various EEG activities while still power, cost, and time.

There are a lot of publications that detail the concepts and models of EEG capturing and processing that have been developed in recent years.[318] describes a wearable device EEG recording set up with including 32 channel active dry electrode for epilepsy monitoring. The system is battery-powered, and the analog data is converted to digital signals by the ADS1299, a 24-bit resolution analog-to-digital converter unit capable of sampling up to 1 ksps. The processor is a 1 GHz ARM CPU, with Wi-Fi 802.11 b/g as the data communication route. The device's size was not optimized, necessitating the usage of longer cables and active electrodes. In [319], A 16-channel EEG cap cape has been developed with the cup AM3358 ARM Cortex-A8 1 GHz CPU. The ADC is ADS1299 and can sample at one ksps. Such a system for battery-powered portable applications is still a significant hurdle.

[320] describes a battery-powered EEG device for long-term monitoring of schizophrenia patients. The CPU is a SAM G55 microcontroller, and the ADC is ADS1299. Bluetooth communication is used as a communication link, and overall power consumption is 69 milliwatt. [321] released details of a low-cost 8-channel EEG recording equipment for BCI applications. The design was committed to favoring compact size and low power use, using an STM32F4 microcontroller, a single ADS1299, and communicating data through Bluetooth.

Due to being battery powered, most of the devices described lack spatial resolution for EEG, and overall board expandability was not considered. [322] represents a novel re-design for an ECG acquisition system that includes a 24-bit ADS1298 ADC. The ADC and controller modules are an 8-channel analog-to-digital converter connected to an MSP430F5529 microcontroller running at 12 MHz. The given system can sample at a rate of 500 Hz.[392] demonstrated a four-channel EEG acquisition system that was relatively small. Researchers developed a BCI board using an ADS1299 ADC linked up using an Atmega328 microcontroller based on OpenBCI project principles [393]. The EEG data was transferred to the back-end through Bluetooth. [394] describes

the development and use of a 16-channel EEG recording system using dry electrodes and a Bluetooth connection link for final processing.

7.5.1 Topology of the Framework

Designing a durable with high-accuracy analog front-end (AFE) is challenging. Because whole-brain EEG rhythmic waves propagate in the low-frequency range of 0.5–100 Hz, a high-sampling capability is unnecessary for ADC selection. However, priority should be given to analog front-ends with the most supported channels, high acquisition resolution, and noise reduction capabilities. For modular design due to low power consumption, reduced input-referred noise (0.205µVrms–6.5µVrms), and overall improvement over offered characteristics in the same device category, The ADS series was suggested for EEG acquisitions based on the assessment supplied literature. Because of its characteristics, widespread use in the industry, and diverse applications, the ADS1299 and its counterpart, the ADS1298, may be used as the analog front end for the design. The ADS1298/9 is a device with eight low-noise, programmable gain amplifiers (PGAs) and eight high 24-bit resolution Delta-Sigma ADCs for biopotential studies and medical instruments (e.g., ECG, EMG, and EEG). Self-test, temperature, and lead-off detection systems are all included in the IC.

7.5.2 Schematic modular design and PCB Layout

At the component level, a circuit diagram describes your electronic system. Components can be represented as discrete blocks with input outputs in a circuit design or standard component symbols. Complex devices, like logic gates, are presented as blocks to avoid defining every transistor and a passive element. This makes it simple to show connections between passive parts, ICs, and other circuit design elements, such as connectors. A circuit schematic and a block diagram are sometimes used interchangeably; however, they do not convey the same information. A block diagram is the starting point for your PCB design. The block diagram depicts how the system

functions from a functional standpoint. The term practical perspective refers to the functions in the system that alter data and analog signals. Each component of the system is labeled according to the role it serves. The idea is to concentrate less on individual members and more on the overall operation of the system. It's worth noting that a block diagram can relate to components while maintaining focus on the system's functioning. PCB design might take longer if the transition from the conceptual requirement to the actual design is not adequately planned. There are several aspects to consider at the same time. For instance, where should important components be placed to maximize space and performance dropped first. We also have to think about how subsystems work together and which location would produce the most evident traces. These early selections might be intimidating, resulting in procrastination or the need to restart.

Modular schematics can save time if hardware redesign is necessary for MCU migration. It might be difficult to replace an outdated microcontroller with a new one if the two are not pin compatible. The microcontroller cannot be changed until all other components have been physically relocated and all connections have been reconnected. A modular schematic design is a significantly superior solution since it allows us to organize the microcontroller on single schematic sheets and connect it to other modules through nets or ports. We would need to change the microcontroller schematic module with this method, and this is far more efficient and neater than non-modularized schematics. The schematic design shown in Figure 7.2 is completed using Altium Designer software.

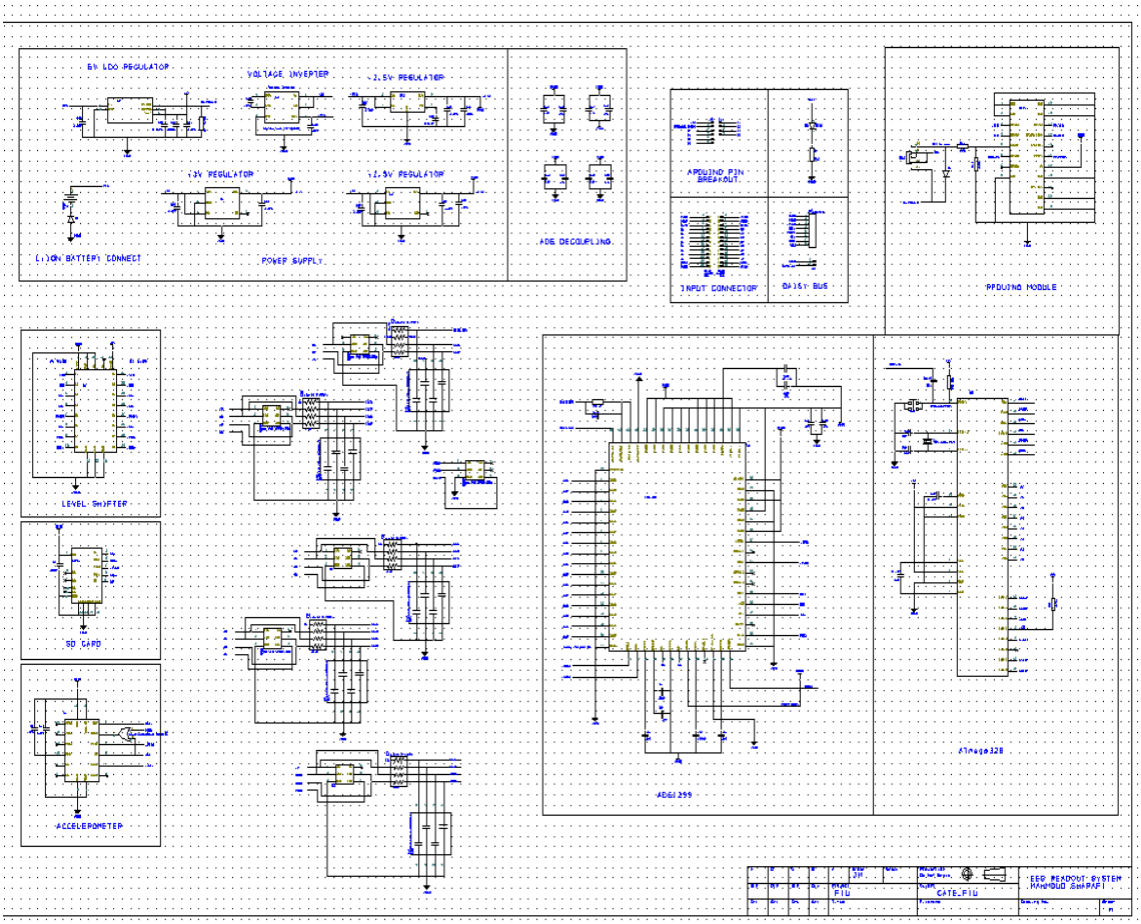

Figure 7.2 schematic design of suggested EEG recording front end system

Next, the schematic must be checked for any design rule breaches that prevent synchronization with the PCB layout. After the PCB layout is finished, this initial synchronization process ensures that any schematic changes may be instantly imported into the PCB layout. The board must then be imported into a blank PCB layout using the schematic capture tool. For the PCB, we create a layer stack, and we can arrange components and route traces between them once we've finished these three procedures. Altium Designer has several valuable features that help us construct an error-free PCB design. It allowed us to rapidly validate the layout against our design rules and restrictions, establish the layer stack fast, execute design simulations, etc. The integrated design capabilities in Altium Designer are designed to keep the PCB schematic and layout synced

without the need for an additional schematic capture application, resulting in a more efficient schematic to circuit board process. The schematic method can be transferred to a four-layer PCB using the design rules, as shown in figure 7.3.

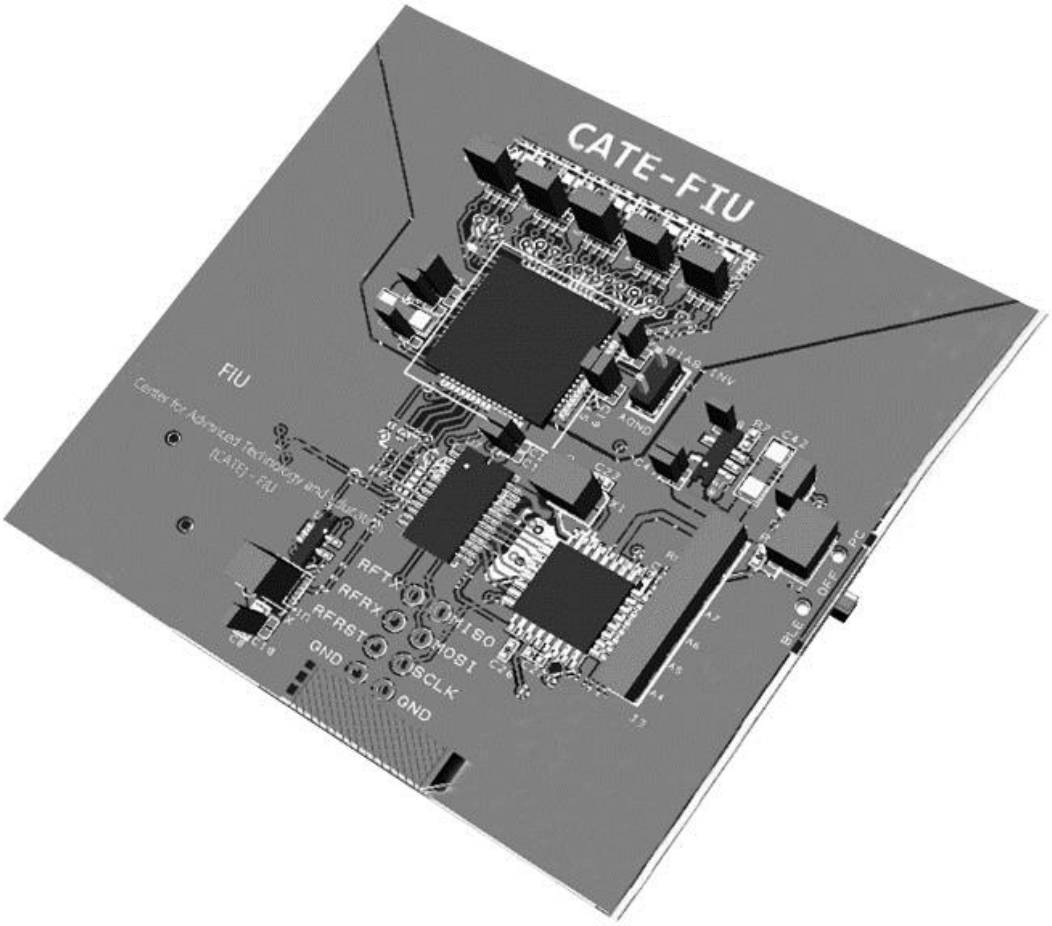

Figure 7.3. PCB of suggested EEG recording system's front end stimulated using Altium designer software

Chapter VIII: Conclusion

This dissertation, whose findings are published in high-quartile journals and in well-known conference venues, dwelved on developing a system and related circuitry for high-performance wireless power and data transmission to wearable biomedical readout devices.

The first chapter provided an investigation through the literature review on design processes of completely untethered EEG readout system applications. In the reported literature, there has been a lot of discussion on the progress of portable EEG equipment. Their performance has proven to be equivalent to traditional EEG devices for various applications. The ability to monitor mobile patients and the rapid setup time are two of its key advantages over conventional systems. We went over the various modalities and design principles in Chapter I, and an EEG cap based on the traditional 10/10 system is designed and constructed in Chapter II. The cap was created as part of a daily consumer need product design for a BCI EEG acquisition headset. Such a device would have excellent performance with a few channels, resist minor misalignment caused by non-professional users, and be tolerant of shaky contact between the electrode points and the user's head.

The design's goal was to develop a fully untethered and self-powered system. The system was built with using 3-D printing. For nonprofessional users, this degree of reliability is sufficient. It is also demonstrated that average performance can be maintained by reducing the number of channels to 16. Even if the positioning of such a headset requires greater precision, it is nevertheless an appealing solution for low-cost devices.

The third chapter focused on several strategies, including multi-resonator power transfer, intelligent power feeding, closed-loop power transmission, and high-efficiency power management, which may considerably boost the PTE of power transfer links. The proposed powering system has been fabricated, and data transfer mechanisms have been tested in the lab to prove the feasibility of the proposed design.

Such strategies have been coupled in a modular printed circuit board (PCB) design to evaluate further the practicality of the power and data transmission systems. Active electrodes, a relatively novel approach incorporating the needed bio amplifier circuitry at the electrode site, were described in Chapter IV. Improved signal integrity, decreased physical size, and a possible

reduction in power usage are deemed critical advantages over traditional electrode arrangements. They're especially well-suited towards portable EEG devices.

A preamplifier for an AE was simulated and tested at the system level in a single-channel EEG application. The application imposed several design constraints, focusing on signal integrity and power consumption. Additional design criteria were acquired from EEG recording system specifications and cutting-edge designs. In Chapter V, the components of EEG front-end electronics, such as filter core amplifiers, ADCs, and microcontrollers, were carefully studied.

8.1 Design Contributions

The following developments are considered as contributions made through this research work:

- This research developed a fully battery-less and wireless (untethered) EEG readout cap. A CAD model of a 3-D view of the EEG head cap is designed and constructed with a hexagonal form electrode holder, including holes and interconnections with elastic printing elements to meet the design requirements. As a result, this construction represents a new version of the 3-D printed EEG cap, which augments prior work. The design and fabrication of the EEG cap includes power resonators and other control circuitry and devices.

- The structural strength is determined by mechanical and electrical testing. The early designs are based on open-source BCI's base 3-D printing file, and we changed the structure to suit our needs The powering system is equipped with a highly efficient and compact power transmitter mosaicked by an array of 8×11 Tx resonators in a certain pattern operating at the lowest ISM band of 6.78 MHz. The front-end’s power receiver block Rx includes multi-resonators mounted all-around an EEG cap that can be worn by a subject.

Furthermore, considering the subject's head which could assume different positions, a well-designed positioning system and an intelligent feeding setup are developed to balance the efficiency drop due to misalignment and to involve the most associated resonators with the powering scenario with the potential of switching off the extraneous resonators that are not engaged with Transmit and Receive (Tx-Rx) power.

- A wireless misalignment-resistant powering system for a portable wireless EEG recording cap is proposed. This design can be used for the wireless recording of EEG data. A design that can also be used as an ambulatory device, or as a fast-diagnostic tool for assessing brain signals and related connectivity patterns pre and post treatment. This setup helps to increase safety precautions and reduce the negative impact of excessive magnetic field exposure in a remotely powered EEG cap. The proposed setup reduces the negative impact of angular and lateral misalignment and maintains the power link's PTE above 80% as the results indicate.

- Except for the design of the electrodes themselves as this is beyond the scope of this dissertation, All the essential elements, and supporting circuitry for designing a highly efficient power generation, transmission, and conversion chain system, PGTCC, to power up the front-end's electronics that acquire satisfactory EEG signal acquisition in a portable wireless and battery-free EEG cap. Unique configurations have been presented, including, a highly efficient and compact resonance-inductive link, multi-resonator power transfer, use of magnetized materials to improve power transmission efficiency, closed-loop power transmission, and a highly efficient power conversion chain. Experimental evaluations have shown the potential to significantly improve the total efficiency and supply stable

power for the front-end units that include the EEG signal, filtering, noise cancelation amplification units, processing units, and transceivers.

- For the first time, the design equations for an array of rectangular slots axially placed on a cylindrical waveguide are driven and presented, making it possible to attain asymmetrical and non-broadside patterns with higher bandwidths. The method of least squares is then used for both the radiation pattern synthesis with the specified side lobe level and the array input impedance matching. For optimization, the error function comprised of the three terms of impedance matching, array pattern synthesis, and slot design equations is constructed. To minimize the error function, the genetic algorithm combined with the conjugate gradient method is utilized and the geometrical characteristic of the slots defined. This procedure increases the design speed and provides the means to synthesize any desired pattern for an array of axial rectangular slots on a cylindrical waveguide. Numerical and fabrication examples are presented as illustrations of the proposed synthesis method. The results of the proposed method are verified by using the commercial software High-Frequency Structure Simulator (HFSS) in comparison to measurement results obtained out of the proposed prototype of a fabricated antenna operating at the frequency of 9 GHz.

- The research on array of rectangular slots axially placed on a cylindrical waveguide expanded on the method of least squares for the synthesis of axial slot array on a cylindrical waveguide for the dominant mode TE_{11} and analyzed the radiation from axial slots on a cylindrical waveguide. Using Elliott's method as a baseline, and for the first time, the design equations were presented and expanded for the traveling wave mode with the use of equivalent circuits for axial slot array antenna. Subsequently, the geometrical dimensions of the slot array on the cylindrical surface were determined by minimizing the

appropriate error functions. This minimization led to accurate pattern synthesis impedance matching, formulation of the relevant design equations, and minimization of power losses. With the proposed antenna design, the computational requirements were optimized. The method is also advantageous because it combines the determination of slots' parameters and impedance matching with the array pattern synthesis, leading to a quick design with higher accuracy. Moreover, a design example was presented to demonstrate the effectiveness of the proposed synthesis method on a cylindrical slot array. Full-wave simulation software HFSS was used to verify the proposed design procedure. To verify the accuracy and the practical feasibility of the simulation, measurements were taken on a prototype design of an array of axial slots on a cylindrical waveguide, and good correspondence with the theoretical predictions was achieved.

8.2 Retrospective

In retrospect, all the proposed designs including the 3D EEG headcap, the (20*1) circular power combiner, the powering resonator array, the testbed to evaluate the coupling distance effect on power transfer efficiency, the 22- rectangular slot array on a cylindrical waveguide (two rows of 11 elements) were fabricated and tested. In terms electronic circuitry for the Tx resonator driver electronics, resonant inductive link, Circuit model of Tx-Rx powering link, powering set up for wireless and battery-free EEG reading devices, Circuit model of suggested octagonal shape Tx-Rx resonators, the front and back-end circuitry for the powering units were all tested and simulated using Spice, Altium, and high-frequency structure simulator (HFSS) software.

The fully integrated head cap to be ultimately fabricated would require the inclusion of select and most performing active electrodes available on the market to be embedded in tha allotted slots in the fabricated 3D headcap. Moreover due to current fabrication facility limitations, the ultimate design will need miniaturization of some of the design elements developed in this dissertation. This is by no means an easy task as other technological limits could be confronted as we attempt to integrate all these softwrae-based and the hardware-based components. Only then will we be able to ascertain the full practical dimension and of the proposed wirelees and batteryless EEG recording system

List of References

[1] R. Caton, “Electrical Currents of the Brain,” The Journal of Nervous and Mental Disease, vol. 2, no. 4, p. 610, 1875.

[2] H. Berger, “Uber das Elektrenkephalogramm des Menschen, 2nd report”, J Psychol Neurol (Leipzig), vol. 40, no. 87, pp. 160–179, 1930.

[3] N. Ernst and F. Lopes da Silva, Electroencephalography: Basic Principles, Clinical Applications, and Related Fields, 5th. Philadelphia: Lippincott Williams & Wilkins, 2005, ISBN: 07817512.

[4] N. N. Boutros, Standard EEG: A Research Roadmap for Neuropsychiatry. Kansas, MO: Springer International, 2013.

[5] B. Burle, L. Spieser, C. Roger, L. Casini, T. Hasbroucq, and F. Vidal, “Spatial and temporal resolutions of EEG: Is it black and white, A scalp current density view,” Intl. Journal of Psychophysiology, vol. 97, no. 3, pp. 210–220, 2015.

[6] R. Maskeliunas, R. Damasevicius, I. Martisius, and M. Vasiljevas, “Consumer-grade EEG devices: are they usable for control tasks,” PeerJ, vol. 4, 2016. DOI: 10.7717/peerj.1746.

[7] Karimi-Bidhendi et al., “CMOS Ultralow Power Brain Signal Acquisition Front-Ends: Design and Human Testing,” IEEE Transactions on Biomedical Circuits and Systems, vol. 11, no. 5, 2017.

[8] K. Ullah, M. Ali, M. Rizwan, and M. Imran, “Low-cost single-channel EEG based communication system for people with lock-in syndrome,” Proceedings of the 14th IEEE International Multitopic Conference 2011, INMIC 2011, pp. 120–125, 2011.

[9]] C. J. Chu, “High-density EEG-What do we have to lose,” Clinical Neurophysiology, vol. 126 (3), pp. 433–434, 2015.

[10] S. Beniczky, A.A. Arbune, J. Jeppesen, P. Ryvlin, “Biomarkers of seizure severity derived from wearable devices,” Epilepsia, DOI: 10.1111/epi.16492, Early access June 2020.

[11] E. Bruno, P.F. Viana, M.R. Sperling, MR M.P. Richardson, “Seizure detection at home: Do devices on the market match the needs of people living with epilepsy and their caregivers?” Epilepsia, Early Access: MAY 2020.

[12] F. Chen, A.P. Chandrakasan, V.M. Stojanovic, “Design and Analysis of a Hardware-Efficient Compressed Sensing Architecture for Data Compression in Wireless Sensors,” IEEE Journal of Solid-State Circuits, Vol. 47 (3), pp. 744-756, March 2012.

[13] N. Verma, A. Shoeb, J. Bohorquez, J. Dawson, J. Guttag, A.P. Chandrakasan, “A Micro-Power EEG Acquisition SoC With Integrated Feature Extraction Processor for a Chronic Seizure Detection System,” IEEE Journal of Solid-State Circuits, Vol. 45 (4), pp. 804-816, April 2010.

[14] T.R. Mullen, C.A.E. Kothe, Y.M. Chi, A. Ojeda, T. Kerth, S. Makeig, T.P. Jung, G. Cauwenberghs, “Real-Time Neuroimaging and Cognitive Monitoring Using Wearable Dry EEG,” IEEE Transactions on Biomedical Engineering, Vol. 62 (11), pp. 2553-2567, November 2015.

[15] J. Xu, R. F. Yazicioglu, B. Grundlehner, P. Harpe, K. A. A. Makinwa, and C. Van Hoof, “A 160 mW 8-channel active electrode system for EEG monitoring”, IEEE Trans. on Biomedical Circuits and Systems, vol. 5, no. 6, pp. 555–567, 2011.

[16] T. Degen and H. Jäckel, “A pseudo-differential amplifier for bioelectric events with DC-offset compensation using two-wired amplifying electrodes,” IEEE Transactions on Biomedical Engineering, vol. 53, no. 2, pp. 300–310, 2006.

[17] Soufineyestani, Mahsa, Dale Dowling, and Arshia Khan. "Electroencephalography (EEG) technology applications and available devices." Applied Sciences 10.21 (2020): 7453.

[18] Kim, Jeehoon, et al. "An instant donning multi-channel EEG headset (with comb-shaped dry electrodes) and BCI applications." Sensors 19.7 (2019): 1537.

[19] Oostenveld, Robert, and Peter Praamstra. "The five percent electrode system for high-resolution EEG and ERP measurements." Clinical Neurophysiology 112.4 (2001): 713-719.

[20] Seeck, Margitta, et al. "The standardized EEG electrode array of the IFCN." Clinical Neurophysiology 128.10 (2017): 2070-2077.

[21] Homan, Richard W. "The 10-20 electrode system and cerebral location." American Journal of EEG Technology 28.4 (1988): 269-279.

[22] Krigolson, Olave E., et al. "Choosing MUSE: Validation of a low-cost, portable EEG system for ERP research." Frontiers in neuroscience 11 (2017): 109.

[23] Teplan, Michal. "Fundamentals of EEG measurement." Measurement science review 2.2 (2002): 1-11.

[24] Thompson, Trevor, et al. "EEG applications for sport and performance." Methods 45.4 (2008): 279-288.

[25] Lacko, Daniël, et al. "Ergonomic design of an EEG headset using 3D anthropometry." Applied ergonomics 58 (2017): 128-136.

[26] OpenBCI, Inc. (2021). Retrieved from https://docs.openbci.com/AddOns/Headwear/MarkIV/.

[27] Debener, Stefan, et al. "How about taking a low-cost, small, and wireless EEG for a walk?" Psychophysiology 49.11 (2012): 1617-1621.

[28] Mihajlović, Vojkan, et al. "Wearable, wireless EEG solutions in daily life applications: what are we missing?." IEEE journal of biomedical and health informatics 19.1 (2014): 6-21.

[29] Ratti, Elena, et al. "Comparison of medical and consumer wireless EEG systems for use in clinical trials." Frontiers in human neuroscience 11 (2017): 398.

[30] Bertrand, Alexander. "Distributed signal processing for wireless EEG sensor networks." IEEE Transactions on Neural Systems and Rehabilitation Engineering 23.6 (2015): 923-935.

[31] Kam, Julia WY, et al. "Systematic comparison between a wireless EEG system with dry electrodes and a wired EEG system with wet electrodes." NeuroImage 184 (2019): 119-129.

[32] Rogers, Jeffrey M., et al. "Test-retest reliability of a single-channel, wireless EEG system." International Journal of Psychophysiology 106 (2016): 87-96.

[33] Matthews, R., et al. "Real time workload classification from an ambulatory wireless EEG system using hybrid EEG electrodes." 2008 30th Annual International Conference of the IEEE Engineering in Medicine and Biology Society. IEEE, 2008.

[34] Grant, Arthur C., et al. "Diagnostic accuracy of microEEG: a miniature, wireless EEG device." Epilepsy & Behavior 34 (2014): 81-85.

[35] Khan, Sadeque Reza, et al. "Wireless power transfer techniques for implantable medical devices: A review." Sensors 20.12 (2020): 3487.

[36] Kiani, Mehdi, Uei-Ming Jow, and Maysam Ghovanloo. "Design and optimization of a 3-coil inductive link for efficient wireless power transmission." IEEE transactions on biomedical circuits and systems 5.6 (2011): 579-591.

[37] Kim, Jin-Wook, et al. "Analysis of wireless energy transfer to multiple devices using CMT." 2010 Asia-Pacific Microwave Conference. IEEE, 2010.

[38] Kiani, Mehdi, and Maysam Ghovanloo. "A figure-of-merit for designing high-performance inductive power transmission links." IEEE transactions on industrial electronics 60.11 (2012): 5292-5305.

[39] Hui, Shu Yuen Ron, Wenxing Zhong, and Chi Kwan Lee. "A critical review of recent progress in mid-range wireless power transfer." IEEE Transactions on Power Electronics 29.9 (2013): 4500-4511.

[40] Kiani, Mehdi, and Maysam Ghovanloo. "The circuit theory behind coupled-mode magnetic resonance-based wireless power transmission." IEEE Transactions on Circuits and Systems I: Regular Papers 59.9 (2012): 2065-2074.

[41] Agarwal, Kush, et al. "Wireless power transfer strategies for implantable bioelectronics." IEEE reviews in biomedical engineering 10 (2017): 136-161.

[42] Barman, Surajit Das, et al. "Wireless powering by magnetic resonant coupling: Recent trends in wireless power transfer system and its applications." Renewable and Sustainable energy reviews 51 (2015): 1525-1552.

[43] A. Kurs, A. Karalis, R. Moffatt, J. D. Joannopoulos, P. Fisher and M. Soljai, "Wireless power transfer via strongly coupled magnetic resonances", Science, vol. 317, no. 5834, pp. 83-86, 2007.

[44] Kim, Han-Joon, et al. "Review of near-field wireless power and communication for biomedical applications." IEEE Access 5 (2017): 21264-21285.

[45] Bou Balust, Elisenda, Eduardo José Alarcón Cot, and Jordi Gutiérrez Cabello. "A comparison of analytical models for resonant inductive coupling wireless power transfer." PIERS 2012: Progress in Electromagnetics Research Symposium: proceedings: Moscow, Russia: August 19-23, 2012. The Electromagnetics Academy, 2012.

[46] Vinge, Rikard. Wireless energy transfer by resonant inductive coupling. MS thesis. 2015.

[47] Samal, Satish K., et al. "Analysis of the effect of design parameters on the power transfer efficiency of resonant inductive coupling based wireless EV charging system." 2017 Innovations in Power and Advanced Computing Technologies (i-PACT). IEEE, 2017.

[48] Tseng, Victor Farm-Guoo, and Huikai Xie. "Resonant inductive coupling-based piston position sensing mechanism for large vertical displacement micromirrors." Journal of Microelectromechanical Systems 25.1 (2015): 207-216.

[49] Xue, Rui-Feng, Kuang-Wei Cheng, and Minkyu Je. "High-efficiency wireless power transfer for biomedical implants by optimal resonant load transformation." IEEE Transactions on Circuits and Systems I: Regular Papers 60.4 (2012): 867-874.

[50] Psenakova, Zuzana, Mariana Benova, and Jana Mydlova. "Investigation of SAR (Specific absorbtion rate) in different head models placed in shielded space." 2019 IEEE 20th International Conference on Computational Problems of Electrical Engineering (CPEE). IEEE, 2019.

[51] Brown, Lindsay, et al. "A low-power, wireless, 8-channel EEG monitoring headset." 2010 Annual International Conference of the IEEE Engineering in Medicine and Biology. IEEE, 2010.

[52] Casson, Alexander J. "Wearable EEG and beyond." Biomedical engineering letters 9.1 (2019): 53-71.

[53] Kassab, Ali, et al. Multichannel wearable f NIRS-EEG system for long-term clinical monitoring. Vol. 39. No. 1. 2018.

[54] Wang, Qiang, Olga Sourina, and Minh Khoa Nguyen. "EEG-based" serious" games design for medical applications." 2010 international conference on cyberworlds. IEEE, 2010.

[55] Seo, Dong-Wook, Jae-Ho Lee, and Hyung-Soo Lee. "Optimal coupling to achieve maximum output power in a WPT system." IEEE Transactions on Power Electronics 31.6 (2015): 3994-3998.

[56] Divakaran, Sleebi K., and Deepti Das Krishna. "RF energy harvesting systems: An overview and design issues." International Journal of RF and Microwave Computer-Aided Engineering 29.1 (2019): e21633.

[57] Valenta, Christopher R., and Gregory D. Durgin. "Harvesting wireless power: Survey of energy-harvester conversion efficiency in far-field, wireless power transfer systems." IEEE Microwave Magazine 15.4 (2014): 108-120.

[58] Shinohara, Naoki. "Trends in wireless power transfer: WPT technology for energy harvesting, mllimeter-wave/THz rectennas, MIMO-WPT, and advances in near-field WPT applications." IEEE Microwave Magazine 22.1 (2020): 46-59.

[59] Cai, Changsong, et al. "Improved coplanar couplers based WPT systems for adaptive energy harvesting on power towers." IEEE Transactions on Electromagnetic Compatibility 63.3 (2020): 922-934.

[60] Qahouq, Jaber A. Abu, and Zhigang Dang. "Investigation and simulation model results of high-density wireless power harvesting and transfer method." 2017 IEEE Applied Power Electronics Conference and Exposition (APEC). IEEE, 2017.

[61] Kang, Seok Hyon, et al. "Magnetic resonant three-coil WPT system between off/in-body for remote energy harvest." IEEE Microwave and Wireless Components Letters 26.9 (2016): 741-743.

[62] Alberto, José, et al. "Fully untethered battery-free biomonitoring electronic tattoo with wireless energy harvesting." Scientific reports 10.1 (2020): 1-11.

[63] Xia, Qingfeng, and Longyang Yan. "Application of wireless power transfer technologies and intermittent energy harvesting for wireless sensors in rotating machines." Wireless Power Transfer 3.2 (2016): 93-104.

[64] Bhatti, Naveed Anwar, et al. "Energy harvesting and wireless transfer in sensor network applications: Concepts and experiences." ACM Transactions on Sensor Networks (TOSN) 12.3 (2016): 1-40.

[65] Shinohara, Naoki. "The wireless power transmission: inductive coupling, radio wave, and resonance coupling." Wiley Interdisciplinary Reviews: Energy and Environment 1.3 (2012): 337-346.

[66] Lazaro, Antonio, et al. "Study on the reading of energy-harvested implanted NFC tags using mobile phones." IEEE Access 8 (2019): 2200-2221.

[67] Masouleh, Mahmoud Sharafi, Amin Kargar Behbahani, and Malek Adjouadi. "Design, Analysis, and Optimization of the Array of Axial Rectangular Slots on a Cylindrical Waveguide." IEEE Access 9 (2021): 98218-98230.

[68] Masouleh, Mahmoud Sharafi, and Amin Kargar Behbahani. "Optimum design of the array of circumferential slots on a cylindrical waveguide." AEU-International Journal of Electronics and Communications 70.5 (2016): 578-583.

[69] Oraizi, Homayoon, et al. "Optimum design of travelling rectangular waveguide edge slot array with non-uniform spacing." IET microwaves, antennas & propagation 7.7 (2013): 575-581.

[70] Aboualalaa, Mohamed, et al. "Design of a dual-band microstrip antenna with enhanced gain for energy harvesting applications." IEEE Antennas and Wireless Propagation Letters 16 (2017): 1622-1626.

[71] Wang, Xiaoyu. High Efficiency and High Sensitivity Wireless Power Transfer and Wireless Power Harvesting Systems. Diss. 2016.

[72] Charthad, Jayant, et al. "System-level analysis of far-field radio frequency power delivery for mm-sized sensor nodes." IEEE Transactions on Circuits and Systems I: Regular Papers 63.2 (2016): 300-311.

[73] Belo, Daniel, et al. "A selective, tracking, and power adaptive far-field wireless power transfer system." IEEE Transactions on Microwave Theory and Techniques 67.9 (2019): 3856-3866.

[74] Le, Triet, Karti Mayaram, and Terri Fiez. "Efficient far-field radio frequency energy harvesting for passively powered sensor networks." IEEE Journal of solid-state circuits 43.5 (2008): 1287-1302.

[75] Sarin, Akshay, Xiaofan Cui, and Al-Thaddeus Avestruz. "Comparison of switched receivers for direct-sequence spread-spectrum wireless power transfer." 2017 IEEE 18th Workshop on Control and Modeling for Power Electronics (COMPEL). IEEE, 2017.

[76] Sun, Hucheng, et al. "A dual-band rectenna using broadband Yagi antenna array for ambient RF power harvesting." IEEE Antennas and Wireless Propagation Letters 12 (2013): 918-921.

[77] Ferreira, David, et al. "Hybrid FSS and rectenna design for wireless power harvesting." IEEE Transactions on Antennas and Propagation 64.5 (2016): 2038-2042.

[78] Zhang, Xuanming, and Long Li. "A dual-band polarization-independent and wide-angle metasurface for electromagnetic power harvesting." 2017 Sixth Asia-Pacific Conference on Antennas and Propagation (APCAP). IEEE, 2017.

[79] Mhatre, Pratik, et al. "RF power harvesting system for RFID applications in multiband systems." 2015 6th International Conference on Computing, Communication and Networking Technologies (ICCCNT). IEEE, 2015.

[80] Takhedmit, Hakim. "Ambient RF power harvesting: Application to remote supply of a batteryless temperature sensor." 2016 IEEE international smart cities conference (ISC2). IEEE, 2016.

[81] Chen, Yen-Sheng, Fei-Peng Lai, and Jing-Wei You. "Analysis of antenna radiation characteristics using a hybrid ray tracing algorithm for indoor WiFi energy-harvesting rectennas." IEEE Access 7 (2019): 38833-38846.

[82] Ishak, Mohamad Hafis Izran. "Review of safety evaluation of thermal wearable power harvesting device." International Journal of Integrated Engineering 9.4 (2017).

[83] Nelson, Carl A., et al. "Power harvesting for railroad track safety enhancement using vertical track displacement." Active and Passive Smart Structures and Integrated Systems 2009. Vol. 7288. International Society for Optics and Photonics, 2009.

[84] Rahmani, Hamed, and Aydin Babakhani. "A dual-mode RF power harvesting system with an on-chip coil in 180-nm SOI CMOS for millimeter-sized biomedical implants." IEEE Transactions on Microwave Theory and Techniques 67.1 (2018): 414-428.

[85] Sauer, Christian, et al. "Power harvesting and telemetry in CMOS for implanted devices." IEEE Transactions on Circuits and Systems I: Regular Papers 52.12 (2005): 2605-2613.

[86] Pourghodrat, Abolfazl, et al. "Improving an energy harvesting device for railroad safety applications." Active and Passive Smart Structures and Integrated Systems 2011. Vol. 7977. International Society for Optics and Photonics, 2011.

[87] Ho, John S., et al. "Wireless power transfer to deep-tissue microimplants." Proceedings of the National Academy of Sciences 111.22 (2014): 7974-7979.

[88] Imran, Muhammad, et al. "Energy harvesting in 5G networks: Taxonomy, requirements, challenges, and future directions." arXiv preprint arXiv:1910.00785 (2019).

[89] Azam, SM Kayser, et al. "Monopole antenna on transparent substrate and rectifier for energy harvesting applications in 5G." International Journal of Advanced Computer Science and Applications 11.8 (2020): 84-89.

[90] Iannacci, Jacopo. "Internet of things (IoT); internet of everything (IoE); tactile internet; 5G–A (not so evanescent) unifying vision empowered by EH-MEMS (energy harvesting MEMS) and RF-MEMS (radio frequency MEMS)." Sensors and actuators a: physical 272 (2018): 187-198.

[91] Coleman, Cristopher, and Heath Yardley. "DAB based passive radar: Performance calculations and trials." 2008 International Conference on Radar. IEEE, 2008.

[92] Togo, Hiroyoshi, Naofumi Shimizu, and Tadao Nagatsuma. "Near-field mapping system using fiber-based electro-optic probe for specific absorption rate measurement." IEICE transactions on electronics 90.2 (2007): 436-442.

[93] Bernardi, Paolo, et al. "Specific absorption rate and temperature elevation in a subject exposed in the far-field of radio-frequency sources operating in the 10-900-MHz range." IEEE Transactions on biomedical engineering 50.3 (2003): 295-304.

[94] Hochwald, Bertrand M., et al. "Incorporating specific absorption rate constraints into wireless signal design." IEEE Communications Magazine 52.9 (2014): 126-133.

[95] McCoy, Danny O., Deanna M. Zakharia, and Quirino Balzano. "Field strengths and specific absorption rates in automotive environments." IEEE transactions on vehicular technology 48.4 (1999): 1287-1303.

[96] Fang, Xiao Sheng, and Kwok Wa Leung. "Linear-/circular-polarization designs of dual-/wide-band cylindrical dielectric resonator antennas." IEEE Transactions on Antennas and Propagation 60.6 (2012): 2662-2671.

[97] Tran, Huy Hung, Nghia Nguyen-Trong, and Amin M. Abbosh. "Simple design procedure of a broadband circularly polarized slot monopole antenna assisted by characteristic mode analysis." IEEE access 6 (2018): 78386-78393.

[98] Abdullah, Mujeeb, Saad Hassan Kiani, and Amjad Iqbal. "Eight element multiple-input multiple-output (MIMO) antenna for 5G mobile applications." IEEE Access 7 (2019): 134488-134495.

[99] Xu, Rui, Jian-Ying Li, and Jie Liu. "A design of broadband circularly polarized C-shaped slot antenna with sword-shaped radiator and its array for L/S-band applications." IEEE Access 6 (2017): 5891-5896.

[100] Shamsinejad, Souren, et al. "Pattern reconfigurable cubic slot antenna." IEEE Access 7 (2019): 64401-64410.

[101] Li, Y. J., Z. Y. Lu, and L. S. Yang. "CPW-fed slot antenna for medical wearable applications." IEEE Access 7 (2019): 42107-42112.

[102] Xu, Rui, et al. "A design of U-shaped slot antenna with broadband dual circularly polarized radiation." IEEE Transactions on Antennas and Propagation 65.6 (2017): 3217-3220.

[103] Chen, Zhijiao, et al. "High gain, broadband and dual-polarized substrate integrated waveguide cavity-backed slot antenna array for 60 GHz band." IEEE Access 6 (2018): 31012-31022.

[104] Yuan, Weile, et al. "Rectangular grating waveguide slot array antenna for SATCOM applications." IEEE Transactions on Antennas and Propagation 67.6 (2019): 3869-3880.

[105] Jia, Yongtao, et al. "In-band radar cross section reduction of slot array antenna." IEEE Access 6 (2018): 23561-23567.

[106] Koli, Mst Nishat Yasmin, et al. "An all-metal high-gain radial-line slot-array antenna for low-cost satellite communication systems." IEEE Access 8 (2020): 139422-139432.

[107] Lian, Ruina, et al. "Design of a low-profile dual-polarized stepped slot antenna array for base station." IEEE Antennas and Wireless Propagation Letters 15 (2015): 362-365.

[108] Oraizi, Homayoon, and Mahmoud T. Noghani. "Design and optimization of waveguide-fed centered inclined slot arrays." IEEE transactions on antennas and propagation 57.12 (2009): 3993-3997.

[109] Stevenson, A. F. "Theory of slots in rectangular wave-guides." Journal of Applied physics 19.1 (1948): 24-38.

[110] Oliner, A. "The impedance properties of narrow radiating slots in the broad face of rectangular waveguide: Part I--Theory." IRE Transactions on Antennas and Propagation 5.1 (1957): 4-11.

[111] R. S. Elliott, “Antenna Theory and Design,” Prentice-Hall, Upper Saddle River, NJ, 2003.

[112] Oraizi, Homayoon, et al. "Optimum design of travelling rectangular waveguide edge slot array with non-uniform spacing." IET microwaves, antennas & propagation 7.7 (2013): 575-581.

[113] Macke, W. "JR Wait, Electromagnetic Radiation from Cylindrical Structures. IX+ 200 S. m. Abb. London 1959. Pergamon Press. Preis geb. 50 s net." (1960): 285-285.

[114] Shin, Dong H., and Hyo J. Eom. "Radiation from narrow circumferential slots on a conducting circular cylinder." IEEE transactions on antennas and propagation 53.6 (2005): 2081-2088.

[115] Masouleh, Mahmoud Sharafi, and Amin Kargar Behbahani. "Optimum design of the array of circumferential slots on a cylindrical waveguide." AEU-International Journal of Electronics and Communications 70.5 (2016): 578-583.

[116] Khodaei, Farhad Gh, Javad Nourinia, and Changiz Ghobadi. "A practical miniaturized U-slot patch antenna with enhanced bandwidth." Progress In Electromagnetics Research B 3 (2008): 47-62.

[117] Chen, Yan-Lin, Cheng-Li Ruan, and Lin Peng. "A novel ultra-wideband bow-tie slot antenna in wireless communication systems." Progress In Electromagnetics Research Letters 1 (2008): 101-108.

[118] Hashimoto, Koh, Jiro Hirokawa, and Makoto Ando. "A post-wall waveguide center-feed parallel plate slot array antenna in the millimeter-wave band." IEEE Transactions on Antennas and Propagation 58.11 (2010): 3532-3538.

[119] Tsai, Ruenn-Bo, Kin-Lu Wong, and Hsin-Cheng Su. "Analysis of a microstrip-line-fed radiating slot on a cylindrical surface." Microwave and Optical Technology Letters 8.4 (1995): 193-196.

[120] Bailin, L. "The radiation field produced by a slot in a large circular cylinder." IRE Transactions on Antennas and Propagation 3.3 (1955): 128-137.

[121] Elliott, R. "An improved design procedure for small arrays of shunt slots." IEEE Transactions on Antennas and Propagation 31.1 (1983): 48-53.

[122] Zhong, Wenxing, Dehong Xu, and Ron Shu Yuen Hui. "Introduction to Magnetic Resonance WPT." Wireless Power Transfer. Springer, Singapore, 2020. 3-9.

[123] Mayordomo, Iker, et al. "An overview of technical challenges and advances of inductive wireless power transmission." Proceedings of the IEEE 101.6 (2013): 1302-1311.

[124] Shinohara, Naoki. "Beam efficiency of wireless power transmission via radio waves from short range to long range." Journal of electromagnetic engineering and science 10.4 (2010): 224-230.

[125] Li, Ying, and Vikram Jandhyala. "Design of retrodirective antenna arrays for short-range wireless power transmission." IEEE Transactions on Antennas and Propagation 60.1 (2011): 206-211.

[126] Dickinson, Richard M. "Wireless power transmission technology state of the art the first Bill Brown lecture." Acta Astronautica 53.4-10 (2003): 561-570.

[127] Li, Joshua Le-Wei. "Wireless power transmission: State-of-the-arts in technologies and potential applications." Asia-Pacific Microwave Conference 2011. IEEE, 2011.

[128] Basar, Md Rubel, et al. "Application of wireless power transmission systems in wireless capsule endoscopy: An overview." Sensors 14.6 (2014): 10929-10951.

[129] Mahmood, A., et al. "A comparative study of wireless power transmission techniques." Journal of Basic and Applied Scientific Research 4.1 (2014): 321-326.

[130] Tomar, Anuradha, and Sunil Gupta. "Wireless power transmission: Applications and components." International Journal of Engineering 1.5 (2012): 1-8.

[131] Carvalho, Nuno Borges, et al. "Wireless power transmission: R&D activities within Europe." IEEE Transactions on Microwave Theory and Techniques 62.4 (2014): 1031-1045.

[132] Ibrahim, Ahmed, Miao Meng, and Mehdi Kiani. "A comprehensive comparative study on inductive and ultrasonic wireless power transmission to biomedical implants." IEEE sensors journal 18.9 (2018): 3813-3826.

[133] Collado, Ana, and Apostolos Georgiadis. "Optimal waveforms for efficient wireless power transmission." IEEE microwave and wireless components letters 24.5 (2014): 354-356.

[134] Jung, K. H., et al. "Wireless power transmission for implantable devices using inductive component of closed magnetic circuit." Electronics letters 45.1 (2008): 21-22.

[135] Sasaki, Susumu, and Koji Tanaka. "Wireless power transmission technologies for solar power satellite." 2011 IEEE MTT-S International Microwave Workshop Series on Innovative Wireless Power Transmission: Technologies, Systems, and Applications. IEEE, 2011.

[136] Aoki, Takumi, et al. "Maximum transfer efficiency of MIMO-WPT system." 2018 IEEE Wireless Power Transfer Conference (WPTC). IEEE, 2018.

[137] Lee, Hoon Hee, Seok Hyon Kang, and Chang Won Jung. "MR-WPT with reconfigurable resonator and ground for laptop application." IEEE Microwave and Wireless Components Letters 28.3 (2018): 269-271.

[138] Fu, Wenzhen, Bo Zhang, and Dongyuan Qiu. "Study on frequency-tracking wireless power transfer system by resonant coupling." 2009 IEEE 6th International Power Electronics and Motion Control Conference. IEEE, 2009.

[139] Kato, Masaki, Takehiro Imura, and Yoichi Hori. "Study on maximize efficiency by secondary side control using DC-DC converter in wireless power transfer via magnetic resonant coupling." World Electric Vehicle Journal 6.4 (2013): 858-862.

[140] Zhang, Zhen, et al. "Wireless power transfer-An overview." IEEE Transactions on Industrial Electronics 66.2 (2018): 1044-1058.

[141] Meng, Miao, and Mehdi Kiani. "Design and optimization of ultrasonic wireless power transmission links for millimeter-sized biomedical implants." IEEE transactions on biomedical circuits and systems 11.1 (2016): 98-107.

[142] Ibrahim, Ahmed, Miao Meng, and Mehdi Kiani. "Inductive and ultrasonic wireless power transmission to biomedical implants." 2017 IEEE International Symposium on Circuits and Systems (ISCAS). IEEE, 2017.

[143] Zhang, Jin, and Chonghu Cheng. "Analysis and optimization of three-resonator wireless power transfer system for predetermined-goals wireless power transmission." Energies 9.4 (2016): 274.

[144] Han, Yang, and Xiaoming Wang. "Calculation of mutual inductance based on field-circuit coupling analysis for WPT." 2013 5th International Conference on Power Electronics Systems and Applications (PESA). IEEE, 2013.

[145] Sonntag, C. L. W., E. A. Lomonova, and J. L. Duarte. "Implementation of the Neumann formula for calculating the mutual inductance between planar PCB inductors." 2008 18th International Conference on Electrical Machines. IEEE, 2008.

[146] Kar, Durga P., et al. "Selection of maximum power transfer region for resonant inductively coupled wireless charging system." AEU-International Journal of Electronics and Communications 84 (2018): 84-92.

[147] Ricketts, David S., Matthew J. Chabalko, and Andrew Hillenius. "Experimental demonstration of the equivalence of inductive and strongly coupled magnetic resonance wireless power transfer." Applied Physics Letters 102.5 (2013): 053904.

[148] Zhang, Jin, and Chonghu Cheng. "Quantitative investigation into the use of resonant magneto-inductive links for efficient wireless power transfer." IET Microwaves, Antennas & Propagation 10.1 (2016): 38-44.

[149] Shadid, Reem, et al. "Hybrid inductive power transfer and wireless antenna system for biomedical implanted devices." Progress In Electromagnetics Research C 88 (2018): 77.

[150] Danilov, A. A., E. A. Mindubaev, and S. V. Selishchev. "Methods for compensation of coil misalignment in systems for inductive transcutaneous power transfer to implanted medical devices." Biomedical Engineering 51.1 (2017): 56-60.

[151] Pérez-Nicoli, Pablo, Fernando Silveira, and Maysam Ghovanloo. Inductive Links for Wireless Power Transfer. Springer International Publishing, 2021.

[152] Dou, Zhifeng, et al. "Bidirectional communication in the inductive WPT system with injected information transmission." 2019 22nd International Conference on Electrical Machines and Systems (ICEMS). IEEE, 2019.

[153] Jawad, Aqeel Mahmood, et al. "Wireless Drone Charging Station Using Class-E Power Amplifier in Vertical Alignment and Lateral Misalignment Conditions." Energies 15.4 (2022): 1298.

[154] Dai, Haipeng, et al. "Quality of energy provisioning for wireless power transfer." IEEE Transactions on Parallel and Distributed Systems 26.2 (2014): 527-537.

[155] Stein, Aaron LF, Phyo Aung Kyaw, and Charles R. Sullivan. "High-Q self-resonant structure for wireless power transfer." 2017 IEEE Applied Power Electronics Conference and Exposition (APEC). IEEE, 2017.

[156] Zhang, Yiming, Zhengming Zhao, and Kainan Chen. "Frequency decrease analysis of resonant wireless power transfer." IEEE Transactions on Power Electronics 29.3 (2013): 1058-1063.

[157] Awai, Ikuo, and Takuya Komori. "A simple and versatile design method of resonator-coupled wireless power transfer system." 2010 International Conference on Communications, Circuits and Systems (ICCCAS). IEEE, 2010.

[158] Dang, Zhigang, Yuan Cao, and Jaber A. Abu Qahouq. "Reconfigurable magnetic resonance-coupled wireless power transfer system." IEEE Transactions on Power Electronics 30.11 (2015): 6057-6069.

[159] Feliziani, Mauro, et al. "Near field shielding of a wireless power transfer (WPT) current coil." Progress In Electromagnetics Research C 77 (2017): 39-48.

[160] Jeong, In-Sung, et al. "Analysis of S-Parameters in Magnetic Resonance WPT Using Superconducting Coils." IEEE Transactions on Applied Superconductivity 26.3 (2016): 1-4..

[161] Li, Siqi, and Chunting Chris Mi. "Wireless power transfer for electric vehicle applications." IEEE journal of emerging and selected topics in power electronics 3.1 (2014): 4-17.

[162] Watteyne, Thomas, et al. "OpenWSN: a standards-based low-power wireless development environment." Transactions on Emerging Telecommunications Technologies 23.5 (2012): 480-493.

[163] Van Wageningen, Dries, and Toine Staring. "The Qi wireless power standard." Proceedings of 14th International Power Electronics and Motion Control Conference EPE-PEMC 2010. IEEE, 2010.

[164] Jones, Christine E., et al. "A survey of energy efficient network protocols for wireless networks." wireless networks 7.4 (2001): 343-358.

[165] Kang, M., E. Noh, and K. Kim. "NFC transmitter coil placement to minimise degradation of A4WP wireless power transfer efficiency." Electronics Letters 53.9 (2017): 616-618.

[166] Shidujaman, Mohammad, Hooman Samani, and Mohammad Arif. "Wireless power transmission trends." 2014 International Conference on Informatics, Electronics & Vision (ICIEV). IEEE, 2014.

[167] El Rayes, Mohamed M., Gihan Nagib, and WG Ali Abdelaal. "A review on wireless power transfer." International Journal of Engineering Trends and Technology (IJETT) 40.5 (2016): 272-280.

[168] Kim, Sang-Yun, et al. "A-20 to 30 dBm input power range wireless power system with a MPPT-based reconfigurable 48% efficient RF energy harvester and 82% efficient A4WP wireless power receiver with open-loop delay compensation." IEEE Transactions on Power Electronics 34.7 (2018): 6803-6817.

[169] Tseng, Ryan, et al. "Introduction to the alliance for wireless power loosely-coupled wireless power transfer system specification version 1.0." 2013 IEEE Wireless Power Transfer (WPT). IEEE, 2013.

[170] Nikoukar, Ali, et al. "Low-power wireless for the Internet of Things: Standards and applications." IEEE Access 6 (2018): 67893-67926.

[171] Monks, Jeffrey P., Vaduvur Bharghavan, and W-MW Hwu. "A power controlled multiple access protocol for wireless packet networks." Proceedings IEEE INFOCOM 2001. Conference on Computer Communications. Twentieth Annual Joint Conference of the IEEE Computer and Communications Society (Cat. No. 01CH37213). Vol. 1. IEEE, 2001.

[172] Gungor, Vehbi C., and Gerhard P. Hancke. "Industrial wireless sensor networks: Challenges, design principles, and technical approaches." IEEE Transactions on industrial electronics 56.10 (2009): 4258-4265.

[173] Lu, Gang, Bhaskar Krishnamachari, and Cauligi S. Raghavendra. "Performance evaluation of the IEEE 802.15. 4 MAC for low-rate low-power wireless networks." IEEE International Conference on Performance, Computing, and Communications, 2004. IEEE, 2004.

[174] Arms, Steven W., et al. "Power management for energy harvesting wireless sensors." Smart Structures and Materials 2005: Smart Electronics, MEMS, BioMEMS, and Nanotechnology. Vol. 5763. International Society for Optics and Photonics, 2005.

[175] Cao, Huasong, et al. "Enabling technologies for wireless body area networks: A survey and outlook." IEEE Communications Magazine 47.12 (2009): 84-93.

[176] Fonseca, Carlos, et al. "A novel dry active electrode for EEG recording." IEEE Transactions on Biomedical Engineering 54.1 (2006): 162-165.

[177] Gargiulo, Gaetano, et al. "A new EEG recording system for passive dry electrodes." Clinical Neurophysiology 121.5 (2010): 686-693.

[178] Ludvig, Nandor, et al. "An implantable triple-function device for local drug delivery, cerebrospinal fluid removal and EEG recording in the cranial subdural/subarachnoid space of primates." Journal of neuroscience methods 203.2 (2012): 275-283.

[179] Sawan, Mohamad, et al. "Wireless recording systems: from noninvasive EEG-NIRS to invasive EEG devices." IEEE Transactions on Biomedical Circuits and Systems 7.2 (2013): 186-195.

[180] Gargiulo, Gaetano, et al. "A mobile EEG system with dry electrodes." 2008 IEEE biomedical circuits and systems conference. IEEE, 2008.

[181] Casson, Alexander J., et al. "Wearable electroencephalography." IEEE engineering in medicine and biology magazine 29.3 (2010): 44-56.

[182] Saadi, Hyem, Merzak Ferroukhi, and Mokhtar Attari. "Development of wireless high immunity EEG recording system." 2011 International Conference on Electronic Devices, Systems and Applications (ICEDSA). IEEE, 2011.

[183] Filipe, Sabine, et al. "A wireless multichannel EEG recording platform." 2011 Annual International Conference of the IEEE Engineering in Medicine and Biology Society. IEEE, 2011.

[184] Engin, Mehmet, et al. "A prototype portable system for EEG measurements." Measurement 40.9-10 (2007): 936-942.

[185] Duun-Henriksen, Jonas, et al. "EEG signal quality of a subcutaneous recording system compared to standard surface electrodes." Journal of Sensors 2015 (2015).

[186] Chang, Pishan, Kevan S. Hashemi, and Matthew C. Walker. "A novel telemetry system for recording EEG in small animals." Journal of neuroscience methods 201.1 (2011): 106-115.

[187] Assawaworrarit, Sid, Xiaofang Yu, and Shanhui Fan. "Robust wireless power transfer using a nonlinear parity–time-symmetric circuit." Nature 546.7658 (2017): 387-390.

[188] Fu, Minfan, et al. "Analysis and tracking of optimal load in wireless power transfer systems." IEEE Transactions on Power Electronics 30.7 (2014): 3952-3963.

[189] Wang, Guoxing, et al. "A dual band wireless power and data telemetry for retinal prosthesis." 2006 International Conference of the IEEE Engineering in Medicine and Biology Society. IEEE, 2006.

[190] Kilinc, Enver G., et al. "A system for wireless power transfer and data communication of long-term bio-monitoring." IEEE Sensors Journal 15.11 (2015): 6559-6569.

[191] Poon, Ada SY, Stephen O'Driscoll, and Teresa H. Meng. "Optimal frequency for wireless power transmission into dispersive tissue." IEEE Transactions on Antennas and Propagation 58.5 (2010): 1739-1750.

[192] Shadid, Reem, and Sima Noghanian. "A literature survey on wireless power transfer for biomedical devices." International Journal of Antennas and Propagation 2018 (2018).

[193] Sahai, Aakash, and David Graham. "Optical wireless power transmission at long wavelengths." 2011 International Conference on Space Optical Systems and Applications (ICSOS). IEEE, 2011.

[194] Duong, Thuc Phi, and Jong-Wook Lee. "Experimental results of high-efficiency resonant coupling wireless power transfer using a variable coupling method." IEEE Microwave and Wireless Components Letters 21.8 (2011): 442-444.

[195] Poon, Ada SY, Stephen O'Driscoll, and Teresa H. Meng. "Optimal operating frequency in wireless power transmission for implantable devices." 2007 29th Annual International Conference of the IEEE Engineering in Medicine and Biology Society. IEEE, 2007.

[196] Dinis, Hugo, Ivo Colmiais, and Paulo M. Mendes. "Design and validation of a six-antenna WPT system with tracking capabilites for biomedical devices." 2019 17th IEEE International New Circuits and Systems Conference (NEWCAS). IEEE, 2019..

[197] Jiang, Hao, et al. "A low-frequency versatile wireless power transfer technology for biomedical implants." IEEE transactions on biomedical circuits and systems 7.4 (2012): 526-535.

[198] Shaw, Tarakeswar, and Debasis Mitra. "Wireless power transfer system design for biomedical implants at 2.45 GHz." 2019 IEEE Asia-Pacific Microwave Conference (APMC). IEEE, 2019..

[199] Pokharel, Ramesh K., et al. "Wireless power transfer system rigid to tissue characteristics using metamaterial inspired geometry for biomedical implant applications." Scientific reports 11.1 (2021): 1-10.

[200] Dai, Zhongyu, et al. "Selective omnidirectional magnetic resonant coupling wireless power transfer with multiple-receiver system." IEEE Access 6 (2018): 19287-19294.

[201] Cannon, Benjamin L., et al. "Magnetic resonant coupling as a potential means for wireless power transfer to multiple small receivers." IEEE transactions on power electronics 24.7 (2009): 1819-1825.

[202] Matias, Ricardo, Bernardo Cunha, and Rui Martins. "Modeling inductive coupling for wireless power transfer to integrated circuits." 2013 IEEE Wireless Power Transfer (WPT). IEEE, 2013.

[203] Kim, Jiseong, et al. "Coil design and shielding methods for a magnetic resonant wireless power transfer system." Proceedings of the IEEE 101.6 (2013): 1332-1342.

[204] Zhang, Jian, et al. "Comparative analysis of two-coil and three-coil structures for wireless power transfer." IEEE Transactions on Power Electronics 32.1 (2016): 341-352.

[205] Wu, Rongxiang, et al. "Silicon-embedded receiving coil for high-efficiency wireless power transfer to implantable biomedical ICs." IEEE Electron Device Letters 34.1 (2012): 9-11.

[206] Jeong, Seungtaek, et al. "Smartwatch strap wireless power transfer system with flexible PCB coil and shielding material." IEEE Transactions on Industrial Electronics 66.5 (2018): 4054-4064.

[207] RamRakhyani, Anil Kumar, and Gianluca Lazzi. "Multi-coil approach to reduce electromagnetic energy absorption for wirelessly powered implants." Healthcare Technology Letters 1.1 (2014): 21-25.

[208] Mirbozorgi, S. Abdollah, et al. "A smart multicoil inductively coupled array for wireless power transmission." IEEE Transactions on Industrial Electronics 61.11 (2014): 6061-6070.

[209] Ahn, Dukju, and Maysam Ghovanloo. "Optimal design of wireless power transmission links for millimeter-sized biomedical implants." IEEE transactions on biomedical circuits and systems 10.1 (2015): 125-137.

[210] Erfani, Reza, et al. "Modeling and experimental validation of a capacitive link for wireless power transfer to biomedical implants." IEEE Transactions on Circuits and Systems II: Express Briefs 65.7 (2017): 923-927.

[211] Low, Zhen Ning, et al. "Design and test of a high-power high-efficiency loosely coupled planar wireless power transfer system." IEEE transactions on industrial electronics 56.5 (2008): 1801-1812.

[212] Shoki, Hiroki. "Issues and initiatives for practical deployment of wireless power transfer technologies in Japan." Proceedings of the IEEE 101.6 (2013): 1312-1320.

[213] Fukuda, Shinichi, et al. "A novel metal detector using the quality factor of the secondary coil for wireless power transfer systems." 2012 IEEE MTT-S International Microwave Workshop Series on Innovative Wireless Power Transmission: Technologies, Systems, and Applications. IEEE, 2012.

[214] Chen, Chen, et al. "Novel flexible material-based unobtrusive and wearable body sensor networks for vital sign monitoring." IEEE Sensors Journal 19.19 (2018): 8502-8513.

[215] Yu, Xi, and Wen Qi. "A user study of wearable EEG headset products for emotion analysis." Proceedings of the 2018 International Conference on Algorithms, Computing and Artificial Intelligence. 2018.

[216] Abhishek, B., et al. "Low Power Portable EEG for Continuous Monitoring with Active Electrodes." 2013 Texas Instruments India Educators' Conference. IEEE, 2013.

[217] Dumitriu, Lucia, et al. "On wireless power transfer." 2012 International Conference on Applied and Theoretical Electricity (ICATE). IEEE, 2012.

[218] Halim, Miah A., et al. "Miniature electrodynamic wireless power transmission receiver using a micromachined silicon suspension." Journal of Microelectromechanical Systems 30.1 (2021): 144-155.

[219] Song, Mingzhao, et al. "Wireless power transfer based on novel physical concepts." Nature Electronics 4.10 (2021): 707-716.

[220] Smith, S., et al. "Development of a miniaturised drug delivery system with wireless power transfer and communication." IET nanobiotechnology 1.5 (2007): 80-86.

[221] Khan, Sadeque Reza, Sumanth Kumar Pavuluri, and Marc PY Desmulliez. "Accurate modeling of coil inductance for near-field wireless power transfer." IEEE Transactions on Microwave Theory and Techniques 66.9 (2018): 4158-4169.

[222] Hwang, Hyeonseok, et al. "An analysis of magnetic resonance coupling effects on wireless power transfer by coil inductance and placement." IEEE Transactions on Consumer Electronics 60.2 (2014): 203-209.

[223] Pacurar, Claudia, et al. "The Construction of a Wireless Power Supply System using Planar Spiral Inductors." 2019 8th International Conference on Modern Power Systems (MPS). IEEE, 2019.

[224] Islam, Ashraf B., Syed K. Islam, and Fahmida S. Tulip. "Design and optimization of printed circuit board inductors for wireless power transfer system." (2013).

[225] Chen, Chih-Jung, et al. "A study of loosely coupled coils for wireless power transfer." IEEE Transactions on Circuits and Systems II: Express Briefs 57.7 (2010): 536-540.

[226] Jenei, Snezana, Bart KJC Nauwelaers, and Stefaan Decoutere. "Physics-based closed-form inductance expression for compact modeling of integrated spiral inductors." IEEE Journal of Solid-State Circuits 37.1 (2002): 77-80.

[227] Pacurar, Claudia, et al. "STUDIES OF INDUCTANCE VARIATION FOR SQUARE SPIRAL INDUCTORS USING CIBSOC SOFTWARE." Environmental Engineering & Management Journal (EEMJ) 12.6 (2013).

[228] Pacurar, Claudia, et al. "Inductance calculation and layout optimization for planar spiral inductors." 2012 13th International Conference on Optimization of Electrical and Electronic Equipment (OPTIM). IEEE, 2012.

[229] Andreica, Sergiu, et al. "Design of multilayer spiral coils with different geometries to determine the inductance." 2020 International Conference and Exposition on Electrical And Power Engineering (EPE). IEEE, 2020.

[230] Valdés-Rayón, José, Reydezel Torres-Torres, and Roberto S. Murphy-Arteaga. "Scalable Model for the Intrinsic Inductance of Octagonal Inductors in RFCMOS."

[231] Liu, Shuangke, et al. "A novel design methodology for high-efficiency current-mode and voltage-mode class-E power amplifiers in wireless power transfer systems." IEEE Transactions on Power Electronics 32.6 (2016): 4514-4523.

[232] Chen, W., et al. "A 25.6 W 13.56 MHz wireless power transfer system with a 94% efficiency GaN class-E power amplifier." 2012 IEEE/MTT-S International Microwave Symposium Digest. IEEE, 2012.

[233] Chokkalingam, Bharatiraja, Sanjeevikumar Padmanaban, and Zbigniew M. Leonowicz. "Class E power amplifier design and optimization for the capacitive coupled wireless power transfer system in biomedical implants." Energies 10.9 (2017): 1409.

[234] Mutashar, Saad, et al. "Analysis and optimization of spiral circular inductive coupling link for bio-implanted applications on air and within human tissue." Sensors 14.7 (2014): 11522-11541.

[235] RamRakhyani, Anil Kumar, Shahriar Mirabbasi, and Mu Chiao. "Design and optimization of resonance-based efficient wireless power delivery systems for biomedical implants." IEEE Transactions on Biomedical Circuits and Systems 5.1 (2010): 48-63.

[236] Harrison, Reid R. "Designing efficient inductive power links for implantable devices." 2007 IEEE International Symposium on Circuits and Systems. IEEE, 2007.

[237] Mirbozorgi, S. Abdollah, et al. "Multi-resonator arrays for smart wireless power distribution: comparison with experimental assessment." IET Power Electronics 13.18 (2020): 4183-4193.

[238] Gundogdu, Askin Erdem, and Erkan Afacan. "The effect of frequency, multi resonator and relay resonator conditions on wireless power transmission." Wireless Telecommunications Symposium 2012. IEEE, 2012.

[239] Saha, Reepa, Bhadhan Roy Joy, and S. A. Mirbozorgi. "Wireless Power Transmission with Uniform Power Delivery in the 3D Space of the Human Body using Resonators in Parallel." 2021 43rd Annual International Conference of the IEEE Engineering in Medicine & Biology Society (EMBC). IEEE, 2021.

[240] Lee, Byunghun, Mehdi Kiani, and Maysam Ghovanloo. "A triple-loop inductive power transmission system for biomedical applications." IEEE transactions on biomedical circuits and systems 10.1 (2015): 138-148.

[241] Park, Byung-Chul, and Jeong-Hae Lee. "Adaptive impedance matching of wireless power transmission using multi-loop feed with single operating frequency." IEEE Transactions on Antennas and Propagation 62.5 (2014): 2851-2856.

[242] Kim, Jungsik, and Jinho Jeong. "Range-adaptive wireless power transfer using multiloop and tunable matching techniques." IEEE Transactions on Industrial Electronics 62.10 (2015): 6233-6241.

[243] Kim, JinWook, et al. "Efficiency analysis of magnetic resonance wireless power transfer with intermediate resonant coil." IEEE Antennas and Wireless Propagation Letters 10 (2011): 389-392.

[244] Agbinya, Johnson I. Wireless power transfer. Vol. 45. River Publishers, 2015.

[245] Jia, Zhiwei, et al. "The optimization of wireless power transmission: design and realization." The International Journal of Medical Robotics and Computer Assisted Surgery 8.3 (2012): 337-347.

[246] Kim, Yong-Hae, et al. "Optimization of wireless power transmission through resonant coupling." SPEEDAM 2010. IEEE, 2010.

[247] Arakawa, Tomohiro, et al. "Optimizing wireless power transfer from multiple transmit coils." IEEE access 6 (2018): 23828-23838.

[248] Duan, Zhu, Yong-Xin Guo, and Dim-Lee Kwong. "Rectangular coils optimization for wireless power transmission." Radio Science 47.03 (2012): 1-10.

[249] Wang, Meng, et al. "Demagnetization weakening and magnetic field concentration with ferrite core characterization for efficient wireless power transfer." IEEE Transactions on Industrial Electronics 66.3 (2018): 1842-1851.

[250] Santalunai, Samran, Chanchai Thongsopa, and Thanaset Thosdeekoraphat. "An increasing the power transmission efficiency of flat spiral coils by using ferrite materials for wireless power transfer applications." 2014 11th International Conference on Electrical Engineering/Electronics, Computer, Telecommunications and Information Technology (ECTI-CON). IEEE, 2014.

[251] Strauch, Ludvik, Mojca Pavlin, and Vladimir Boštjan Bregar. "Optimization, design, and modeling of ferrite core geometry for inductive wireless power transfer." International Journal of Applied Electromagnetics and Mechanics 49.1 (2015): 145-155.

[252] Hwang, Karam, et al. "Ferrite position identification system operating with wireless power transfer for intelligent train position detection." IEEE Transactions on Intelligent Transportation Systems 20.1 (2018): 374-382.

[253] Rodríguez, Erik Saturnino Gámez, et al. "Compact low-frequency metamaterial design for wireless power transfer efficiency enhancement." IEEE Transactions on Microwave Theory and Techniques 64.5 (2016): 1644-1654.

[254] Zhang, Zhen, and Bowen Zhang. "Angular-misalignment insensitive omnidirectional wireless power transfer." IEEE Transactions on Industrial Electronics 67.4 (2019): 2755-2764.

[255] Cazan, Dorotheea, et al. "The effect on snoring of using a pillow to change the head position." Sleep and Breathing 21.3 (2017): 615-621.

[256] Yuan, Qiaowei, Qiang Chen, and Kunio Sawaya. "Effect of nearby human body on WPT system." Proc. of the 5th European Conference on Antennas and Propagation (EUCAP). IEEE, 2011.

[257] Mou, Xiaolin, and Hongjian Sun. "Wireless power transfer: Survey and roadmap." 2015 IEEE 81st Vehicular Technology Conference (VTC Spring). IEEE, 2015.

[258] Waters, Benjamin H., et al. "Optimal coil size ratios for wireless power transfer applications." 2014 IEEE international symposium on circuits and systems (ISCAS). IEEE, 2014.

[259] Rattanarungngam, Darupon, Kittisak Phaebua, and Titipong Lertwiriyaprapa. "Power control unit for E-class power oscillator of 6.78 MHz wireless power transfer." 2017 International Symposium on Antennas and Propagation (ISAP). IEEE, 2017.

[260] Roshan, Yaser M., and Edward J. Park. "Design approach for a wireless power transfer system for wristband wearable devices." IET Power Electronics 10.8 (2017): 931-937

[261] Morikawa, Koji, et al. "Compact wireless EEG system with active electrodes for daily healthcare monitoring." 2013 IEEE International Conference on Consumer Electronics (ICCE). IEEE, 2013.

[262] Penders, Julien, et al. "Wireless EEG systems: Increasing functionality, decreasing power." 2010 Annual International Conference of the IEEE Engineering in Medicine and Biology. IEEE, 2010.

[263] Chen, Wei-Chen, et al. "An EEG analog front-end design with wireless communication module for a portable EEG monitoring system." 2015 IEEE 5th International Conference on Consumer Electronics-Berlin (ICCE-Berlin). IEEE, 2015.

[264] Chen, Xun, and Z. Jane Wang. "Design and implementation of a wearable, wireless EEG recording system." 2011 5th International Conference on Bioinformatics and Biomedical Engineering. IEEE, 2011.

[265] Chebli, Robert, and Mohamad Sawan. "Low noise and high CMRR front-end amplifier dedicated to portable EEG acquisition system." 2013 35th Annual International Conference of the IEEE Engineering in Medicine and Biology Society (EMBC). IEEE, 2013.

[266] Subha, D. Puthankattil, et al. "EEG signal analysis: a survey." Journal of medical systems 34.2 (2010): 195-212.

[267] Osselton, J. W. "Acquisition of EEG data by bipolar unipolar and average reference methods: a theoretical comparison." Electroencephalography and clinical neurophysiology 19.5 (1965): 527-528.

[268] Taheri, Babak A., Robert T. Knight, and Rosemary L. Smith. "A dry electrode for EEG recording." Electroencephalography and clinical neurophysiology 90.5 (1994): 376-383..

[269] Zheng, Wei-Long, and Bao-Liang Lu. "Investigating critical frequency bands and channels for EEG-based emotion recognition with deep neural networks." IEEE Transactions on Autonomous Mental Development 7.3 (2015): 162-175.

[270] Sazgar, Mona, and Michael G. Young. "EEG artifacts." Absolute epilepsy and EEG rotation review. Springer, Cham, 2019. 149-162.

[271] Kannan, Ramani, et al. "Smart wearable EEG sensor." Procedia Computer Science 105 (2017): 138-143.

[272] Lucey, Brendan P., et al. "Comparison of a single-channel EEG sleep study to polysomnography." Journal of sleep research 25.6 (2016): 625-635.

[273] Vaughan, Theresa M., Jonathan R. Wolpaw, and Emanuel Donchin. "EEG-based communication: prospects and problems." IEEE transactions on rehabilitation engineering 4.4 (1996): 425-430.

[274] Lee, Chung-Jae, and Jong-In Song. "A chopper stabilized current-feedback instrumentation amplifier for EEG acquisition applications." IEEE Access 7 (2019): 11565-11569.

[275] Xu, Jiawei, et al. "Active electrodes for wearable EEG acquisition: Review and electronics design methodology." IEEE reviews in biomedical engineering 10 (2017): 187-198.

[276] Verma, Naveen, et al. "A micro-power EEG acquisition SoC with integrated feature extraction processor for a chronic seizure detection system." IEEE journal of solid-state circuits 45.4 (2010): 804-816.

[277] Martins, Rui, Siegfried Selberherr, and Francisco A. Vaz. "A CMOS IC for portable EEG acquisition systems." IEEE Transactions on Instrumentation and measurement 47.5 (1998): 1191-1196.

[278] Guermandi, Marco, Eleonora Franchi Scarselli, and Roberto Guerrieri. "A driving right leg circuit (DgRL) for improved common mode rejection in bio-potential acquisition systems." IEEE transactions on biomedical circuits and systems 10.2 (2015): 507-517.

[279] Doneva, Mariya, et al. "Compressed sensing reconstruction for magnetic resonance parameter mapping." Magnetic Resonance in Medicine 64.4 (2010): 1114-1120.

[280] Deo, Ankita, et al. "Design of a Third Order Butterworth G m-C Filter for EEG Signal Detection Application." 2018 25th International Conference" Mixed Design of Integrated Circuits and System"(MIXDES). IEEE, 2018.

[281] Young, G. Bryan, et al. "A comparison of subdermal wire electrodes with collodion-applied disk electrodes in long-term EEG recordings in ICU." Clinical neurophysiology 117.6 (2006): 1376-1379..

[282] Usakli, Ali Bulent. "Improvement of EEG signal acquisition: An electrical aspect for state of the art of front end." Computational intelligence and neuroscience 2010 (2010).

[283] Xu, Jiawei, et al. "A 160 μm 8-Channel Active Electrode System for EEG Monitoring." IEEE Transactions on Biomedical circuits and systems 5.6 (2011): 555-567.

[284] Broniec, Anna. "Analysis of EEG signal by flicker-noise spectroscopy: identification of right-/left-hand movement imagination." Medical & Biological Engineering & Computing 54.12 (2016): 1935-1947.

[285] Van Den Dool, Bernard J., and J. K. Huijsing. "Indirect current feedback instrumentation amplifier with a common-mode input range that includes the negative roll." IEEE Journal of Solid-State Circuits 28.7 (1993): 743-749.

[286] Costa, Guillermo, Alfredo Arnaud, and Matías Miguez. "A precision autozero amplifier for EEG signals." Proceedings of the 23rd symposium on Integrated circuits and system design. 2010.

[287] Li, Bohao, Tianshuo Cheng, and Zexuan Guo. "A review of EEG acquisition, processing and application." Journal of Physics: Conference Series. Vol. 1907. No. 1. IOP Publishing, 2021.

[288] Chebli, Robert, Mohamed Ali, and Mohamad Sawan. "High-CMRR low-noise fully integrated front-end for eeg acquisition systems." Electronics 8.10 (2019): 1157.

[289] Ferree, Thomas C., et al. "Scalp electrode impedance, infection risk, and EEG data quality." Clinical neurophysiology 112.3 (2001): 536-544.

[290] Guermandi, Marco, et al. "Active electrode IC combining EEG, electrical impedance tomography, continuous contact impedance measurement and power supply on a single wire." 2011 Proceedings of the ESSCIRC (ESSCIRC). IEEE, 2011.

[291] Tyagi, Aruna, Sunil Semwal, and Gautam Shah. "A review of EEG sensors used for data acquisition." Journal of Computer Applications (IJCA) (2012): 13-17.

[292] Delorme, A., et al., EEG / ERP data available for free public download. [Online]. Available: https://sccn.ucsd.edu/~arno/fam2data/publicly_available_EEG_data.html (visited on 05/11/2018)

[293] Hoseini, Zaniar, et al. "Current feedback instrumentation amplifier with built-in differential electrode offset cancellation loop for ECG/EEG sensing frontend." IEEE Transactions on Instrumentation and Measurement 70 (2020): 1-11.

[294] Tohidi, Mohammad, Jens Kargaard Madsen, and Farshad Moradi. "Low-power high-input-impedance EEG signal acquisition SoC with fully integrated IA and signal-specific ADC for wearable applications." IEEE Transactions on Biomedical Circuits and Systems 13.6 (2019): 1437-1450.

[295] Chen, Yi-Chung, Zong-Han Hsieh, and Wai-Chi Fang. "A wireless readout front-end device for portable EEG acquisition system." 2013 IEEE International Symposium on Consumer Electronics (ISCE). IEEE, 2013.

[296] Liu, Ming, et al. "Low-Power IC design for a wireless BCI system." 2008 IEEE International Symposium on Circuits and Systems. IEEE, 2008.

[297] Kaur, Amandeep, and Deepak Mishra. "A reconfigurable cyclic ADC for biomedical applications." 2019 IEEE Biomedical Circuits and Systems Conference (BioCAS). IEEE, 2019.

[298] Chen, Chia-Hung, Yi Zhang, and Gabor C. Temes. "History, present state-of-art and future of incremental ADCs." ESSCIRC Conference 2016: 42nd European Solid-State Circuits Conference. IEEE, 2016.

[299] Ozols, K., M. Greitans, and R. Shavelis. "EEG data acquisition system based on asynchronous sigma-delta modulator." 2012 13th Biennial Baltic Electronics Conference. IEEE, 2012.

[300] https://ortus.rtu.lv/science/lv/publications/25512/attachments/2903

[301] Kościelnik, Dariusz, Dominik Rzepka, and Jakub Szyduczyński. "Sample-and-hold asynchronous sigma-delta time encoding machine." IEEE Transactions on Circuits and Systems II: Express Briefs 63.4 (2015): 366-370.

[302] Mollazadeh, Mohsen, et al. "Micropower CMOS integrated low-noise amplification, filtering, and digitization of multimodal neuropotentials." IEEE transactions on biomedical circuits and systems 3.1 (2009): 1-10.

[303] Harrison, Reid R., and Cameron Charles. "A low-power low-noise CMOS amplifier for neural recording applications." IEEE Journal of solid-state circuits 38.6 (2003): 958-965.

[304] Verma, Naveen, and Anantha P. Chandrakasan. "An ultra low energy 12-bit rate-resolution scalable SAR ADC for wireless sensor nodes." IEEE Journal of Solid-State Circuits 42.6 (2007): 1196-1205.

[305] Hasan, Md Kamrul, et al. "Design and simulation of cost-effective wireless EEG acquisition system for patient monitoring." 2014 International Conf. on Informatics, Electronics & Vision (ICIEV). IEEE, 2014.

[306] Li, Ping, et al. "A Smart Safety Helmet using IMU and EEG sensors for worker fatigue detection." 2014 IEEE International Symposium on Robotic and Sensors Environments (ROSE) Proceedings. IEEE, 2014.

[307] Greenwald, Elliot, et al. "A VLSI neural monitoring system with ultra-wideband telemetry for awake behaving subjects." IEEE transactions on biomedical circuits and systems 5.2 (2011): 112-119.

[308] Delorme, Arnaud, Terrence Sejnowski, and Scott Makeig. "Enhanced detection of artifacts in EEG data using higher-order statistics and independent component analysis." Neuroimage 34.4 (2007): 1443-1449.

[309] Nazzal, Tasnim B., Soliman A. Mahmoud, and Mohamed O. Shaker. "A 200-nw 7.6-enob 10-ks/s sar adc in 90-nm cmos for portable biomedical applications." Microelectronics Journal 56 (2016): 81-96.

[310] Senevirathna, Bathiya, et al. "Low cost mobile EEG for characterization of cortical auditory responses." 2016 IEEE International Symposium on Circuits and Systems (ISCAS). IEEE, 2016.

[311] Vo, Thong Tri, Nam Phuong Nguyen, and Toi Vo Van. " Wireless 8-channel EEG recording device." International Conference on the Development of Biomedical Engineering in Vietnam. Springer, Singapore, 2017.

[312] Campillo, Daniel, et al. "A real-time ECG preprocessing system based on ADS1298." Computing in Cardiology 2013. IEEE, 2013.

[313] Wild M., Pegan R. Wearable Bluetooth Brain-Computer Interface for Detection and Analysis of Ear-EEG Signals. [(accessed on 26 June 2018)];2015 Available online: https://www.semanticscholar.org/paper/Wearable-Bluetooth-Brain-Computer-Interface-for-and-Wild-Pegan/bae82d84b4384bd86cf942139ac9a45326f3083d.

[314] https://docs.openbci.com/AddOns/Headwear/ElectrodeCap/

[315] Nathan, Viswam, et al. "A 16-channel bluetooth enabled wearable eeg platform with dry-contact electrodes for brain computer interface." Proceedings of the 4th Conference on Wireless Health. 2013.

[316] Xu, Jiahui, and Baichang Zhong. "Review on portable EEG technology in educational research." Computers in Human Behavior 81 (2018): 340-349.

[317] Favretto, Mateus Andre, et al. "High density surface EMG system based on ADS1298-front end." IEEE Latin America Transactions 16.6 (2018): 1616-1622.

[318] Seco, Giordano BS, et al. "EEG alpha rhythm detection on a portable device." Biomedical Signal Processing and Control 52 (2019): 97-102.

[319] Texas Instruments ADS129x Low-Power, 8-Channel, 24-Bit Analog Front-End for Biopotential Measurements. [(accessed on 11 May 2018)]; Available:: http://www.ti.com/lit/ds/symlink/ads1298.pdf.

[320] Mastinu, Enzo, Max Ortiz-Catalan, and Bo Håkansson. "Analog front-ends comparison in the way of a portable, low-power and low-cost EMG controller based on pattern recognition." 2015 37th annual international conference of the IEEE engineering in medicine and biology society (EMBC). IEEE, 2015.

[321] Acharya, Deepshikha, Asha Rani, and Shivangi Agarwal. "EEG data acquisition circuit system based on ADS1299EEG FE." 2015 4th International Conference on Reliability, Infocom Technologies and Optimization (ICRITO)(Trends and Future Directions). IEEE, 2015.

[322] Spicer, Ryan, et al. "REINVENT: A low-cost, virtual reality brain-computer interface for severe stroke upper limb motor recovery." 2017 IEEE Virtual Reality (VR). IEEE, 2017.

VITA

MAHMOUD SHARAFI MASOULEH

Aug 2017–July 2022 Florida International University, Miami, Florida US
Doctor of Philosophy in Electrical and Computer Engineering

Sep 2008 – Jan 2012 Iran University of Science and Technology, Tehran, Iran
Master of Science in Electrical and Communication-Fields and System-Engineeri

Sep2003 – June 2008 Bachelor of Science in Electrical Engineering, Iran

PUBLICATIONS AND PRESENTATIONS

1. M. Sharafi Masouleh, A.Kargar Behbahani, and M. Adjouadi, " Design, Analysis, and Optimization of the Array of Axial Rectangular Slots on a Cylindrical Waveguide," IEEE Access, vol. 9, pp. 98218 - 98230, 2021.
2. Homayoon Oraizi, Amin Kargar Behbahani, Mahmoud T. Noghani, Mahmoud Sharafi Masouleh "Optimum design of traveling rectangular waveguide edge slot array with non-uniform spacing " Published in IET Microwaves, Antennas & Propagation Vol.7 (7), PP575-581, 2013.
3. Mahmoud Sharafi Masouleh, Amin Kargar Behbahani " Optimum Design of the Array of Circumferential Slots on a Cylindrical Waveguide " AEU, International Journal of Electronics and Communications, Urban & Fischer, 70 (2016), pp. 578-583.
4. Abdullah Ahmadi, Mahmoud Sharafi Masouleh, Mohammadreza Janghorbani, Navid Yadollahi Ghasemi Manjili, Adel M Sharaf, Ali Esmaeel Nezhad "Short-term multi-objective hydrothermal scheduling" Published in Electric Power Systems Research Volume 121 Pages 357-367 Publisher Elsevier 2015.
5. Mahmoud Sharafi Masouleh Abdullah Ahmadi " Mixed-integer programming of the stochastic hydro self-scheduling problem in joint energy and reserves markets" Journal Electric Power Components and Systems, Volume 44 Issue7 Pages 752-762 Publisher Taylor & Francis, (Manuscript ID UEMP-2014-0304.R2).
6. Ali Azarbar, Mahmoud Sharafi Masouleh, Amin Kargar Behbahani "A New Terahertz Microstrip Rectangular Patch Array Antenna" International Journal of Electromagnetics and Applications Vol.4 (1), pp.25-29-2014.
7. M. Sharafi Masouleh, A.Kargar Behbahani, and M. Adjouadi, " Pattern Synthesis of a Resonant Slot on a Broad Wall of the Rectangular Waveguide Using Amplitude and Phase Control," IEEE Antennas and Wireless Propagation Letters AWPL (under Review).
8. M. Sharafi Masouleh, A.Kargar Behbahani, and M. Adjouadi, " Mutual Admittance Calculation and Validation of Optimized Design Equations of a Slot Array on a Cylindrical Waveguide Using a Genetic Algorithm and the Conjugate Gradient Method," International Journal of Communication Systems - IJCS Wiley (under Review).

9. Mahmoud Sharafi, Maryam Sajedi, Malek Adjouadi "Highly Efficient Power Transmission-Conversion Chain For a Wireless and Battery-Free EEG Cap" 2022 IEEE International Symposium on Antennas and Propagation and USNC-URSI Radio Science Meeting, • Denver, Colorado. (Accepted)

10. Mahmoud Sharafi, Maryam Sajedi, Malek Adjouadi "Intelligent Remote Powering System With PTE Auto- Balancing For a Wireless and Battery-Free EEG Cap" 2022 IEEE International Symposium on Antennas and Propagation and USNC-URSI Radio Science Meeting, • Denver, Colorado. (Accepted)

11. A.Azarbar, M.Sharafi Masouleh, A.kargar Behbahani, H.Oraizi, "Comparison of Different Designs of Cylindrical Printed Quadrifilar Helix Antennas," International Conference on Computer and Communication Engineering (ICCCE 2012), 3-5 July 2012, Kuala Lumpur, Malaysia.

12. Mahmoud Sharafi Masouleh, Abdul-Sattar Kaddour, Stavros Georgakopoulos" Recent Advances in Wireless Systems for Simultaneous Power and Data Transfer" 2019 International Applied Computational Electromagnetics Society Symposium (ACES).April 14-18, 201Miami,FL,USA.

13. Mahmoud Sharafi Masouleh, Daerhan Liu, Constantinos L Zekios, Stavros V "Wireless Power Transfer and High Data Rate Communication Using Load-Shift Keying Modulation" 2019 International Workshop on Antenna Technology (iWAT), March 3rd-6th, 2019, Miami, FL USA.

14. Mahmoud Sharafi, Constantinos L. Zekios, Stavros V. Georgakopoulos "Simultaneous High Data Rate Communication and Highly Efficient Wireless Power Transfer Through a Coplanar Link" 2019 IEEE International Symposium on Antennas and Propagation and USNC-URSI Radio Science Meeting7-12 July 2019 • Atlanta, Georgia, U.S.A - Pages 1797-1798.

15. Mahmoud Sharafi, Constantinos L. Zekios, Stavros V. Georgakopoulos "Simultaneous Wireless Power & Data Transmission for Wearable Applications" 2019 IEEE International Symposium on Antennas and Propagation and USNC-URSI Radio Science Meeting,7-12 July 2019 • Atlanta, Georgia, U.S.A. Pages 1801-1802